universe

MDPI

Article

Neutrino Oscillations in Neutrino-Dominated Accretion Around Rotating Black Holes

Juan David Uribe [1,2,†], Eduar Antonio Becerra-Vergara [1,2,3,†] and Jorge Armando Rueda [2,4,5,6,*,†]

1 Dipartimento di Fisica, Sapienza Università di Roma, P.le Aldo Moro 5, 00185 Rome, Italy; juandavid.uribe@uniroma1.it (J.D.U.); eduar.becerra@icranet.org (E.A.B.-V.)
2 ICRANet, Piazza della Repubblica 10, 65122 Pescara, Italy
3 Grupo de Investigación en Relatividad y Gravitación, Escuela de Física, Universidad Industrial de Santander, A. A. 678, Bucaramanga 680002, Colombia
4 ICRANet-Ferrara, Dipartimento di Fisica e Scienze della Terra, Università degli Studi di Ferrara, Via Saragat 1, 44122 Ferrara, Italy
5 Dipartimento di Fisica e Scienze della Terra, Università degli Studi di Ferrara, Via Saragat 1, 44122 Ferrara, Italy
6 INAF, Istituto di Astrofisica e Planetologia Spaziali, Via Fosso del Cavaliere 100, 00133 Rome, Italy
* Correspondence: jorge.rueda@icra.it
† These authors contributed equally to this work.

Abstract: In the binary-driven hypernova model of long gamma-ray bursts, a carbon–oxygen star explodes as a supernova in the presence of a neutron star binary companion in close orbit. Hypercritical (i.e., highly super-Eddington) accretion of the ejecta matter onto the neutron star sets in, making it reach the critical mass with consequent formation of a Kerr black hole. We have recently shown that, during the accretion process onto the neutron star, fast neutrino flavor oscillations occur. Numerical simulations of the above system show that a part of the ejecta stays bound to the newborn Kerr black hole, leading to a new process of hypercritical accretion. We address herein, also for this phase of the binary-driven hypernova, the occurrence of neutrino flavor oscillations given the extreme conditions of high density (up to 10^{12} g cm^{-3}) and temperatures (up to tens of MeV) inside this disk. We estimate the behavior of the electronic and non-electronic neutrino content within the two-flavor formalism ($\nu_e\nu_x$) under the action of neutrino collective effects by neutrino self-interactions. We find that in the case of inverted mass hierarchy, neutrino oscillations inside the disk have frequencies between $\sim(10^5$–$10^9)$ s^{-1}, leading the disk to achieve flavor equipartition. This implies that the energy deposition rate by neutrino annihilation ($\nu + \bar{\nu} \rightarrow e^- + e^+$) in the vicinity of the Kerr black hole is smaller than previous estimates in the literature not accounting for flavor oscillations inside the disk. The exact value of the reduction factor depends on the ν_e and ν_x optical depths but it can be as high as $\sim$5. The results of this work are a first step toward the analysis of neutrino oscillations in a novel astrophysical context, and as such, deserve further attention.

Keywords: accretion disk; neutrino physics; gamma-ray bursts; black hole physics

Citation: Uribe, J.D.; Becerra-Vergara, E.A.; Rueda, J.A. Neutrino Oscillations in Neutrino-Dominated Accretion Around Rotating Black Holes. *Universe* **2021**, *7*, 7. https://doi.org/10.3390/universe7010007

Received: 28 October 2020
Accepted: 25 December 2020
Published: 4 January 2021

1. Introduction

Neutrino flavor oscillations are now an experimental fact [1], and in recent years, their study based only on Mikheyev–Smirnov–Wolfenstein (MSW) effects [2,3] has been transformed by the insight that refractive effects of neutrinos on themselves due to the neutrino self-interaction potential are essential. Their behavior in a vacuum, in matter or by neutrino self-interactions has been studied in the context of early universe evolution [4–15], solar and atmospheric neutrino anomalies [16–24] and core-collapse supernovae (SN) ([25–51] and references therein). We are interested in astrophysical situations when neutrino self-interactions become more relevant than the matter potential. This implies systems in which a high density of neutrinos is present and in fact most of the literature on neutrino self-interaction dominance is concentrated on supernova neutrinos. It has

been shown how collective effects, such as synchronized and bipolar oscillations, change the flavor content of the emitted neutrinos when compared with the original content deep inside the exploding star.

This article aims to explore the problem of neutrino flavor oscillations in the case of long gamma-ray bursts (GRBs), in particular in the context of the binary-driven hypernova (BdHN) scenario. Long GRBs are the most energetic and powerful cosmological transients so far observed, releasing energies of up to a few 10^{54} erg in just a few seconds. Most of the energy is emitted in the prompt gamma-ray emission and in the X-ray afterglow. We refer the reader to [52] for an excellent review on GRBs and its observational properties.

The GRB progenitor in the BdHN model is a binary system composed of a carbon–oxygen star (CO_{core}) and a companion neutron star (NS) in tight orbit with orbital periods in the order of a few minutes [53–58]. These binaries are expected to occur in the final stages of the evolutionary path of a binary system of two main-sequence stars of masses in the order of 10–15 $M_\odot$, after passing from X-ray binary phase and possibly multiple common-envelope phases (see [57,59] and references therein).

The CO_{core} explodes as SN, creating at its center a newborn NS (νNS), and ejecting the matter from its outermost layers. Part of the ejected matter falls back and accretes onto the νNS, while the rest continues its expansion leading to a hypercritical accretion (i.e., highly super-Eddington) process onto the NS companion. The NS companion reaches the critical mass for gravitational collapse, hence forming a rotating black hole (BH). The class of BdHN in which a BH is formed has been called type I, i.e., BdHN I [60].

One of the most important aspects of the BdHN model of long GRBs is that different GRB observables in different energy bands of the electromagnetic spectrum are explained by different components and physical ingredients of the system. This is summarized in Table 1, taken from [61]. For a review on the BdHN model and all the physical phenomena at work, we refer the reader to [62].

Table 1. Summary of the gamma-ray burst (GRB) observables associated with each BdHN I component and physical phenomenon. Adapted from Table 1 in [61] with the permission of the authors. References in the table: [a] [60], [b] [57,62,63], [c] [64], [d] [65,66], [e] [67], [f] [60,68].

BdHN Component/Phenomena	GRB Observable				
	X-Ray Precursor	**Prompt (MeV)**	**GeV-TeV Emission**	**X-Ray Flares Early Afterglow**	**X-Ray Plateau and Late Afterglow**
SN breakout [a]	⊗				
Hypercrit. acc. onto the NS [b]	⊗				
e^+e^-: transparency in low baryon load region [c]		⊗			
Inner engine: BH + B + matter [d]			⊗		
e^+e^-: transparency in high baryon load region [e]				⊗	
Synchrotron by νNS injected particles on SN ejecta [f]					⊗
νNS pulsar-like emission [f]					⊗

The emission of neutrinos is a crucial ingredient, since they act as the main cooling process that allows the accretion onto the NS to proceed at very high rates of up to 1 $M_\odot$ s^{-1} [57,59,63,69,70]. In [71], we studied the neutrino flavor oscillations in this hypercritical accretion process onto the NS, all the way to BH formation. We showed that the density of neutrinos on top the NS in the accreting "atmosphere" is such that neutrino self-interactions dominate the flavor evolution, leading to collective effects. The latter induce in this system quick flavor conversions with short oscillation lengths as small as

(0.05–1) km. Far from the NS surface, the neutrino density decreases, and so the matter potential and MSW resonances dominate the flavor oscillations. The main result has been that the neutrino flavor content emerging on top of the accretion zone was completely different compared to the one created at the bottom of it. In the BdHN scenario, part of the SN ejecta stays bound to the newborn Kerr BH, forming an accretion disk onto it. In this context, the study of accretion disks and their nuances related to neutrinos is of paramount importance to shed light on this aspect of the GRB central engine. In most cases, the mass that is exchanged in close binaries has enough angular momentum so that it cannot fall radially. As a consequence, the gas will start rotating around the star or BH, forming a disk. At this point, it is worth digressing to mention the case of short GRBs. They are widely thought to be the product of mergers of compact-object binaries, e.g., NS–NS and/or NS–BH binaries (see, e.g., the pioneering works [72–75]). It is then clear that, especially in NS–NS mergers, matter can be kept bound and circularize around the new central remnant. Additionally, in such a case, an accretion disk will form around the more massive NS or the newborn BH (if the new central object overcomes the critical mass), and therefore the results of this work become relevant for such physical systems.

The magneto-hydrodynamics that describe the behavior of accretion disks are too complex to be solved analytically and full numerical analysis is time-consuming and costly. To bypass this difficulty, different models make approximations that allow casting the physics of an accretion disk as a two-dimensional or even one-dimensional problem. These approximations can be can be pigeonholed into four categories: symmetry, temporal evolution, viscosity and dynamics. Almost all analytic models are axially symmetric. This is a sensible assumption for any physical system that rotates. Similarly, most models are time-independent, although this is a more complicated matter. A disk can evolve in time in several ways. For example, the accretion rate $\dot{M}$ depends on the external source of material which need not be constant, and at the same time, the infalling material increases the mass and angular momentum of the central object, constantly changing the gravitational potential. Additionally, strong winds and outflows can continually change the mass of the disk. Nonetheless, $\dot{M}(\boldsymbol{x}, t) = \dot{M} =$ constant is assumed. Viscosity is another problematic approximation. For the gas to spiral down, its angular momentum needs to be reduced by shear stresses. These come from the turbulence driven by differential rotation and the electromagnetic properties of the disk [76–79], but again, to avoid magneto-hydrodynamical calculations, the turbulence is accounted for using a phenomenological viscosity $\alpha =$ constant, such that the kinematical viscosity takes the form $\nu \approx \alpha H c_s$, where c_s is the local isothermal sound speed of the gas and H is the height of the disk measured from the plane of rotation (or half-thickness). This idea was first put forward by [80] and even though there is disagreement about the value and behavior of the viscosity constant, and it has been criticized as inadequate [81–84], several thriving models use this prescription. Finally, the assumptions concerning the dynamics of the disk are related to what terms are dominant in the energy conservation equation and the Navier–Stokes equation that describe the fluid (apart from the ones related to symmetry and time independence). In particular, it amounts to deciding what cooling mechanisms are important, what external potentials should be considered and what are the characteristics of the internal forces in the fluid. The specific tuning of these terms breeds one of the known models: thin disks, slim disks, advection-dominated accretion flows (ADAFs), thick disks, neutrino-dominated accretion flows (NDAFs), convection-dominated accretion flows (CDAFs), luminous hot accretion flows (LHAFs), advection-dominated inflow-outflow solutions (ADIOS) and magnetized tori. The options are numerous and each model is full of subtleties, making accretion flows around a given object an extremely rich area of research. For useful reviews and important articles with a wide range of subjects related to accretion disks, see [85–99] and references therein.

NDAFs are of special interest for GRBs. They are hyperaccreting slim disks, optically thick to radiation that can reach high densities $\rho \approx 10^{10}$–10^{13} g cm^{-3} and high temperatures $T \approx 10^{10}$–10^{11} K around the inner edge. Under these conditions, the main cooling

mechanism is neutrino emission since copious amounts of (mainly electron) neutrinos and antineutrinos are created by electron–positron pair annihilation, URCA and nucleon–nucleon bremsstrahlung processes, and later emitted from the disk surface. These $\nu\bar{\nu}$ pairs might then annihilate above the disk producing an e^-e^+ dominated outflow. NDAFs were proposed as a feasible central engine for GRBs in [100] and have been studied extensively since [101–112]. In [103] and later in [107], it was found that the inner regions of the disk can be optically thick to $\nu_e\bar{\nu}_e$, trapping them inside the disk, hinting that NDAFs may be unable to power GRBs. However, the system involves neutrinos propagating through dense media, and consequently, an analysis of neutrino oscillations, missing in the above literature, must be performed. Figure 1 represents the standard situation of the physical system of interest. The dominance of the self-interaction potential induces collective effects or decoherence. In either case, the neutrino flavor content of the disk changes. Some recent articles are starting to recognize their role in accretion disks and spherical accretion [71,113–117]. In particular, refs. [113,117] calculated the flavor evolution of neutrinos once they are emitted from the disk, but did not take into account the oscillation behavior inside the disk. The energy deposition rate above a disk by neutrino-pair annihilation as a powering mechanism of GRBs in NDAFs can be affected by neutrino oscillation in two ways. The neutrino spectrum emitted at the disk surface depends not only on the disk temperature and density but also on the neutrino flavor transformations inside the disk. Additionally, once the neutrinos are emitted, they undergo flavor transformations before being annihilated.

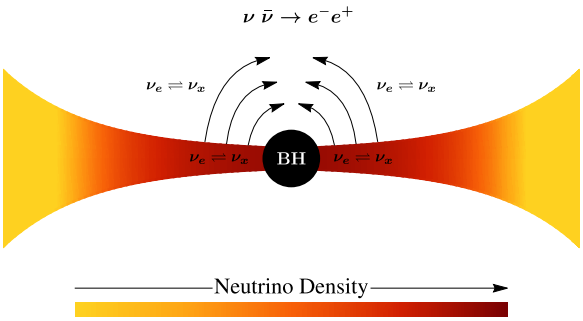

Figure 1. Schematic representation of the physical system. Due to conditions of high temperature and density, neutrinos are produced in copious amounts inside the disk. Since they have very low cross-sectional areas, neutrinos are free to escape but not before experiencing collective effects due to the several oscillation potentials. The energy deposition rate of the process $\nu + \bar{\nu} \rightarrow e^- + e^+$ depends on the local distribution of electronic and non-electronic (anti)neutrinos, which is affected by the flavor oscillation dynamics.

Our main objective is to propose a simple model to study neutrino oscillations inside an accretion disk and analyze its consequences. Applying the formalism of neutrino oscillations to non-symmetrical systems is difficult, so we chose a steady-state, α-disk as a first step in the development of such a model. The generalizations to more sophisticated accretion disks (see, e.g., [118–121]) can be subjects of future research.

This article is organized as follows. We outline the features of NDAFs and discuss in detail the assumptions needed to derive the disk equations in Section 2. Then, in Section 3, we discuss the general characteristics of the equation that drive the evolution of neutrino oscillations. We use the comprehensive exposition of the accretion disk of the previous section to build a simple model that adds neutrino oscillations to NDAFs, while emphasizing how the thin disk approximation can simplify the equations of flavor evolution. In Section 4 we set the parameters of the physical system and give some details on the initial conditions needed to solve the equations of accretion disks and neutrino oscillations. In Section 5 we discuss the main results of our calculations and analyze the phenomenology of neutrino oscillations in accretion disks. Finally, we present in Section 6 the conclusions of this work. Additional technical details are presented in a series of appendices at the end.

2. Hydrodynamics

2.1. Units, Velocities and Averaging

Throughout this article, we use Planck units $c = G = \hbar = k_B = k_e = 1$. To describe the spacetime around a Kerr BH of mass M, we use the metric $g_{\mu\nu}$ in Boyer–Lindquist coordinates, with a space-like signature, and with a dimensionless spin parameter $a = J/M^2$, which can be written as:

$$ds^2 = \left(g_{tt} - \omega^2 g_{\phi\phi}\right) dt^2 + g_{\phi\phi}(d\phi - \omega\, dt)^2 + g_{rr}\, dr^2 + g_{\theta\theta}\, d\theta^2, \tag{1}$$

in coordinates (t, r, θ, ϕ). The covariant components $(\boldsymbol{g})_{\mu\nu}$ of the metric are

$$\begin{aligned} g_{tt} &= -\left(1 - \frac{2\,M\,r}{\Sigma}\right), \quad g_{rr} = \frac{\Sigma}{\Delta}, \quad g_{\theta\theta} = \Sigma, \\ g_{\phi\phi} &= \left(r^2 + M^2 a^2 + \frac{2\,M^3 a^2 r}{\Sigma}\sin^2\theta\right)\sin^2\theta, \quad g_{t\phi} = -\frac{2\,M^2\,a\,r}{\Sigma}\sin^2\theta, \end{aligned} \tag{2}$$

and its determinant is $g = -\Sigma^2 \sin^2\theta$, with the well known functions $\Sigma = r^2 + M^2 a^2 \cos^2\theta$ and $\Delta = r^2 - 2Mr + M^2 a^2$. We denote the coordinate frame by CF. Note that these coordinates can be used by an observer on an asymptotic rest frame. The angular velocity of the locally non-rotating frame (LNRF) is

$$\omega = -\frac{g_{t\phi}}{g_{\phi\phi}} = \frac{2\,a\,M^2}{(r^3 + M^2 a^2 r + 2M^3 a^2)}, \tag{3}$$

and in Equation (2) it can be seen explicitly that if an observer has an angular velocity $\omega = d\phi/dt$, it would not measure any differences between the $\pm\phi$ directions. The LNRF is defined by orthonormality and the coordinate change $\phi_{\rm LNRF} = \tilde{\phi} = \phi - \omega\, t$ [122,123]. We assume that the disk lies on the equatorial plane of the BH ($\theta = \pi/2$). This way we represent the average movement of the fluid by geodesic circular orbits with angular velocity $\Omega = d\phi/dt = u^\phi/u^t$ plus a radial velocity so that the local rest frame (LRF) of the fluid is obtained by performing, first, an azimuthal Lorentz boost with velocity $\beta^{\hat{\phi}}$ to a co-rotating frame (CRF) [124], and then a radial Lorentz boost with velocity $\beta^{\tilde{r}}$. Clearly, the metric on the LNRF, CRF and LRF is $\mathrm{diag}(-1, 1, 1, 1)$. The expression for the angular velocity of circular orbits is obtained by setting $\dot{r} = \ddot{r} = 0$ in the r-component of the geodesic equation

$$\Omega^{\pm} = \pm\frac{\sqrt{M}}{\left(r^{3/2} \pm M^{3/2} a\right)}, \tag{4}$$

where $(+)$ is for prograde orbits and $(-)$ is for retrograde orbits. We will limit our calculations to prograde movement with $0 \leq a \leq 1$, but extension to retrograde orbits is straightforward. Finally, we can get the components of the 4-velocity of the fluid by transforming $\boldsymbol{u}_{\rm LRF} = (1, 0, 0, 0)$ back to the CF

$$u^\mu = \left(\frac{\gamma_{\tilde{r}}\gamma_{\hat{\phi}}}{\sqrt{\omega^2 g_{\phi\phi} - g_{tt}}}, \frac{\gamma_{\tilde{r}}\beta^{\tilde{r}}}{\sqrt{g_{rr}}}, 0, \frac{\gamma_{\tilde{r}}\gamma_{\hat{\phi}}\Omega}{\sqrt{\omega^2 g_{\phi\phi} - g_{tt}}}\right), \tag{5}$$

leaving $\beta^{\tilde{r}}$ to be determined by the conservation laws. In Equation (5) we have replaced $\beta^{\hat{\phi}}$ with Equation (A3). A discussion on the explicit form of the transformations and some miscellaneous results are given in Appendix A. We will also assume that the disk is in a steady-state. This statement requires some analysis. There are two main ways in which it can be false:

First, as matter falls into the BH, its values M and a change [125,126], effectively changing the spacetime around it. For the spacetime to remain the same (i.e., for M and a to stay constant) we require $\Omega^{-1} \ll t_{\rm acc} = \Delta M_0/\dot{M}_{\rm acc}$, where ΔM_0 is the total mass of the disk and $\dot{M}_{\rm acc}$ is the accretion rate. The characteristic accretion time must be bigger than the dynamical time of the disk so that flow changes due to flow dynamics are more important than flow changes due to spacetime changes. Equivalent versions of this condition that appear throughout disk accretion articles are $t_{\rm dym} \ll t_{\rm visc}$ and

$$\beta^r \ll \beta^\phi < 1, \tag{6}$$

where it is understood that the accretion rate obeys $\dot{M}_{\rm acc} \approx \Delta M_0/t_{\rm acc}$. To put these numbers into perspective, consider a solar mass BH ($M = 1M_\odot$) and a disk with mass between $\Delta M_0 = (1-10)M_\odot$. For accretion rates up to $\dot{M}_{\rm acc} = 1M_\odot/$s the characteristic accretion time is $t_{\rm acc} \lesssim (1-10)$ s, while $\Omega^{-1} \sim (10^{-5} - 10^{-1})$ s between $r = r_{\rm ISCO}$ and $r = 2000M_\odot$. Consequently, a wide range of astrophysical systems satisfy this condition, and it is equivalent to claiming that both $\boldsymbol{\partial}_t$ and $\boldsymbol{\partial}_\phi$ are killing fields.

Second, at any point inside the disk, any field $\boldsymbol{\psi}(t,r,\theta,\phi)$ that reports a property of the gas may variate in time due to the turbulent motion of the flow. Thus, to assume that any field is time-independent and smooth enough in r for its flow to be described by Equation (5) means replacing such field by its average over an appropriate spacetime volume. The same process allows one to choose a natural set of variables that split the hydrodynamics into r-component equations and θ-component equations. The averaging process has been explained in [124,127,128]. We include the analysis here and try to explain it in a self-consistent manner. The turbulent motion is characterized by the eddies. The azimuthal extension of the largest eddies can be 2π, like waves crashing around an island, but their linear measure cannot be larger than the thickness of the disk, and as measured by an observer on the CRF, their velocity is in the order of $\beta^{\tilde{r}}$ so that their period along the r component is $\Delta\tilde{t} \approx (\text{Thickness})/\beta^{\tilde{r}}$ (e.g., §33, [129]). If we denote by H the average half-thickness of the disk as measured by this observer at r over the time $\Delta\tilde{t}$, then the appropriate volume $\mathcal{V}$ is composed by the points (t,r,θ,ϕ) such that $t \in [t^* - \Delta t/2, t^* + \Delta t/2]$, $\theta \in [\theta_{\rm min}, \theta_{\rm max}]$ and $\phi \in [0, 2\pi)$, where we have transformed $\Delta\tilde{t}$ and $\Delta\tilde{r}$ back to the CF using Equation (A4) as approximations. The values $\theta_{\rm min}$ and $\theta_{\rm max}$ correspond to the upper and lower faces of the disk, respectively. Then, the average takes the form

$$\boldsymbol{\psi}(t,r,\theta,\phi) \mapsto \boldsymbol{\psi}(r,\theta) = \langle \boldsymbol{\psi}(t,r,\theta,\phi) \rangle = \frac{\int_{t^*-\Delta t/2}^{t^*+\Delta t/2} \int_0^{2\pi} \boldsymbol{\psi}(r,t,\theta,\phi) \sqrt{\frac{-g}{g_{rr}g_{\theta\theta}}} dt d\phi}{\int_{t^*-\Delta t/2}^{t^*+\Delta t/2} \int_0^{2\pi} \sqrt{\frac{-g}{g_{rr}g_{\theta\theta}}} dt d\phi}. \tag{7}$$

The steady-state condition is achieved by requiring that the Lie derivative of the averaged quantity along the killing field $\boldsymbol{\partial}_t$ vanishes: $\mathcal{L}_{\boldsymbol{\partial}_t} \langle \boldsymbol{\psi} \rangle = 0$. Note that the thickness measurement performed by the observer already has an error $\sim M^2 a^2 H^3/6r^4$ since it extends the Lorentz frame beyond the local neighborhood, but if we assume that the disk is thin ($H/r \ll 1$), and we do, this error remains small. At the same time, we can take all metric components evaluated at the equator and use Equation (5) as the representative average velocity. Under these conditions, we have $\theta_{\rm max} - \theta_{\rm min} \approx 2H/r$, and the term $\sqrt{-g/g_{rr}}$ in Equation (7) cancels out. It becomes clear that an extra θ integral is what separates the radial and polar variables. In other words, the r-component variables are the vertically integrated fields

$$\boldsymbol{\psi}(r,\theta) \mapsto \boldsymbol{\psi}(r) = \int_{\theta_{\rm min}}^{\theta_{\rm max}} \boldsymbol{\psi}(r,\theta) \sqrt{g_{\theta\theta}} d\theta. \tag{8}$$

The vertical equations of motion can be obtained by setting up Newtonian (with relativistic corrections) equations for the field $\boldsymbol{\psi}(r,\theta)$ at each value of r (see, e.g., [99,127,130,131]).

2.2. Conservation Laws

The equations of evolution of the fluid are contained in the conservation laws $\nabla_\mu T^{\mu\nu} = 0$ and $\nabla_\mu(\rho u^\mu) = 0$. The most general stress–energy tensor for a Navier–Stokes viscous fluid with heat transfer is [132,133]

$$\boldsymbol{T} = \overbrace{(\rho + U + P)\boldsymbol{u}\otimes\boldsymbol{u} + P\boldsymbol{g}}^{\text{Ideal Fluid}} + \overbrace{(-2\eta\boldsymbol{\sigma} - \zeta(\boldsymbol{\nabla}\cdot\boldsymbol{u})\boldsymbol{P})}^{\text{Viscous Stress}} + \overbrace{\boldsymbol{q}\otimes\boldsymbol{u} + \boldsymbol{u}\otimes\boldsymbol{q}}^{\text{Heat flux}}, \tag{9}$$

where ρ, P, U, ζ, η, $\boldsymbol{q}$, $\boldsymbol{P}$ and $\boldsymbol{\sigma}$ are the rest-mass energy density, pressure, internal energy density, dynamic viscosity, bulk viscosity, heat-flux 4-vector, projection tensor and shear tensor, respectively, and thermodynamic quantities are measured on the LRF. We do not consider electromagnetic contributions and ignore the causality problems associated with the equations derived from this stress–energy tensor, since we are not interested in phenomena close to the horizon [124]. Before deriving the equations of motion and to add a simple model of neutrino oscillations to the dynamics of disk accretion, we must make some extra assumptions. We will assume that the θ integral in Equation (8) can be approximated by

$$\int_{\theta_{\min}}^{\theta_{\max}} \boldsymbol{\psi}\sqrt{g_{\theta\theta}}d\theta \approx \boldsymbol{\psi} r(\theta_{\max} - \theta_{\min}) \approx 2H\boldsymbol{\psi}, \tag{10}$$

for any field $\boldsymbol{\psi}$. Additionally, we use Stokes' hypothesis ($\zeta = 0$). Since we are treating the disk as a thin fluid in differential rotation, we will assume that, on average, the only non-zero component of the shearing stress on the CRF is $\sigma_{\tilde{r}\tilde{\phi}}$ (there are torques only on the ϕ direction), and $q_{\tilde{\theta}}$ is the only non-zero component of the energy flux (on average the flux is vertical). By $u^\mu\sigma_{\mu\nu} = 0$ and Equation (A7) we have

$$\sigma_{r\phi} = \frac{\gamma_{\hat{\phi}}^3}{2}\frac{g_{\phi\phi}}{\sqrt{\omega^2 g_{\phi\phi} - g_{tt}}}\partial_r\Omega\,, \quad \sigma_{rt} = -\Omega\sigma_{r\phi}. \tag{11}$$

Finally, the turbulent viscosity is estimated to be $\sim l\Delta u$ where l is the size of the turbulent eddies and Δu is the average velocity difference between points in the disk separated by a distance l. By the same arguments in (§33, [129]) and in Section 2.2, l can be at most equal to $2H$ and Δu can be at most equal to the isothermal sound speed $c_s = \sqrt{\partial P/\partial\rho}$ or else the flow would develop shocks [89]. The particular form of c_s can be calculated from Equation (15). This way we get

$$\eta = \Pi\nu_{\text{turb}} = 2\alpha\Pi H c_s, \tag{12}$$

with $\alpha \leq 1$ and $\Pi = \rho + U + P$. In a nutshell, this is the popular α-prescription put forward by [80]. As we mentioned at the end of Section 2.1, on the CRF for a fixed value of r, the polar equation takes the form of Euler's equation for a fluid at rest where the acceleration is given by the tidal gravitational acceleration. Namely, the θ component of the fluid's path-lines relative acceleration in the θ direction is

$$\frac{1}{r}\partial_\theta P \approx \rho r\cos\theta\left[\boldsymbol{R}\left(\boldsymbol{u},\boldsymbol{\partial}_{\tilde{\theta}},\boldsymbol{u}\right)\cdot\boldsymbol{\partial}_{\tilde{\theta}}\right]_{\theta=\pi/2}, \tag{13}$$

with $\boldsymbol{R}$ being the Riemann curvature tensor. With $u^{\tilde{\mu}} \approx (1,0,0,0)$, Equations (10) and (A8) and assuming that there is no significant compression of the fluid under the action of the tidal force, integration of this equation yields the relation up to second order in $\pi/2 - \theta$:

$$P = \frac{1}{2}\rho R^{\tilde{\theta}}{}_{\tilde{t}\tilde{\theta}\tilde{t}}\Big|_{\theta=\pi/2}\left(H^2 - r^2\left(\frac{\pi}{2} - \theta\right)^2\right), \tag{14}$$

where we used the condition $P = 0$ at the disk's surface. Hence, the average pressure inside the disk is (cf. [99,107,131])

$$P = \frac{1}{3}\rho H^2 R^{\tilde{\theta}}{}_{\tilde{t}\tilde{\theta}\tilde{t}}\Big|_{\theta=\pi/2}. \tag{15}$$

The equation of mass conservation is obtained by directly inserting into Equation (A13) the averaged density and integrating vertically to obtain

$$2Hr\rho u^r = \text{constant} = -\frac{\dot{M}}{2\pi}, \tag{16}$$

where the term $2Hr\rho u^r$ is identified as the average inward mass flux through a cylindrical surface of radius r per unit of azimuthal angle, and thus must be equal to the accretion rate divided by 2π. The same process applied to Equation (A12) yields the energy conservation equation:

$$u^r\left[\partial_r(HU) - \frac{U+P}{\rho}\partial_r(H\rho)\right] = 2\eta H\sigma^{r\phi}\sigma_{r\phi} - H\epsilon, \tag{17}$$

where factors proportional to H/r are ignored and we assume $\Pi \approx \rho$ to integrate the second term on the left-hand side. ϵ is the average energy density measured on the LRF (see the discussion around Equation (A16)). The first term on the right-hand side is the viscous heating rate F_{heat} and the second term is the cooling rate F_{cool}. The last constitutive equation is obtained by applying the zero torque at the last stable orbit condition. These relations are calculated in Appendix A. We just replace the density in Equation (16) using Equation (A21), obtaining

$$u^r = -\frac{4\alpha H c_s \sigma^r_\phi}{Mf(x,x^*)}. \tag{18}$$

2.3. Equations of State

We consider that the main contribution to the rest-mass energy density of the disk is made up of neutrons, protons and ions. This way $\rho = \rho_{\text{B}} = n_B m_B$ with baryon number density n_B and baryon mass m_B equal to the atomic unit mass. The disk's baryonic mass obeys Maxwell–Boltzmann statistics, and its precise composition is determined by the nuclear statistical equilibrium (NSE). We denote the mass fraction of an ion i by $X_i = \rho_i/\rho_B$ (if $i = p$ or n then we are referring to proton or neutrons) and it can be calculated by the Saha equation [134,135]

$$X_i = \frac{A_i m_B}{\rho} G_i \left(\frac{TA_i m_B}{2\pi}\right)^{3/2} \exp\left(\frac{Z_i\left(\mu_p + \mu_p^C\right) + N_i\mu_n - \mu_i^C + B_i}{T}\right), \tag{19}$$

with the constraints:

$$\sum_i X_i = 1, \quad \sum_i Z_i Y_i = Y_e. \tag{20}$$

In these equations, T, A_i, N_i, Z_i, Y_e, Y_i, G_i, μ_i and B_i are the temperature, atomic number, neutron number, proton number, electron fraction (electron abundance per baryon), ion abundance per baryon, nuclear partition function, chemical potential (including the nuclear rest-mass energy) and ion binding energy. The μ_i^C are the Coulomb corrections for the NSE state in a dense plasma (see Appendix C). The binding energy data for a large collection of nuclei can be found in [136] and the temperature-dependent partition functions are found in [137,138]. Even though we take into account Coulomb corrections in NSE, we assume that the baryonic mass can be described by an ideal gas[1,2] and

$$P_B = \sum_i P_i = n_B T \sum_i \frac{X_i}{A_i}, \quad U_B = \frac{3}{2}P_B. \tag{21}$$

[1] Since bulk viscosity effects appear as a consequence of correlations between ion velocities due to Coulomb interactions and of large relaxation times to reach local equilibrium, the NSE and ideal gas assumptions imply that imposing Stokes' hypothesis becomes de rigueur [133,139,140]

[2] We will consider accretion rates of up to $1M_\odot$ s^{-1}. These disks reach densities of 10^{13} g cm^{-3}. Baryons can be lightly degenerate at these densities but we will still assume that the baryonic mass can be described by an ideal gas.

The disk also contains photons, electrons, positrons, neutrinos and antineutrinos. As is usual in neutrino oscillations analysis, we distinguish only between electron (anti)neutrinos $\nu_e, (\bar{\nu}_e)$ and x (anti)neutrinos $\nu_x(\bar{\nu}_x)$, where $x = \mu + \tau$ is the superposition of muon neutrinos and tau neutrinos. Photons obey the usual relations

$$P_\gamma = \frac{\pi^2 T^4}{45}, \quad U_\gamma = 3P_\gamma, \tag{22}$$

while, for electrons and positrons we have

$$n_{e^\pm} = \frac{\sqrt{2}}{\pi^2}\xi^{3/2}[\mathcal{F}_{1/2,0}(\xi, \eta_{e^\pm}) + \xi\mathcal{F}_{3/2,0}(\xi, \eta_{e^\pm})], \tag{23a}$$

$$U_{e^\pm} = \frac{\sqrt{2}}{\pi^2}\xi^{5/2}[\mathcal{F}_{3/2,0}(\xi, \eta_{e^\pm}) + \xi\mathcal{F}_{5/2,0}(\xi, \eta_{e^\pm})], \tag{23b}$$

$$P_{e^\pm} = \frac{2\sqrt{2}}{3\pi^2}\xi^{5/2}\left[\mathcal{F}_{3/2,0}(\xi, \eta_{e^\pm}) + \frac{\xi}{2}\mathcal{F}_{5/2,0}(\xi, \eta_{e^\pm})\right], \tag{23c}$$

with $\xi = T/m_e$ and written in terms of the generalized Fermi functions

$$\mathcal{F}_{k,\ell}(y, \eta) = \int_\ell^\infty \frac{x^k\sqrt{1 + xy/2}}{\exp(x - \eta) + 1}dx. \tag{24}$$

In these equations $\eta_{e^\pm} = (\mu_{e^\pm} - m_e)/T$ is the electron (positron) degeneracy parameter without rest-mass contributions (not to be confused with η in Section 2.2). Since electrons and positrons are in equilibrium with photons due to the pair creation and annihilation processes $(e^- + e^+ \to 2\gamma)$, we know that their chemical potentials are related by $\mu_{e^+} = -\mu_{e^-}$, which implies $\eta_{e^+} = -\eta_{e^-} - 2/\xi$ from the charge neutrality condition, and we obtain

$$n_B Y_e = n_{e^-} - n_{e^+}. \tag{25}$$

For neutrinos, the story is more complicated. In the absence of oscillations and if the disk is hot and dense enough for neutrinos to be trapped within it and in thermal equilibrium, n_ν, U_ν, P_ν can be calculated with Fermi–Dirac statistics using the same temperature T

$$n^{\text{trapped}}_{\nu(\bar{\nu})} = \frac{T^3}{\pi^2}\mathcal{F}_{2,0}\left(\eta_{\nu(\bar{\nu})}\right), \tag{26a}$$

$$U^{\text{trapped}}_{\nu(\bar{\nu})} = \frac{T^4}{\pi^2}\mathcal{F}_{3,0}\left(\eta_{\nu(\bar{\nu})}\right), \tag{26b}$$

$$P^{\text{trapped}}_{\nu(\bar{\nu})} = \frac{U^{\text{trapped}}_{\nu(\bar{\nu})}}{3}, \tag{26c}$$

where it is understood that $\mathcal{F}(\eta) = \mathcal{F}(y = 0, \eta)$ with $\eta_{\nu(\bar{\nu})} = \mu_{\nu(\bar{\nu})}/T$ and the ultra-relativistic approximation $m_\nu \ll 1$ for any neutrino flavor is used. If thermal equilibrium is has not been achieved, Equation (26) cannot be used. Nevertheless, at any point in the disk and for given values of T and ρ, (anti)neutrinos are being created through several processes. The processes we take into account are pair annihilation $e^- + e^+ \to \nu + \bar{\nu}$, electron or positron capture by nucleons $p + e^- \to n + \nu_e$ or $n + e^+ \to p + \bar{\nu}_e$, electron capture by ions $A + e^- \to A' + \nu_e$, plasmon decay $\tilde{\gamma} \to \nu + \bar{\nu}$ and nucleon-nucleon bremsstrahlung $n_1 + n_2 \to n_3 + n_4 + \nu + \bar{\nu}$. The emission rates can be found in Appendix D. The chemical equilibria for these processes determine the values of $\eta_{\nu(\bar{\nu})}$. In particular,

$$\eta_{\nu_e} = \eta_{e^-} + \ln\left(\frac{X_p}{X_n}\right) + \frac{1-\mathbb{Q}}{\xi}, \tag{27a}$$

$$\eta_{\bar{\nu}_e} = -\eta_{\nu_e}, \tag{27b}$$

$$\eta_{\nu_x} = \eta_{\bar{\nu}_x} = 0, \tag{27c}$$

satisfy all equations. Here, $\mathbb{Q} = (m_n - m_p)/m_e \approx 2.531$. Once the (anti)neutrino number and energy emission rates (R_i, Q_i) are calculated for each process i, the (anti)neutrino thermodynamic quantities are given by

$$n^{\text{free}}_{\nu(\bar{\nu})} = H\sum_i R_{i,\nu(\bar{\nu})}, \tag{28a}$$

$$U^{\text{free}}_{\nu(\bar{\nu})} = H\sum_i Q_{i,\nu(\bar{\nu})}, \tag{28b}$$

$$P^{\text{free}}_{\nu(\bar{\nu})} = \frac{U^{\text{free}}_{\nu(\bar{\nu})}}{3}. \tag{28c}$$

Remember we are using Planck units, so in these expressions there should be an H/c instead of just an H. The transition for each (anti)neutrino flavor between both regimes occurs when Equations (26b) and (28b) are equal, and it can be simulated by defining the parameter

$$w_{\nu(\bar{\nu})} = \frac{U^{\text{free}}_{\nu(\bar{\nu})}}{U^{\text{free}}_{\nu(\bar{\nu})} + U^{\text{trapped}}_{\nu(\bar{\nu})}}. \tag{29}$$

With this equation, the (anti)neutrino average energy can be defined as

$$\langle E_{\nu(\bar{\nu})}\rangle = \left(1 - w_{\nu(\bar{\nu})}\right)\frac{U^{\text{free}}_{\nu(\bar{\nu})}}{n^{\text{free}}_{\nu(\bar{\nu})}} + w_{\nu(\bar{\nu})}\frac{U^{\text{trapped}}_{\nu(\bar{\nu})}}{n^{\text{trapped}}_{\nu(\bar{\nu})}}. \tag{30}$$

and the approximated number and energy density are

$$n_{\nu(\bar{\nu})} = \begin{cases} n^{\text{free}}_{\nu(\bar{\nu})}, & \text{if } w_{\nu(\bar{\nu})} < 1/2. \\ n^{\text{trapped}}_{\nu(\bar{\nu})}, & \text{if } w_{\nu(\bar{\nu})} \geq 1/2. \end{cases} \tag{31a}$$

$$U_{\nu(\bar{\nu})} = \begin{cases} U^{\text{free}}_{\nu(\bar{\nu})}, & \text{if } w_{\nu(\bar{\nu})} < 1/2. \\ U^{\text{trapped}}_{\nu(\bar{\nu})}, & \text{if } w_{\nu(\bar{\nu})} \geq 1/2. \end{cases} \tag{31b}$$

$$P_{\nu(\bar{\nu})} = \frac{U_{\nu(\bar{\nu})}}{3}. \tag{31c}$$

Note that both Equations (28c) and (31c) are approximations since they are derived from equilibrium distributions, but they help make the transition smooth. Besides, the neutrino pressure before thermal equilibrium is negligible. This method was presented in [107] where it was used only for electron (anti)neutrinos. The total (anti)neutrino number and energy flux through one the disk's faces can be approximated by

$$\dot{n}_{\nu_j(\bar{\nu}_j)} = \sum_{j\in\{e,x\}} \frac{n_{\nu_j(\bar{\nu}_j)}}{1+\tau_{\nu_j(\bar{\nu}_j)}}, \tag{32a}$$

$$F_{\nu_j(\bar{\nu}_j)} = \sum_{j\in\{e,x\}} \frac{U_{\nu_j(\bar{\nu}_j)}}{1+\tau_{\nu_j(\bar{\nu}_j)}}, \tag{32b}$$

where τ_{ν_i} is the total optical depth for the (anti)neutrino $\nu_i(\bar{\nu}_i)$. By collecting all the expressions, we write the total internal energy and total pressure as

$$U = \sum_{j\in\{e,x\}} \left(U_{\nu_j} + U_{\bar{\nu}_j}\right) + U_B + U_{e^-} + U_{e^+} + U_\gamma \ , \tag{33a}$$

$$P = \sum_{j\in\{e,x\}} \left(P_{\nu_j} + P_{\bar{\nu}_j}\right) + P_B + P_{e^-} + P_{e^+} + P_\gamma \ . \tag{33b}$$

The (anti)neutrino energy flux through the disk faces contributes to the cooling term in the energy conservation equation, but it is not the only one. Another important energy sink is photodisintegration of ions. To calculate it we proceed as follows. The energy spent to knocking off a nucleon of an ion i is equal to the binding energy per nucleon B_i/A_i. Now, consider a fluid element of volume V whose moving walls are attached to the fluid so that no baryons flow in or out. The total energy of photodisintegration contained within this volume is the sum over i of (energy per nucleon of ion i)$\times$(# of freed nucleons of ion i inside V). This can be written as $\sum_i (B_i/A_i) n_{f,i} V$, or, alternatively, $n_B V \sum_i (B_i/A_i) X_{f,i}$. If we approximate B_i/A_i by the average binding energy per nucleon $\bar{B}$ (which is a good approximation save for a couple of light ions) the expression becomes $n_B V \bar{B} \sum_i X_{f,i} = n_B V \bar{B} X_f = n_B V \bar{B}(X_p + X_n)$. We place the value of $\bar{B}$ in Section 4.

The rate of change of this energy on the LRF, denoting the proper time by λ, is

$$\frac{d}{d\lambda}\left[n_B V \bar{B}\left(X_p + X_n\right)\right] = n_B V \bar{B} \frac{d}{d\lambda}\left(X_p + X_n\right). \tag{34}$$

The derivative of $n_B V$ vanishes by baryon conservation. Transforming back to CF and taking the average we find the energy density per unit time used in disintegration of ions

$$\epsilon_{\text{ions}} = n_B \bar{B} u^r H \partial_r \left(X_p + X_n\right). \tag{35}$$

The average energy density measured on the LRF ϵ appearing in Equation (17) is

$$\epsilon = \epsilon_{\text{ions}} + \frac{1}{H} \sum_{i\in\{e,x\}} (F_{\nu_i} + F_{\bar{\nu}_i}). \tag{36}$$

Finally, a similar argument allows us to obtain the equation of lepton number conservation. For any lepton ℓ, the total lepton number density is $\sum_{\ell\in\{e,\mu,\tau\}}(n_\ell - n_{\bar{\ell}} + n_{\nu_\ell} - n_{\bar{\nu}_\ell})$. Thus, with Equation (25), calculating the rate of change as before, using Gauss's theorem and taking the average, we get

$$u^r H \left[n_B \partial_r Y_e + \partial_r \sum_{\ell\in\{e,x\}} (n_{\nu_\ell} - n_{\bar{\nu}_\ell}) \right] = \sum_{\ell\in\{e,x\}} (\dot{n}_{\bar{\nu}_\ell} - \dot{n}_{\nu_\ell}), \tag{37}$$

where the right-hand side represents the flux of lepton number through the disk's surface.

3. Neutrino Oscillations

To study the flavor evolution of neutrinos within a particular system, a Hamiltonian governing neutrino oscillation must be set up. The relative strengths of the potentials appearing in such a Hamiltonian depend on four elements: geometry, mass content, neutrino content and neutrino mass hierarchy. Geometry refers to the nature of net neutrino fluxes and possible gravitational effects. Mass and neutrino contents refer to respective distributions of leptons of each flavor (e, μ, τ) present in the medium. Finally, mass hierarchy refers to the relative values of the masses m_1, m_2, m_3 for each neutrino mass eigenstates (see Table 2). We dedicate this section to a detailed derivation of the equations of flavor evolution for a neutrino dominated accretion disk. To maintain consistency with the traditional literature of neutrino oscillations, we will reuse some symbols appearing in

previous sections. To avoid confusion, we point out that the symbols in this section are independent of the previous sections unless we explicitly draw a comparison.

Table 2. Mixing and squared mass differences as they appear in [141]. Error values in parentheses are shown in 3σ interval. The squared mass difference is defined as $\Delta m^2 = m_3^2 - \left(m_2^2 + m_1^2\right)/2$ and its sign depends on the hierarchy $m_1 < m_2 < m_3$ or $m_3 < m_1 < m_2$.

$\Delta m^2_{21} = 7.37\,(6.93 - 7.96) \times 10^{-5}$ eV^2
$\lvert\Delta m^2\rvert = 2.56\,(2.45 - 2.69) \times 10^{-3}$ eV^2 Normal Hierarchy
$\lvert\Delta m^2\rvert = 2.54\,(2.42 - 2.66) \times 10^{-3}$ eV^2 Inverted Hierarchy
$\sin^2\theta_{12} = 0.297\,(0.250 - 0.354)$
$\sin^2\theta_{23}(\Delta m^2 > 0) = 0.425\,(0.381 - 0.615)$
$\sin^2\theta_{23}(\Delta m^2 < 0) = 0.589\,(0.383 - 0.637)$
$\sin^2\theta_{13}(\Delta m^2 > 0) = 0.0215\,(0.0190 - 0.0240)$
$\sin^2\theta_{13}(\Delta m^2 < 0) = 0.0216\,(0.0190 - 0.0242)$

3.1. Equations of Oscillation

The equations that govern the evolution of an ensemble of mixed neutrinos are the Boltzmann collision equations

$$i\dot{\rho}_{\mathbf{p},t} = C\left(\rho_{\mathbf{p},t}\right), \tag{38a}$$
$$i\dot{\bar{\rho}}_{\mathbf{p},t} = C\left(\bar{\rho}_{\mathbf{p},t}\right). \tag{38b}$$

The collision terms should include the vacuum oscillation plus all possible scattering interactions that neutrinos undergo through their propagation. For free streaming neutrinos, only the vacuum term and the forward-scattering interactions are taken into account so that the equations become

$$i\dot{\rho}_{\mathbf{p},t} = \left[\mathsf{H}_{\mathbf{p},t}, \rho_{\mathbf{p},t}\right], \tag{39a}$$
$$i\dot{\bar{\rho}}_{\mathbf{p},t} = \left[\bar{\mathsf{H}}_{\mathbf{p},t}, \bar{\rho}_{\mathbf{p},t}\right]. \tag{39b}$$

Here, $\mathsf{H}_{\mathbf{p},t}$ ($\bar{\mathsf{H}}_{\mathbf{p},t}$) is the oscillation Hamiltonian for (anti)neutrinos and $\rho_{\mathbf{p},t}$ ($\bar{\rho}_{\mathbf{p},t}$) is the matrix of occupation numbers: $(\rho_{\mathbf{p},t})_{ij} = \langle a_j^\dagger a_i\rangle_{\mathbf{p},t}$ for neutrinos and $((\bar{\rho}_{\mathbf{p},t})_{ij} = \langle \bar{a}_i^\dagger \bar{a}_j\rangle_{\mathbf{p},t}$ for antineutrinos), for each momentum $\mathbf{p}$ and flavors i, j. The diagonal elements are the distribution functions $f_{\nu_i(\bar{\nu}_i)}(\mathbf{p})$ such that their integration over the momentum space gives the neutrino number density n_{ν_i} of a determined flavor i at time t. The off-diagonal elements provide information about the overlapping between the two neutrino flavors. Taking into account the current–current nature of the weak interaction in the standard model, the Hamiltonian for each equation is [142–144]

$$\mathsf{H}_{\mathbf{p},t} = \Omega_{\mathbf{p},t} + \sqrt{2}G_F\int\left(l_{\mathbf{q},t} - \bar{l}_{\mathbf{q},t}\right)\left(1 - \mathbf{v}_{\mathbf{q},t}\cdot\mathbf{v}_{\mathbf{p},t}\right)\frac{d^3\mathbf{q}}{(2\pi)^3} + \sqrt{2}G_F\int\left(\rho_{\mathbf{q},t} - \bar{\rho}_{\mathbf{q},t}\right)\left(1 - \mathbf{v}_{\mathbf{q},t}\cdot\mathbf{v}_{\mathbf{p},t}\right)\frac{d^3\mathbf{q}}{(2\pi)^3}, \tag{40a}$$
$$\bar{\mathsf{H}}_{\mathbf{p},t} = -\Omega_{\mathbf{p},t} + \sqrt{2}G_F\int\left(l_{\mathbf{q},t} - \bar{l}_{\mathbf{q},t}\right)\left(1 - \mathbf{v}_{\mathbf{q},t}\cdot\mathbf{v}_{\mathbf{p},t}\right)\frac{d^3\mathbf{q}}{(2\pi)^3} + \sqrt{2}G_F\int\left(\rho_{\mathbf{q},t} - \bar{\rho}_{\mathbf{q},t}\right)\left(1 - \mathbf{v}_{\mathbf{q},t}\cdot\mathbf{v}_{\mathbf{p},t}\right)\frac{d^3\mathbf{q}}{(2\pi)^3}. \tag{40b}$$

where G_F is the Fermi coupling constant, $\Omega_{\mathbf{p},t}$ is the matrix of vacuum oscillation frequencies, $l_{\mathbf{p},t}$ and $\bar{l}_{\mathbf{p},t}$ are matrices of occupation numbers for charged leptons built in a similar way to the neutrino matrices, and $\mathbf{v}_{\mathbf{p},t} = \mathbf{p}/p$ is the velocity of a particle with momentum $\mathbf{p}$ (either neutrino or charged lepton). As stated before, we will only consider two neutrino flavors: e and $x = \mu + \tau$. Three-flavor oscillations can be approximated by two-flavor oscillations as a result of the strong hierarchy of the squared mass differences $|\Delta m^2_{13}| \approx |\Delta m^2_{23}| \gg |\Delta m^2_{12}|$. In this case, only the smallest mixing angle θ_{13} is considered. We will drop the suffix for the rest of the discussion. Consequently, the relevant oscillations

are $\nu_e \rightleftharpoons \nu_x$ and $\bar{\nu}_e \rightleftharpoons \bar{\nu}_x$, and each term in the Hamiltonian governing oscillations becomes a 2×2 Hermitian matrix. Now, consider an observer on the LRF (which is almost identical to the CRF due to Equation (6) at a point r. In its spatial local frame, the unit vectors $\hat{x}, \hat{y}, \hat{z}$ are parallel to the unit vectors $\hat{r}, \hat{\theta}, \hat{\phi}$ of the CF, respectively. Solving Equation (39) in this coordinate system would yield matrices $\rho, \bar{\rho}$ as functions of time t. However, in our specific physical system, both the matter density and the neutrino density vary with the radial distance from the BH. This means that the equations of oscillations must be written in a way that makes explicit the spatial dependence, i.e., in terms of the coordinates x, y, z. For a collimated ray of neutrinos, the expression $dt = dr$ would be good enough, but for radiating extended sources or neutrino gases the situation is more complicated.

In Equation (39) we must replace the matrices of occupation numbers by the space-dependent Wigner functions $\rho_{\mathbf{p},\mathbf{x},t}$ (and $\bar{\rho}_{\mathbf{p},\mathbf{x},t}$) and the total time derivative by the Liouville operator [145,146]:

$$\dot{\rho}_{\mathbf{p},\mathbf{x},t} = \overbrace{\frac{\partial \rho_{\mathbf{p},\mathbf{x},t}}{\partial t}}^{\text{Explicit Time}} + \overbrace{\mathbf{v}_{\mathbf{p}} \cdot \nabla_{\mathbf{x}} \rho_{\mathbf{p},\mathbf{x},t}}^{\text{Drift}} + \overbrace{\dot{\mathbf{p}} \cdot \nabla_{\mathbf{p}} \rho_{\mathbf{p},\mathbf{x},t}}^{\text{External Forces}} . \tag{41}$$

In this context, $\mathbf{x}$ represents a vector in the LRF. In the most general case, finding $\rho_{\mathbf{p},\mathbf{x},t}$ and $\bar{\rho}_{\mathbf{p},\mathbf{x},t}$ means solving a 7D neutrino transport problem in the variables $x, y, z, p_x, p_y, p_z, t$. Since our objective is to construct a simple model of neutrino oscillations inside the disk, to obtain the specific form of Equation (39) we must simplify the equations by imposing on it conditions that are consistent with the assumptions made in Section 2.

- Due to axial symmetry, the neutrino density is constant along the $\mathbf{z}$ direction. Moreover, since neutrinos follow null geodesics, we can set $\dot{p}_z \approx \dot{p}_\phi = 0$.
- Within the thin disk approximation (as represented by Equation (10)) the neutrino and matter densities are constant along the $\mathbf{y}$ direction and the momentum change due to curvature along this direction can be neglected, that is, $\dot{p}_y \approx 0$.
- In the LRF, the normalized radial momentum of a neutrino can be written as $p_x = \pm r/\sqrt{r^2 - 2Mr + M^2a^2}$. Hence, the typical scale of the change of momentum with radius is $\Delta r_{p_x,\text{eff}} = |d \ln p_x / dr|^{-1} = (r/M)\left(r^2 - 2Mr + M^2a^2\right)/\left(Ma^2 - r\right)$, which obeys $\Delta r_{p_x,\text{eff}} > r_s$ for $r > 2r_{\text{in}}$. This means we can assume $\dot{p}_x \approx 0$ up to regions very close to the inner edge of the disk.
- We define an effective distance $\Delta r_{\rho,\text{eff}} = |d \ln(Y_e n_B)/dr|^{-1}$. For all the systems we evaluated, we found that it is comparable to the height of the disk ($\Delta r_{\rho,\text{eff}} \sim 2 - 5\, r_s$). This means that at any point of the disk we can calculate neutrino oscillations in a small regions assuming that both the electron density and neutrino densities are constant.
- We neglect energy and momentum transport between different regions of the disk by neutrinos that are recaptured by the disk due to curvature. This assumption is reasonable except for regions very close to the BH but is consistent with the thin disk model (see, e.g., [128]). We also assume initially that the neutrino content of neighboring regions of the disk (different values of r) do not affect each other. As a consequence of the results discussed above, we assume that at any point inside the disk and at any instant of time an observer can describe both the charged leptons and neutrinos as isotropic gases around small enough regions of the disk. This assumption is considerably restrictive but we will generalize it in Section 5.

The purpose of these approximations is twofold. On one hand, we can reduce the problem considerably, since they allow us to add the neutrino oscillations to a steady-state disk model by simply studying the behavior of neutrinos at each point of the disk using the constant values of density and temperature at that point. We will see in Section 5, that this assumption would correspond to a transient state of an accretion disk, since very fast neighboring regions of the disk start interacting. On the other hand, the approximations allow us to simplify the equations of oscillation considering that all but the first term in Equation (41) vanish, leaving only a time derivative. In addition, both terms of the form

$\mathbf{v}_{\mathbf{q},t} \cdot \mathbf{v}_{\mathbf{p},t}$ in Equation (40) average to zero so that $\rho_{\mathbf{p},\mathbf{x},t} = \rho_{p,t}$ and $\bar{\rho}_{\mathbf{p},\mathbf{x},t} = \bar{\rho}_{p,t}$. We are now in a position to derive the simplified equations of oscillation for this particular model. Let us first present the relevant equations for neutrinos. Due to the similarity between $\mathsf{H}_{p,t}$ and $\bar{\mathsf{H}}_{p,t}$, the corresponding equations for antineutrinos can be obtained analogously. For simplicity, we will drop the suffix t since the time dependence is now obvious. In the two-flavor approximation, ρ_p is a 2×2 Hermitian matrix and can be expanded in terms of the Pauli matrices σ_i and a polarization vector $\mathsf{P}_p = (\mathsf{P}^x, \mathsf{P}^y, \mathsf{P}^z)$ in the neutrino flavor space, such that

$$\rho_p = \begin{pmatrix} \rho_{ee} & \rho_{ex} \\ \rho_{xe} & \rho_{xx} \end{pmatrix} = \frac{1}{2}(f_p \mathbf{1} + \mathsf{P}_p \cdot \vec{\sigma}), \tag{42}$$

where $f_p = \mathrm{Tr}[\rho_p] = f_{\nu_e}(p) + f_{\nu_x}(p)$ is the sum of the distribution functions for ν_e and ν_x. Note that the z component of the polarization vector obeys

$$\mathsf{P}^z_p = f_{\nu_e}(p) - f_{\nu_x}(p). \tag{43}$$

Hence, this component tracks the fractional flavor composition of the system. Appropriately normalizing ρ_p allows one to define a survival and mixing probability

$$P_{p,\nu_e \to \nu_e} = \frac{1}{2}\left(1 + \mathsf{P}^z_p\right), \tag{44a}$$

$$P_{p,\nu_e \to \nu_x} = \frac{1}{2}\left(1 - \mathsf{P}^z_p\right). \tag{44b}$$

The Hamiltonian can be written as a sum of three interaction terms:

$$\mathsf{H} = \mathsf{H}_{\text{vacuum}} + \mathsf{H}_{\text{matter}} + \mathsf{H}_{\nu\nu}. \tag{45}$$

The first term is the Hamiltonian in vacuum [27]:

$$\mathsf{H}_{\text{vacuum}} = \frac{\omega_p}{2}\begin{pmatrix} -\cos 2\theta & \sin 2\theta \\ \sin 2\theta & \cos 2\theta \end{pmatrix} = \frac{\omega_p}{2}\mathbf{B} \cdot \vec{\sigma}, \tag{46}$$

where $\omega_p = \Delta m^2/2p$, $\mathbf{B} = (\sin 2\theta, 0, -\cos 2\theta)$ and θ is the smallest neutrino mixing angle in vacuum. The other two terms in Equation (40) are special since they make the evolution equations non-linear. Since we are considering that the electrons inside the form an isotropic gas, the vector $\mathbf{v}_\mathbf{q}$ in the first integral is distributed uniformly on the unit sphere and the factor $\mathbf{v}_\mathbf{q} \cdot \mathbf{v}_p$ averages to zero. After integrating the matter Hamiltonian is given by

$$\mathsf{H}_{\text{matter}} = \frac{\lambda}{2}\begin{pmatrix} 1 & 0 \\ 0 & -1 \end{pmatrix} = \frac{\lambda}{2}\mathbf{L} \cdot \vec{\sigma}, \tag{47}$$

where $\lambda = \sqrt{2}G_F(n_{e^-} - n_{e^+})$ is the charged current matter potential and $\mathbf{L} = (0, 0, 1)$. Similarly, the same product disappears in the last term and after integrating we get

$$\mathsf{H}_{\nu\nu} = \sqrt{2}G_F[\mathsf{P} - \bar{\mathsf{P}}] \cdot \vec{\sigma}. \tag{48}$$

Clearly, $\mathsf{P} = \int \mathsf{P}_p \, d\mathbf{p}/(2\pi)^3$. Introducing every Hamiltonian term in Equation (39), and using the commutation relations of the Pauli matrices, we find the equations of oscillation for neutrinos and antineutrinos for each momentum mode p:

$$\dot{\mathsf{P}}_p = \left[\omega_p \mathbf{B} + \lambda \mathbf{L} + \sqrt{2}G_F(\mathsf{P} - \bar{\mathsf{P}})\right] \times \mathsf{P}_p, \tag{49a}$$

$$\dot{\bar{\mathsf{P}}}_p = \left[-\omega_p \mathbf{B} + \lambda \mathbf{L} + \sqrt{2}G_F(\mathsf{P} - \bar{\mathsf{P}})\right] \times \bar{\mathsf{P}}_p, \tag{49b}$$

where we have assumed that the total neutrino distribution remains constant, $\dot{f}_p = 0$. This shows how the polarization vectors can be normalized. By performing the transformations $\mathsf{P}_p/f_p \mapsto \mathsf{P}_p$ and $\bar{\mathsf{P}}_p/\bar{f}_p \mapsto \bar{\mathsf{P}}_p$, and multiplying and dividing the last term by the total neutrino density Equation (49), we get

$$\dot{\mathsf{P}}_p = \left[\omega_p \mathbf{B} + \lambda \mathbf{L} + \mu \mathbf{D}\right] \times \mathsf{P}_p, \tag{50a}$$

$$\dot{\bar{\mathsf{P}}}_p = \left[-\omega_p \mathbf{B} + \lambda \mathbf{L} + \mu \mathbf{D}\right] \times \bar{\mathsf{P}}_p, \tag{50b}$$

$$\mathbf{D} = \frac{1}{n_{\nu_e} + n_{\nu_x}} \int \left(f_q \mathsf{P}_q - \bar{f}_q \bar{\mathsf{P}}_q\right) \frac{d\mathbf{q}}{(2\pi)^3}. \tag{50c}$$

These are the traditional forms of the equations in terms of the vacuum, matter and self-interaction potentials ω_p, λ and μ with

$$\mu = \sqrt{2} G_F \sum_{i \in \{e,x\}} n_{\nu_i}. \tag{51}$$

Different normalization schemes are possible (see, e.g., [36,49,144,147]). Assuming that we can solve the equations of oscillation with constant potentials λ and μ simplifies the problem even further. Following [29], with the vector transformation (a rotation around the z axis of flavor space)

$$R_z = \begin{pmatrix} \cos(\lambda t) & \sin(\lambda t) & 0 \\ -\sin(\lambda t) & \cos(\lambda t) & 0 \\ 0 & 0 & 1 \end{pmatrix}, \tag{52}$$

Equation (50) becomes

$$\dot{\mathsf{P}}_p = \left[\omega_p \mathbf{B} + \mu \mathbf{D}\right] \times \mathsf{P}_p, \tag{53a}$$

$$\dot{\bar{\mathsf{P}}}_p = \left[-\omega_p \mathbf{B} + \mu \mathbf{D}\right] \times \bar{\mathsf{P}}_p, \tag{53b}$$

eliminating the λ potential, but making $\mathbf{B}$ time dependent. By defining the vector $\mathbf{S}_p = \mathsf{P}_p + \bar{\mathsf{P}}_p$, and adding and subtracting Equations (53a) and (53b) we get

$$\dot{\mathbf{S}}_p = \omega_p \mathbf{B} \times \mathbf{D}_p + \mu \mathbf{D} \times \mathbf{S}_p \approx \mu \mathbf{D} \times \mathbf{S}_p, \tag{54a}$$

$$\dot{\mathbf{D}}_p = \omega_p \mathbf{B} \times \mathbf{S}_p + \mu \mathbf{D} \times \mathbf{D}_p \approx \mu \mathbf{D} \times \mathbf{D}_p. \tag{54b}$$

The last approximation is true if we assume that the self-interaction potential is larger than the vacuum potential $\omega_p/\mu \ll 1$. We will show in Section 5 that this is the case for thin disks. The first equation implies that all the vectors $\mathbf{S}_p$ and their integral $\mathbf{S}$ evolve in the same way, suggesting the relation $\mathbf{S}_p = \left(f_p + \bar{f}_p\right)\mathbf{S}$. By replacing in Equation (54b) and integrating

$$\dot{\mathbf{S}} = \mu \mathbf{D} \times \mathbf{S}, \tag{55a}$$

$$\dot{\mathbf{D}} = \langle \omega \rangle \mathbf{B} \times \mathbf{S}. \tag{55b}$$

where $\langle \omega \rangle = \int \omega_p \left(f_p + \bar{f}_p\right) d\mathbf{p}/(2\pi)^3$ is the average vacuum oscillation potential. The fact that in our model the equations of oscillations can be written in this way has an important consequence. Usually, as it is done in supernovae neutrino oscillations, to solve Equation (50) we would need the neutrino distributions throughout the disk. If neutrinos are trapped, their distribution is given by Equation (26). If neutrinos are free, their temperature is not the same as the disk's temperature. Nonetheless, we can approximate the neutrino distribution in this regime by a Fermi–Dirac distribution with the same chemical potential as defined by Equation (27) but with an effective temperature T_ν^{eff}. This tempera-

ture can be obtained by solving the equation $\langle E_\nu \rangle = U(T_\nu^{\rm eff}, \eta_\nu)/n(T_\nu^{\rm eff}, \eta_\nu)$ which gives

$$T^{\rm eff}_{\nu_x,\bar{\nu}_x} = \langle E_{\nu_x,\bar{\nu}_x} \rangle \frac{180\,\zeta(3)}{7\pi^4}, \tag{56a}$$

$$T^{\rm eff}_{\nu_e,\bar{\nu}_e} = \frac{\langle E_{\nu_e,\bar{\nu}_e} \rangle}{3} \frac{{\rm Li}_3(-\exp(\eta_{\nu_e,\bar{\nu}_e}))}{{\rm Li}_4(-\exp(\eta_{\nu_e,\bar{\nu}_e}))}, \tag{56b}$$

where $\zeta(3)$ is Apéry's constant (ζ is the Riemann zeta function) and ${\rm Li}_s(z)$ is Jonquière's function. For convenience and considering the range of values that the degeneracy parameter reaches (see Section 6), we approximate the effective temperature of electron neutrinos and antineutrinos with the expressions

$$T^{\rm eff}_{\nu_e} = \frac{\langle E_{\nu_e} \rangle}{3}\left(a\eta^2_{\nu_e} + b\eta_{\nu_e} + c\right), \tag{57a}$$

$$T^{\rm eff}_{\bar{\nu}_e} = \frac{\langle E_{\bar{\nu}_e} \rangle}{3}. \tag{57b}$$

with constants $a = 0.0024$, $b = -0.085$, $c = 0.97$. However, Equation (55) allows us to consider just one momentum mode, and the rest of the spectrum behaves in the same way.

4. Initial Conditions and Integration

In the absence of oscillations, we can use Equations (15), (17) and (37) to solve for the set of functions $\eta_{e^-}(r)$, $\xi(r)$ and $Y_e(r)$ using as input parameters the accretion rate $\dot{M}$, the dimensionless spin parameter a, the viscosity parameter α and the BH mass M. From [99,107] we learn that neutrino dominated disks require accretion between 0.01 $M_\odot$ s^{-1} and 1 $M_\odot$ s^{-1} (this accretion rate range varies depending on the value of α). For accretion rates smaller than the lower value, the neutrino cooling is not efficient, and for rates larger than the upper value, the neutrinos are trapped within the flow. We also limit ourselves to the above accretion rate range, since it is consistent with the one expected to occur in a BdHN (see, e.g., [57,63,70]). We also know that s high spin parameter, high accretion rate, high BH mass and low viscosity parameter produce disks with higher density and higher temperature. This can be explained using the fact that several variables of the disk, such as pressure, density and height, are proportional to a positive power of M and a positive power of the quotient $\dot{M}/\alpha$. To avoid this semi-degeneracy in the system, we reduce the parameter space, and considering that we want to focus on the study of the oscillation dynamics inside the disk, we fix the BH mass at $M = 3M_\odot$, the viscosity parameter at $\alpha = 0.01$ and the spin parameter at $a = 0.95$ while changing the accretion rate. These values also allow us to compare our results with earlier disk models. Equations (17) and (37) are first-order ordinary differential equations, and since we perform the integration from an external (far away) radius $r_{\rm out}$ up to the innermost stable circular orbit $r_{\rm in}$, we must provide two boundary conditions at $r_{\rm out}$. Following the induced gravitational collapse (IGC) paradigm of GRBs associated with type Ib/c supernovae we assume that at the external edge of the disk, the infalling matter is composed mainly by the ions present in the material ejected from an explosion of a carbon–oxygen core, that is, mainly oxygen and electrons. This fixes the electron fraction $Y_e(r_{\rm out}) = 0.5$. We can also calculate the average binding energy per nucleon that appears in Equation (34) using the data in [136]. To establish the NSE we consider H2, H3, HE3, HE4, LI6, LI7, BE7, BE9, BE10, B10, B11, C11, C12, C13, C14, N13, N14, N15, O14, O15, O16, O17 and O18, and obtain the value of the average binding energy per nucleon $\bar{B} = 6.35$ MeV. The second boundary condition can be obtained by the relation $(T\eta + m_B)\sqrt{g_{tt}} =$ constant [148–150], with η being the degeneracy parameter of the fluid. If we require the potentials to vanish at infinity and invoke Euler's theorem, we arrive at the relation in the weak field limit

$$\frac{M}{r_{\rm out}} = \left.\frac{\rho + U + P - TS}{\rho}\right|_{r=r_{\rm out}}. \tag{58}$$

For a classical gas composed of ions and electrons, this relation becomes

$$\frac{M}{r_{\rm out}} \lesssim \frac{U}{\rho}\bigg|_{r=r_{\rm out}}. \tag{59}$$

That is, the virial specific energy must be smaller or comparable to the energy per baryon. Equation (59) can be used together with Equations (15) and (33) to solve for $\eta_{e^-}(r_{\rm out})$, $\xi(r_{\rm out})$. The value of $r_{\rm out}$ is chosen to be at most the circularization radius of the accreting material as described in [63,69]. We can estimate this radius by solving for r in the expression of the angular momentum per unit mass for a equatorial circular orbits. Hence, using Equation (5) we need to solve

$$u_\phi = M\frac{x^2-2x+a^2}{x^{3/2}\sqrt{x^3-3x+2a}} \sim 3\times 10^7 \text{ cm}, \tag{60}$$

where $x = \sqrt{r/M}$ which yields $r_{\rm out} \sim 1800 r_s$ and the expression is in geometric units. Finally, for the initial conditions to be accepted, they are evaluated by the gravitational instability condition [151]:

$$\sqrt{R^{\tilde{\theta}}{}_{\tilde{t}\tilde{\theta}\tilde{t}}\Big|_{\theta=\pi/2}}\,\Omega \geq 2\sqrt{3}\pi\rho. \tag{61}$$

Integration of the equations proceeds as follows: With the initial conditions we solve Equation (37) to obtain the electron fraction in the next integration point. With the new value of the electron fraction we solve the differential algebraic system of Equations (15) and (17) at this new point. This process continues until the innermost stable circular orbit $r_{\rm in}$ is reached.

To add the dynamics of neutrino oscillations we proceed the same as before, but at each point of integration, once the values of Y_e, η and ξ are found, we solve Equation (50) for the average momentum mode to obtain the survival probabilities as a function of time. We then calculate the new neutrino and antineutrino distributions with the conservation of total number density and the relations

$$n^{\rm new}_{\nu_e}(t) = P_{\nu_e\to\nu_e}(t)n_{\nu_e} + [1-P_{\nu_e\to\nu_e}(t)]n_{\nu_x}, \tag{62a}$$
$$n^{\rm new}_{\nu_x}(t) = P_{\nu_x\to\nu_x}(t)n_{\nu_x} + [1-P_{\nu_x\to\nu_x}(t)]n_{\nu_e}. \tag{62b}$$

Since the disk is assumed to be in a steady-state, we then perform a time average of Equation (62) as discussed in Section 2. With the new distributions, we can calculate the new neutrino and antineutrino average energies and use them to re-integrate the disk equations.

Neutrino emission within neutrino-cooled disks is dominated by electron and positron capture, which only produces electron (anti)neutrinos. The second most important process is electron–positron annihilation, but it is several orders of magnitude smaller. In Figure 2 we show the total number emissivity for these two processes for an accretion rate of $\dot{M} = 0.1 M_\odot$ s $^{-1}$. Other cases behave similarly. Moreover, although the degeneracy parameter suppresses the positron density, a high degeneracy limit does not occur in the disk and the degeneracy is kept low at values between about 0.2 and 3, as shown in Figure 3. The reason for this is the effect of high degeneracy on neutrino cooling. Higher degeneracy leads to a lower density of positrons, which suppresses the neutrino production and emission, which in turn leads to a lower cooling rate, higher temperature, lower degeneracy and higher positron density. This equilibrium leads, via the lepton number conservation Equation (37), to a balance between electronic and non-electronic neutrino densities within the inner regions of the disk. Given this fact, to solve the equations of oscillations, we can approximate the initial conditions of the polarization vectors with

$$\mathsf{P} = \bar{\mathsf{P}} \approx (0,0,1). \tag{63}$$

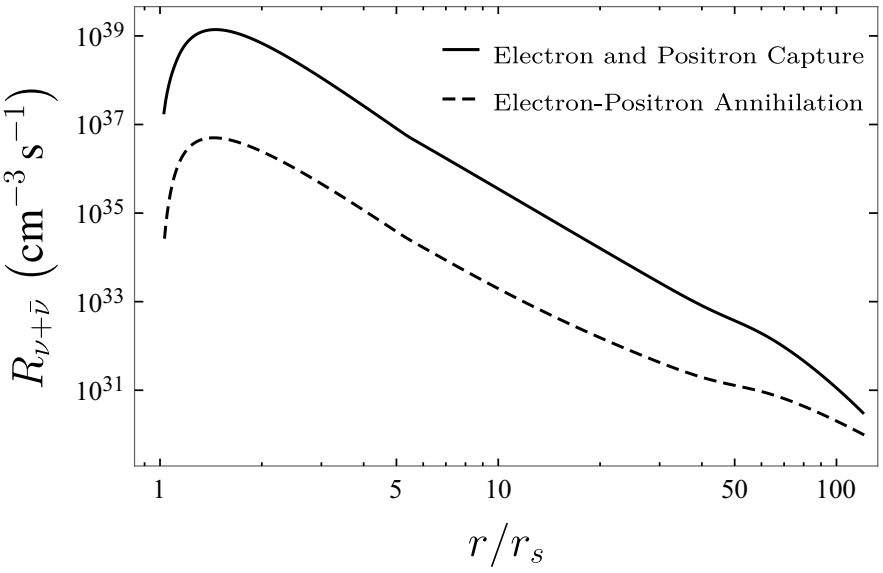

Figure 2. Total number emissivity for electron and positron capture ($p + e^- \rightarrow n + \nu_e$, $n + e^+ \rightarrow p + \bar{\nu}_e$) and electron–positron annihilation ($e^- + e^+ \rightarrow \nu + \bar{\nu}$) for accretion disks with $\dot{M} = 0.1 M_\odot$ s^{-1} between the inner radius and the ignition radius.

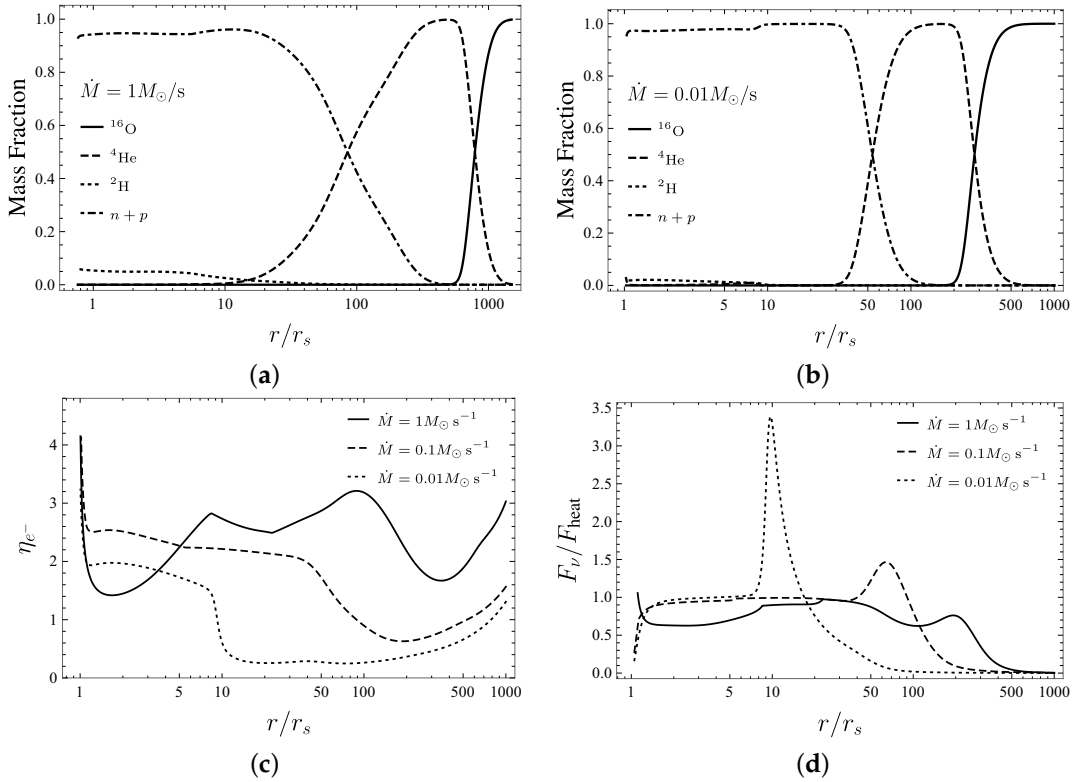

Figure 3. *Cont.*

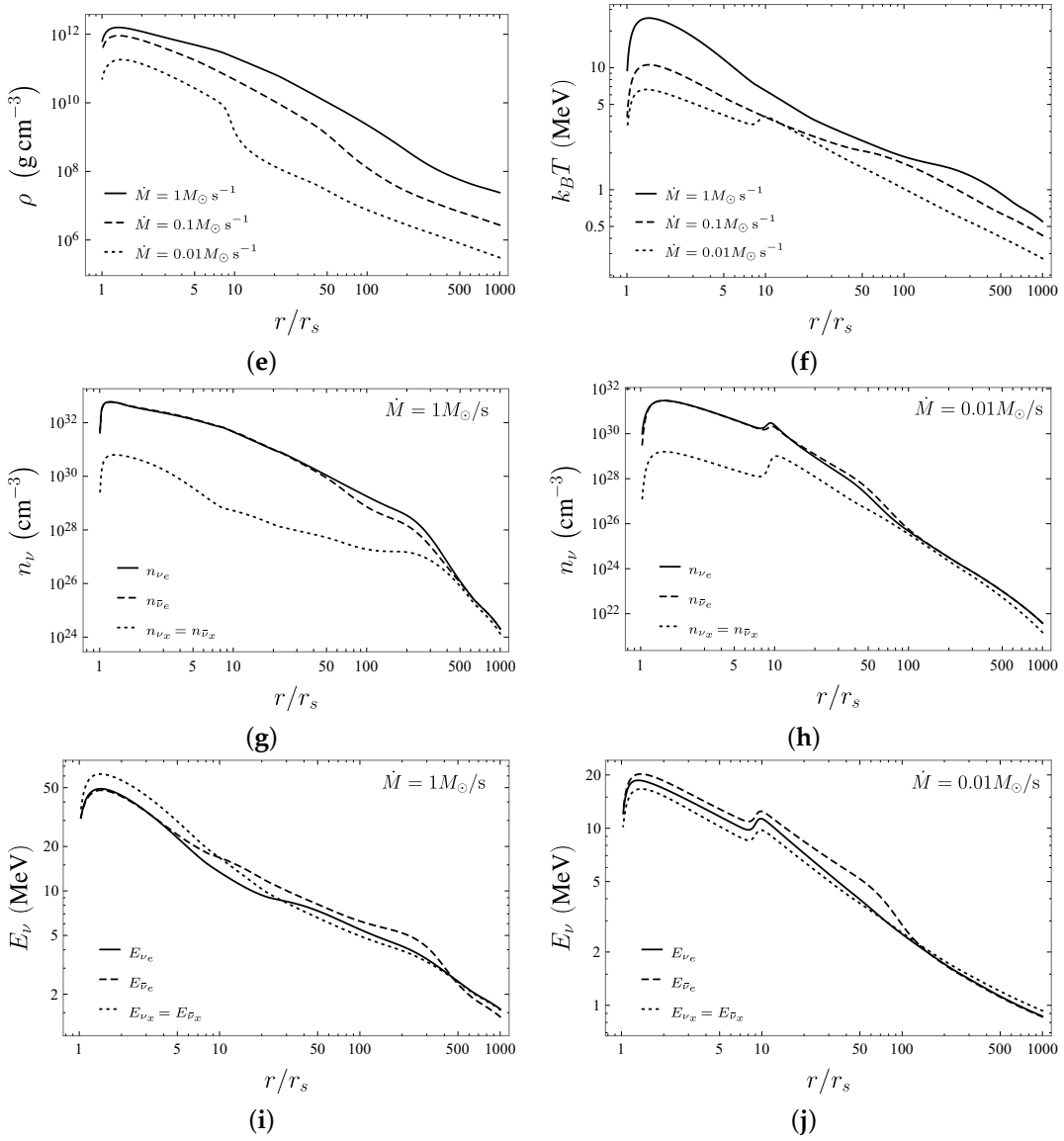

Figure 3. Properties of accretion disks in the absence of oscillations with $M = 3M_\odot$, $\alpha = 0.01$, $a = 0.95$. (**a**,**b**) The mass fraction inside the disk. We have plotted only the ones that appreciably change. (**c**) The electron degeneracy parameter. (**d**) The comparison between the neutrino cooling flux F_ν and the viscous heating F_{heat}. (**e**) The baryon density. (**f**) The temperature. (**g**,**h**) The neutrino number density. (**i**,**j**) The average neutrino energies.

5. Results and Analysis

In Figures 3 and 4, we present the main features of accretion disks for the parameters $M = 3M_\odot$; $\alpha = 0.01$; $a = 0.95$; and two selected accretion rates, $\dot{M} = 1M_\odot$ s^{-1} and $\dot{M} = 0.01M_\odot$ s^{-1}. It exhibits the usual properties of thin accretions disks. High accretion rate disks have higher density, temperature and electron degeneracy. Additionally, for high accretion rates, the cooling due to photodisintegration and neutrino emission kicks in at larger radii. For all cases, as the disk heats up, the number of free nucleons starts to increase enabling the photodisintegration cooling at $r \sim (100\text{–}300)r_s$. Only the disintegration of alpha particles is important, and the nucleon content of the infalling matter is of little consequence for the dynamics of the disk. When the disk reaches temperatures $\sim$1.3 MeV, the electron capture switches on, the neutrino emission becomes significant and the physics of the disk is dictated by the energy equilibrium between F_{heat} and F_ν. The radius at which neutrino cooling becomes significant (called ignition radius r_{ign}) is defined by the condition $F_\nu \sim F_{\text{heat}}/2$. For the low accretion rate $\dot{M} = 0.01M_\odot$ s^{-1}, the photodisintegration cooling finishes before the neutrino cooling becomes significant; this leads to fast heating of the

disk. Then the increase in temperature triggers a strong neutrino emission that carries away the excess heat generating a sharp spike in F_ν surpassing F_{heat} by a factor of $\sim$3.5. This behavior is also present in the systems studied in [107], but there it appears for fixed accretion rates and high viscosity ($\alpha = 0.1$). This demonstrates the semi-degeneracy mentioned in Section 5. The evolution of the fluid can be tracked accurately through the degeneracy parameter. At the outer radius, η_{e^-} starts to decrease as the temperature of the fluid rises. Once neutrino cooling becomes significant, it starts to increase until the disk reaches the local balance between heating and cooling. At this point, η_{e^-} stops rising and is maintained (approximately) at a constant value. Very close to r_{in}, the zero torque condition of the disk becomes important and the viscous heating is reduced drastically. This is reflected in a sharp decrease in the fluid's temperature and increase in the degeneracy parameter. For the high accretion rate, an additional effect has to be taken into account. Due to high ν_e optical depth, neutrino cooling is less efficient, leading to an increase in temperature and a second dip in the degeneracy parameter. This dip is not observed in low accretion rates because τ_{ν_e} does not reach significant values.

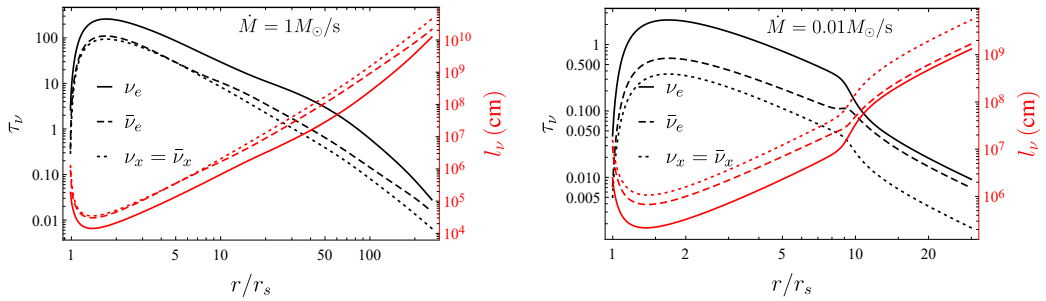

Figure 4. Total optical depth (left scale) and mean free path (right scale) for neutrinos and antineutrinos of both flavors between the inner radius and the ignition radius for accretion disks with (**a**) $\dot{M} = 1M_\odot\ \text{s}^{-1}$ and (**b**) $0.01M_\odot\ \text{s}^{-1}$.

With the information in Figure 3 we can obtain the oscillation potentials which we plot in Figure 5. Since the physics of the disk for $r < r_{\text{ign}}$ are independent of the initial conditions at the external radius and for $r > r_{\text{ign}}$ the neutrino emission is negligible, the impact of neutrino oscillations is important only inside r_{ign}.

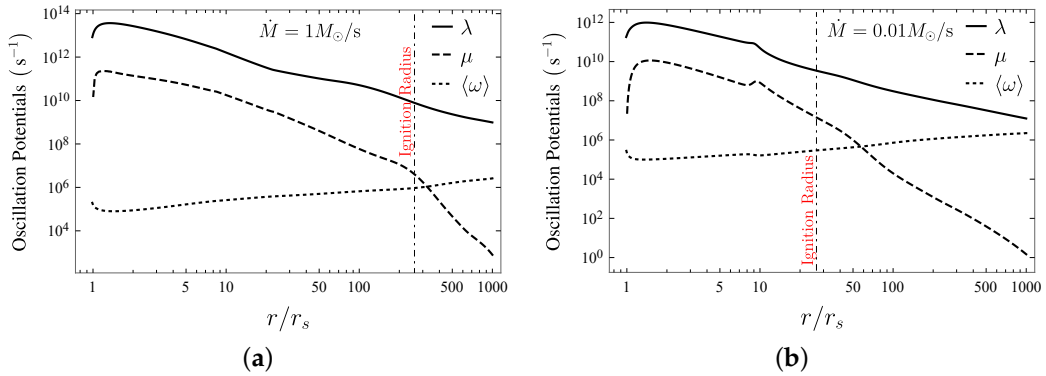

Figure 5. Oscillation potentials as functions of r with $M = 3M_\odot$, $\alpha = 0.01$, $a = 0.95$ for accretion rates (**a**) $\dot{M} = 1M_\odot\ \text{s}^{-1}$ and (**b**) $\dot{M} = 0.01M_\odot\ \text{s}^{-1}$, respectively. The vertical line represents the position of the ignition radius.

We can see that the discussion at the end of Section 3.1 is justified since, for $r_{\text{in}} < r < r_{\text{ign}}$, the potentials obey the relation

$$\langle\omega\rangle \ll \mu \ll \lambda. \tag{64}$$

Generally, the full dynamics of neutrino oscillations are a rather complex interplay between the three potentials, yet it is possible to understand the neutrino response in the disk using some numerical and algebraic results obtained in [33,36,144] and references therein. Specifically, we know that if $\mu \gg \langle\omega\rangle$, as long as the MSW condition $\lambda \simeq \langle\omega\rangle$ is not met (precisely our case), collective effects should dominate the neutrino evolution even if $\lambda \gg \mu$. On the other hand, if $\mu \lesssim \langle\omega\rangle$, the neutrino evolution is driven by the relative values between the matter and vacuum potentials (not our case). With Equation (55) we can build a very useful analogy. These equations are analogous to the equations of motion of a simple mechanical pendulum with a vector position given by $\mathbf{S}$, precessing around with angular momentum $\mathbf{D}$, subjected to a gravitational force $\langle\omega\rangle\mu\mathbf{B}$ with mass μ^{-1}. Using Equation (63) obtains the expression $|\mathbf{S}| = S \approx 2 + O(\langle\omega\rangle/\mu)$. Calculating $\partial_t(\mathbf{S}\cdot\mathbf{S})$, it can be checked that this value is conserved up to fluctuations of order $\langle\omega\rangle/\mu$. The analogous angular momentum is $\mathbf{D} = \mathsf{P} - \bar{\mathsf{P}} = 0$. Thus, the pendulum moves initially in a plane defined by $\mathbf{B}$ and the z-axis, i.e., the plane xz. Then, it is possible to define an angle φ between $\mathbf{S}$ and the z-axis such that

$$\mathbf{S} = S(\sin\varphi, 0, \cos\varphi). \tag{65}$$

The only non-zero component of $\mathbf{D}$ is the y-component. From Equation (55) we find

$$\dot{\varphi} = \mu D, \tag{66a}$$
$$\dot{D} = -\langle\omega\rangle S\cos(\varphi + 2\theta). \tag{66b}$$

These equations can be equivalently written as

$$\ddot{\varphi} = -k^2\sin(2\theta + \varphi), \tag{67}$$

where we have introduced the inverse characteristic time k by

$$k^2 = \langle\omega\rangle\mu S, \tag{68}$$

which is related to the anharmonic oscillations of the pendulum. The role of the matter potential λ is to logarithmically extend the oscillation length by the relation [144]

$$\tau = -k^{-1}\ln\left[\frac{k}{\theta(k^2+\lambda^2)^{1/2}}\left(1 + \frac{\langle\omega\rangle}{S\mu}\right)\right]. \tag{69}$$

The total oscillation time can then be approximated by the period of an harmonic pendulum plus the logarithmic extension

$$t_{\rm osc} = \frac{2\pi}{k} + \tau. \tag{70}$$

The initial conditions of Equation (63) imply

$$\varphi(t=0) = \arcsin\left(\frac{\langle\omega\rangle}{S\mu}\sin 2\theta\right), \tag{71}$$

so that φ is a small angle. The potential energy for a simple pendulum is

$$V(\varphi) = k^2[1 - \cos(\varphi + 2\theta)] \approx k^2(\varphi + 2\theta)^2. \tag{72}$$

If $k^2 > 0$, which is true for the normal hierarchy $\Delta m^2 > 0$, we expect small oscillations around the initial position since the system begins in a stable position of the potential. The magnitude of flavor conversions is in the order $\sim\langle\omega\rangle/S\mu \ll 1$. We stress that normal hierarchy does not mean an absence of oscillations but rather imperceptible oscillations in P_z. No strong flavor oscillations are expected. On the contrary, for the inverted hierarchy $\Delta m^2 < 0$, $k^2 < 0$ and the initial φ indicates that the system begins in an unstable position and we expect very large anharmonic oscillations. P^z (and $\bar{\mathsf{P}}^z$) oscillates between two

different maxima, passing through a minimum $-\mathsf{P}^z$ ($-\bar{\mathsf{P}}^z$) several times. This implies total flavor conversion: all electronic neutrinos (antineutrinos) are converted into non-electronic neutrinos (antineutrinos) and vice versa. This has been called bipolar oscillation in the literature [44]. If the initial conditions are not symmetric as in Equation (63), the asymmetry is measured by a constant $\varsigma = \bar{\mathsf{P}}^z/\mathsf{P}^z$ if $\bar{\mathsf{P}}^z < \mathsf{P}^z$ or $\varsigma = \mathsf{P}^z/\bar{\mathsf{P}}^z$ if $\bar{\mathsf{P}}^z > \mathsf{P}^z$ so that $0 < \varsigma < 1$. Bipolar oscillations are present in an asymmetric system as long as the relation

$$\frac{\mu}{|\langle\omega\rangle|} < 4\frac{1+\varsigma}{(1-\varsigma)^2}, \tag{73}$$

is obeyed [144]. If this condition is not met, instead of bipolar oscillation we get synchronized oscillations. Since we are considering constant potentials, synchronized oscillations are equivalent to the normal hierarchy case. From Figure 5 we can conclude that in the normal hierarchy case, neutrino oscillations have no effects on neutrino-cooled disks under the assumptions we have made. On the other hand, in the inverted hierarchy case, we expect extremely fast flavor conversions with periods of order $t_{\rm osc} \sim (10^{-9}$–$10^{-5})$ s for high accretion rates and $t_{\rm osc} \sim (10^{-8}$–$10^{-5})$ s for low accretion rates, between the respective $r_{\rm in}$ and $r_{\rm ign}$.

For the purpose of illustration we solve the equations of oscillations for the $\dot{M} = 0.1 M_\odot$ s^{-1} case at $r = 10 r_s$. The electronic (anti)neutrino survival probability at this point is shown in Figure 6 for inverted hierarchy and normal hierarchy, respectively. On both plots, there is no difference between the neutrino and antineutrino survival probabilities. This should be expected, since for these values of r, the matter and self-interaction potentials are much larger than the vacuum potential, and there is virtually no difference between Equations (50a) and (50b). Additionally, as mentioned before, note that the (anti)neutrino flavor proportions remain virtually unchanged for normal hierarchy, while the neutrino flavor proportions change drastically for the inverted hierarchy case. The characteristic oscillation time of the survival probability in inverted hierarchy found on the plot is

$$t_{\rm osc} \approx 8.4 \times 10^{-7}\,\text{s}, \tag{74}$$

which agrees with the ones given by Equation (70) up to a factor of order one. Such a small value suggests extremely quick $\nu_e\bar{\nu}_e \to \nu_x\bar{\nu}_x$ oscillations. A similar effect occurs for regions of the disk inside the ignition radius for all three accretion rates. In this example, the time average of the survival probabilities yields the values $\langle P_{\nu_e\to\nu_e}\rangle = \langle P_{\bar{\nu}_e\to\bar{\nu}_e}\rangle = 0.92$. With this number and Equations (62) and (57), the (anti)neutrino spectrum for both flavors can be constructed. However, more importantly, this means that the local observer at that point in the disk measures, on average, an electron (anti)neutrino loss of around 8%, which is represented by an excess of non-electronic (anti)neutrinos.

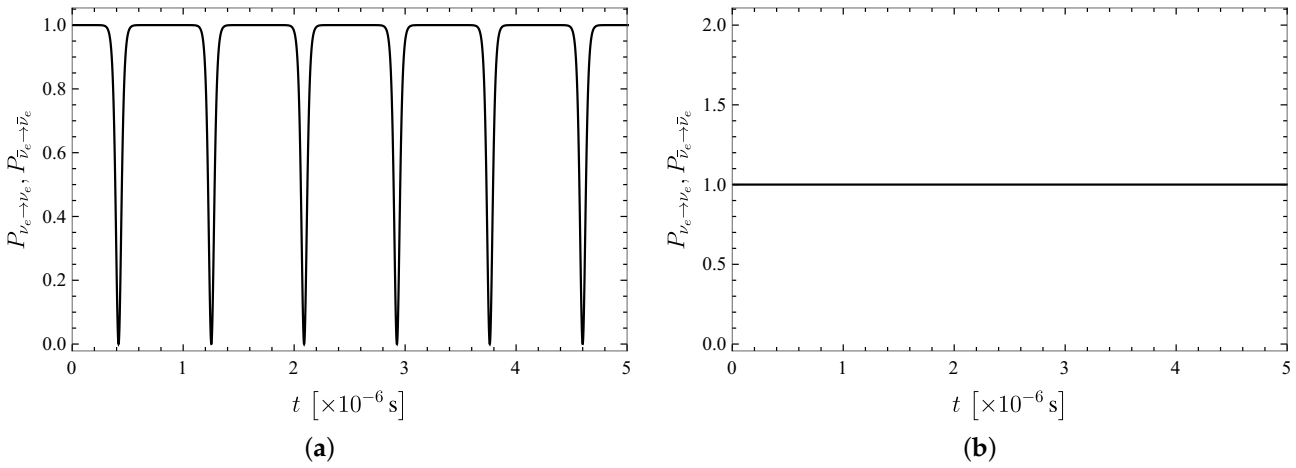

Figure 6. Survival provability for electron neutrinos and antineutrinos for the accretion disk with $\dot{M} = 0.1 M_\odot$ s^{-1} at $r = 10 r_s$. The survival probabilities for neutrinos and antineutrinos in both plots coincide. (**a**) Inverted hierarchy and (**b**) normal hierarchy.

In Section 3.1 we proposed to calculate neutrino oscillations assuming that small neighboring regions of the disk are independent and that neutrinos can be viewed as isotropic gases in those regions. However, this cannot be considered a steady-state of the disk. To see this, consider Figure 4. The maximum value of the neutrino optical depth is in the order of 10^3 for the highest accretion rate, meaning that the time that takes neutrinos to travel a distance of one Schwarzschild inside the disk radius obeys

$$t_{r_s} \ll \text{Max}(\tau_\nu) r_s \approx 10^{-2}\,\text{s}, \tag{75}$$

which is lower than the accretion time of the disk as discussed in Section 2 but higher than the oscillation time. Different sections of the disk are not independent, since they very quickly share (anti)neutrinos created with a non-vanishing momentum along the radial direction. Furthermore, the oscillation patterns between neighboring regions of the disk are not identical. In Figure 7 we show the survival probability as a function of time for different (but close) values of r for $\dot{M} = 0.1 M_\odot\ \text{s}^{-1}$. The superposition between neutrinos with different oscillation histories has several consequences: (1) It breaks the isotropy of the gas because close to the BH, neutrinos are more energetic and their density is higher, producing a radially directed net flux, meaning that the factor $\mathbf{v}_{\mathbf{q},t} \cdot \mathbf{v}_{\mathbf{p},t}$ does not average to zero. This implies that realistic equations of oscillations include a multi-angle term and a radially decaying neutrino flux similar to the situation in SN neutrinos. (2) It constantly changes the neutrino content at any value of r independently of the neutrino collective evolution given by the values of the oscillation potentials at that point. This picture plus the asymmetry that electron and non-electron neutrinos experience through the matter environment (electron (anti)neutrinos can interact through $n + \nu_e \to p + e^-$ and $p + \bar{\nu}_e \to n + e^+$), suggests that the disk achieves complete flavor equipartitioning (decoherence). We can identify two competing causes, namely, quantum decoherence and kinematic decoherence.

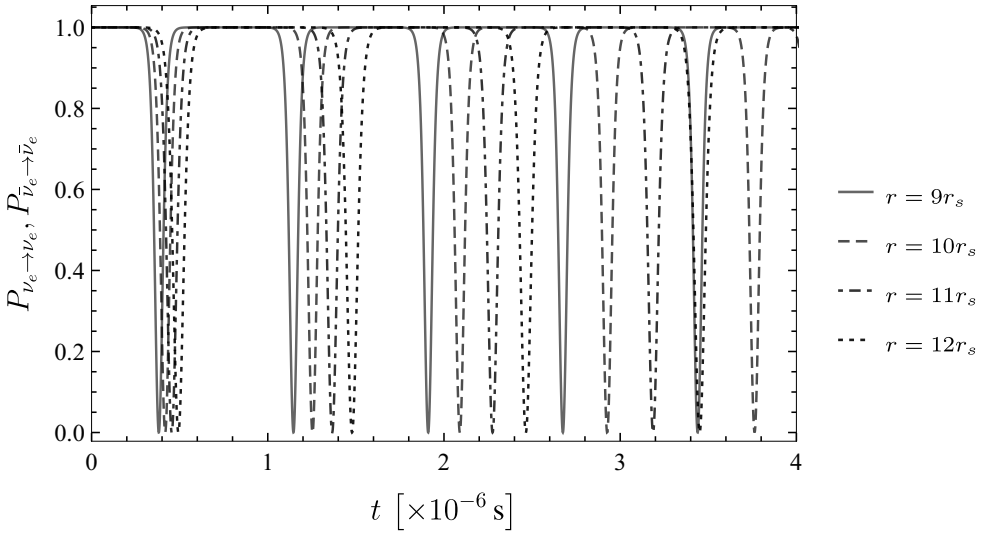

Figure 7. Survival provability for electron neutrinos and antineutrinos for the accretion disk with $\dot{M} = 0.1 M_\odot\ \text{s}^{-1}$ at $r = 9r_s, 10r_s, 11r_s, 12r_s$.

Quantum decoherence is the product of collisions among the neutrinos or with a thermal background medium can be understood as follows [152]. From Appendix D.2 we know that different (anti)neutrino flavors posses different cross-sections and scattering rates $\Gamma_{\nu_i, \bar{\nu}_i}$. In particular, we have $\Gamma_{\nu_x} \approx \Gamma_{\bar{\nu}_x} < \Gamma_{\bar{\nu}_e} < \Gamma_{\nu_e}$. An initial electron (anti)neutrino created at a point r will begin to oscillate into $\nu_x(\bar{\nu}_x)$. The probability of finding it in one of the two flavors evolves as previously discussed. However, in each interaction $n + \nu_e \to p + e^-$, the electron neutrino component of the superposition is absorbed, while the ν_x component remains unaffected. Thus, after the interaction the two flavors can no longer interfere. This allows the remaining ν_x to oscillate and develop a new coherent ν_e component which

is made incoherent in the next interaction. The process will come to equilibrium only when there are equal numbers of electronic and non-electronic neutrinos. That is, the continuous emission and absorption of electronic (anti)neutrinos generate non-electronic (anti)neutrinos with an average probability of $\langle P_{\nu_e \to \nu_e} \rangle$ in each interaction, and once the densities of flavors are equal, the oscillation dynamic stops. An initial system composed of $\nu_e, \bar{\nu}_e$ turns into an equal mixture of $\nu_e, \bar{\nu}_e$ and $\nu_x, \bar{\nu}_x$, reflected as an exponential damping of oscillations. For the particular case in which non-electronic neutrinos can be considered as sterile (do not interact with the medium), the relaxation time of this process can be approximated as [153,154]

$$t_Q = \frac{1}{2l_{\nu\bar{\nu}}\langle\omega\rangle^2 \sin^2 2\theta} + \frac{2l_{\nu\bar{\nu}}\lambda^2}{\langle\omega\rangle^2 \sin^2 2\theta}, \tag{76}$$

where $l_{\nu\bar{\nu}}$ represents the (anti)neutrino mean free path.

Kinematic decoherence is the result of a non-vanishing flux term such that at any point, (anti)neutrinos traveling in different directions do not experience the same self-interaction potential due to the multi-angle term in the integral of Equation (40). Different trajectories do not oscillate in the same way, leading to a de-phasing and a decay of the average $\langle P_{\nu \to \nu} \rangle$, and thus to the equipartitioning of the overall flavor content. The phenomenon is similar to an ensemble of spins in an inhomogeneous magnetic field. In [35] it is shown that for asymmetric $\nu\bar{\nu}$ gas, even an infinitesimal anisotropy triggers an exponential evolution towards equipartitioning, and in [36] it was shown that if the symmetry between neutrinos and antineutrinos is not broken beyond the limit of 25%, kinematic decoherence is still the main effect of neutrino oscillations. As a direct consequence of the $\nu\bar{\nu}$ symmetry present within the ignition radius of accretion disks (see Figure 3), an equipartition among different neutrino flavors is expected. This multi-angle term keeps the order of the characteristic time $t_{\rm osc}$ of Equation (70) unchanged, and kinematic decoherence happens within a few oscillation cycles. The oscillation time gets smaller closer to the BH due to the $1/\mu^{1/2}$ dependence. Therefore, we expect that neutrinos emitted within the ignition radius will be equally distributed among both flavors in about few microseconds. Once the neutrinos reach this maximally mixed state, no further changes are expected. We emphasize that kinematic decoherence does not mean quantum decoherence. Figures 6 and 7 clearly show the typical oscillation pattern which happens only if quantum coherence is still acting on the neutrino system. Kinematic decoherence, differently to quantum decoherence, is just the result of averaging over the neutrino intensities resulting from quick flavor conversion. Therefore, neutrinos are yet able to quantum oscillate if appropriate conditions are satisfied.

Simple inspection of Equations (70) and (76) with Figure 4 yields $t_{\rm osc} \ll t_Q$. Clearly the equipartition time is dominated by kinematic decoherence. These two effects are independent of the neutrino mass hierarchy, and neutrino flavor equipartitioning is achieved for both hierarchies. Within the disk dynamic, this is equivalent to imposing the condition $\langle P_{\nu_e \to \nu_e} \rangle = \langle P_{\bar{\nu}_e \to \bar{\nu}_e} \rangle = 0.5$.

Figure 8 shows a comparison between disks with and without neutrino flavor equipartition for the three accretion rates considered. The roles of an equipartition are to increase the disk's density, reduce the temperature and electron fraction and further stabilize the electron degeneracy for regions inside the ignition radius. The effect is mild for low accretion rates and very pronounced for high accretion rates. This result is in agreement with our understanding of the dynamics of the disk and can be explained in the following way. In low accretion systems the neutrino optical depth for all flavors is $\tau_{\nu\bar{\nu}} \lesssim 1$, and the differences between the cooling fluxes, as given by Equation (32) are small. Hence, when the initial (mainly electron flavor) is redistributed among both flavors, the total neutrino cooling remains virtually unchanged and the disk evolves as if equipartition had never occurred save the new emission flavor content. On the other hand, when accretion rates are high, the optical depth obeys $\tau_{\nu_x} \approx \tau_{\bar{\nu}_x} \lesssim \tau_{\bar{\nu}_e} < \tau_{\nu_e} \sim 10^3$. The ν_e cooling is heavily suppressed—the other factors, less so. When flavors are redistributed, the new ν_x particles are free to escape, enhancing the total cooling and reducing the temperature. As

the temperature decreases, so do the electron and positron densities, leading to a lower electron fraction. The net impact of a flavor equipartition is to make the disk evolution less sensitive to ν_e opacity, and thus, increase the total cooling efficiency. As a consequence, once the fluid reaches a balance between F^+ and F_ν, this state is kept without being affected by high optical depths and η_{e^-} stays at a constant value until the fluid reaches the zero torque condition close to r_{in}. Note that for every case, inside the ignition radius, we find $\tau_{\nu_x} \approx \tau_{\bar{\nu}_x} \lesssim \tau_{\bar{\nu}_e} < \tau_{\nu_e}$ so that the equipartition enhances, mainly, neutrino cooling F_ν (and not antineutrino cooling $F_{\bar{\nu}}$). The quotient between neutrino cooling with and without an equipartition can be estimated with

$$\frac{F_\nu^{\text{eq}}}{F_\nu} \approx \frac{1}{2}\left(1 + \frac{\langle E_{\nu_x}\rangle}{\langle E_{\nu_e}\rangle}\frac{1+\tau_{\nu_e}}{1+\tau_{\nu_x}}\right). \tag{77}$$

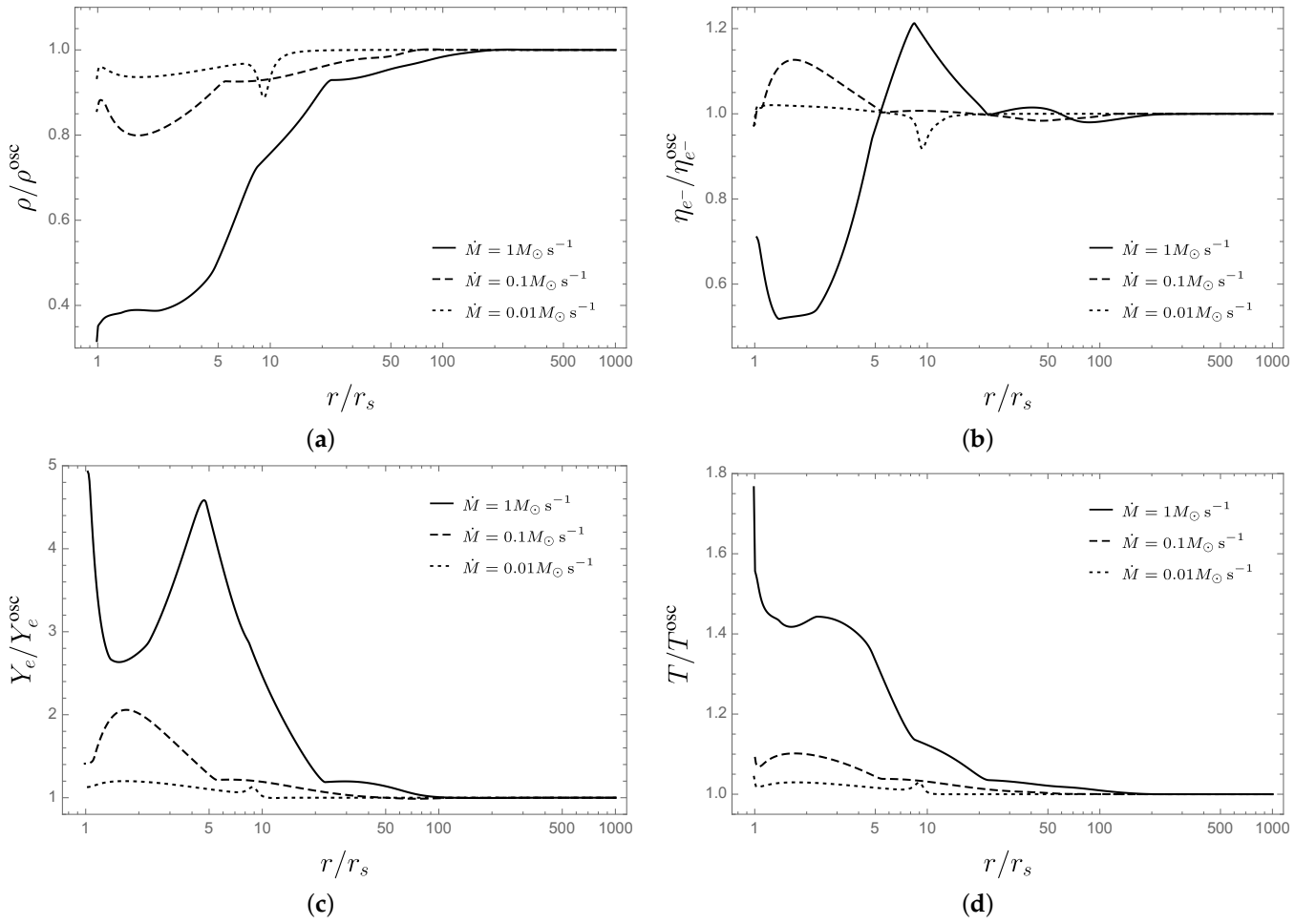

Figure 8. Comparison between the main variables describing thin disks with and without a neutrino flavor equipartition for each accretion rate considered. Here $\rho^{\text{osc}}, \eta_{e^-}^{\text{osc}}, Y_e^{\text{osc}}, T^{\text{osc}}$ are the density, electron degeneracy, electron fraction and temperature of a disk with a flavor equipartition. Together with Figure 3, these plots completely describe the profile of a disk under a flavor equipartition. (**a**) The ratio between baryon densities. (**b**) The ratio between degeneracy parameters. (**c**) The ratio between electron fractions. (**d**) The ratio between temperatures.

This relation exhibits the right limits. From Figure 3 we see that $\langle E_{\nu_e}\rangle \approx \langle E_{\nu_x}\rangle$. Hence, If $1 \gg \tau_{\nu_e} > \tau_{\nu_x}$, then $F_\nu^{\text{eq}} = F_\nu$ and the equipartition is unnoticeable. However, if $1 < \tau_{\nu_x} < \tau_{\nu_e}$ then $F_\nu^{\text{eq}}/F_\nu > 1$. In our simulations, this fraction reaches values of 1.9 for $\dot{M} = 1M_\odot\ \text{s}^{-1}$ to 2.5 for $\dot{M} = 0.01M_\odot\ \text{s}^{-1}$.

The disk variables at each point do not change beyond a factor of order five in the most obvious case. However, these changes can be important for cumulative quantities,

e.g., the total neutrino luminosity and the total energy deposition rate into electron–positron pairs due to neutrino antineutrino annihilation. To see this we perform a Newtonian calculation of these luminosities following [99,100,112,155–158], and references therein. The neutrino luminosity is calculated by integrating the neutrino cooling flux throughout both faces of the disk:

$$L_{\nu_i} = 4\pi \int_{r_{\rm in}}^{r_{\rm out}} C_{\rm cap} F_{\nu_i} r dr. \tag{78}$$

The factor $0 < C_{\rm cap} < 1$ is a function of the radius (called capture function in [126]) that accounts for the proportion of neutrinos that are re-captured by the BH, and thus, do not contribute to the total luminosity. For a BH with $M = 3M_\odot$ and $a = 0.95$, the numerical value of the capture function as a function of the dimensionless distance $x = r/r_s$ is well fitted by

$$C_{\rm cap}(x) = \left(1 + \frac{0.3348}{x^{3/2}}\right)^{-1}, \tag{79}$$

with a relative error smaller than 0.02%. To calculate the energy deposition rate, the disk is modeled as a grid of cells in the equatorial plane. Each cell k has a specific value of differential neutrino luminosity $\Delta\ell^k_{\nu_i} = F^k_{\nu_i} r_k \Delta r_k \Delta\phi_k$ and average neutrino energy $\langle E_{\nu_i}\rangle^k$. If a neutrino of flavor i is emitted from the cell k and an antineutrino is emitted from the cell k', and before interacting at a point $\mathbf{r}$ above the disk, each travels a distance r_k and $r_{k'}$, then their contribution to the energy deposition rate at $\mathbf{r}$ is (see Appendix D.3 for details)

$$\begin{aligned}\Delta Q_{\nu_i\bar\nu_i kk'} = {} & A_{1,i} \frac{\Delta\ell^k_{\nu_i}}{r_k^2} \frac{\Delta\ell^{k'}_{\bar\nu_i}}{r_{k'}^2} \left(\langle E_{\nu_i}\rangle^k + \langle E_{\bar\nu_i}\rangle^{k'}\right) \left(1 - \frac{\mathbf{r}_k \cdot \mathbf{r}_{k'}}{r_k r_{k'}}\right)^2 \\ & + A_{2,i} \frac{\Delta\ell^k_{\nu_i}}{r_k^2} \frac{\Delta\ell^{k'}_{\bar\nu_i}}{r_{k'}^2} \left(\frac{\langle E_{\nu_i}\rangle^k + \langle E_{\bar\nu_i}\rangle^{k'}}{\langle E_{\nu_i}\rangle^k \langle E_{\bar\nu_i}\rangle^{k'}}\right) \left(1 - \frac{\mathbf{r}_k \cdot \mathbf{r}_{k'}}{r_k r_{k'}}\right).\end{aligned} \tag{80}$$

The total neutrino annihilation luminosity is the sum over all pairs of cells integrated in space

$$L_{\nu_i\bar\nu_i} = 4\pi \int_{\mathcal{A}} \sum_{k,k'} \Delta Q_{\nu_i\bar\nu_i kk'} d^3\mathbf{r}, \tag{81}$$

where $\mathcal{A}$ is the entire space above (or below) the disk.

In Table 3 we show the neutrino luminosities and the neutrino annihilation luminosities for disks with and without neutrino collective effects. In each case, the flavor equipartition induces a loss in L_{ν_e} by a factor of ∼3, and a loss in $L_{\bar\nu_e}$ luminosity by a factor of ∼2. At the same time, L_{ν_x} and $L_{\bar\nu_e}$ are increased by a factor ∼10. This translates into a reduction of the energy deposition rate due to electron neutrino annihilation by a factor of ∼7, while the energy deposition rate due to non-electronic neutrinos goes from being negligible to be of the same order of the electronic energy deposition rate. The net effect is to reduce the total energy deposition rate of neutrino annihilation by a factor of ∼3–5 for the accretion rates considered. In particular, we obtain factors of 3.03 and 3.66 for $\dot M = 1\ M_\odot\ {\rm s}^{-1}$ and $\dot M = 0.01\ M_\odot\ {\rm s}^{-1}$, respectively, and a factor of 4.73 for $\dot M = 0.1\ M_\odot\ {\rm s}^{-1}$. The highest value corresponds to an intermediate value of the accretion rate because, for this case, there is a ν_e cooling suppression ($\tau_{\nu_e} > 1$) and the quotient $\tau_{\nu_e}/\tau_{\nu_x}$ is maximal. By Equation (77), the difference between the respective cooling terms is also maximal. In Figure 9 we show the energy deposition rate per unit volume around the BH for each flavor with accretion rates $\dot M = 1\ M_\odot\ {\rm s}^{-1}$ and $\dot M = 0.1\ M_\odot\ {\rm s}^{-1}$. There we can see the drastic enhancement of the non-electronic neutrino energy deposition rate and the reduction of the electronic deposition rate. Due to the double peak in the neutrino density for $\dot M = 0.01\ M_\odot\ {\rm s}^{-1}$ case (see Figure 3), the deposition rate per unit volume also shows two peaks—one at $r_s < r < 2r_s$ and the other at $10\,r_s < r < 11\,r_s$. Even so, the behavior is similar to the other cases.

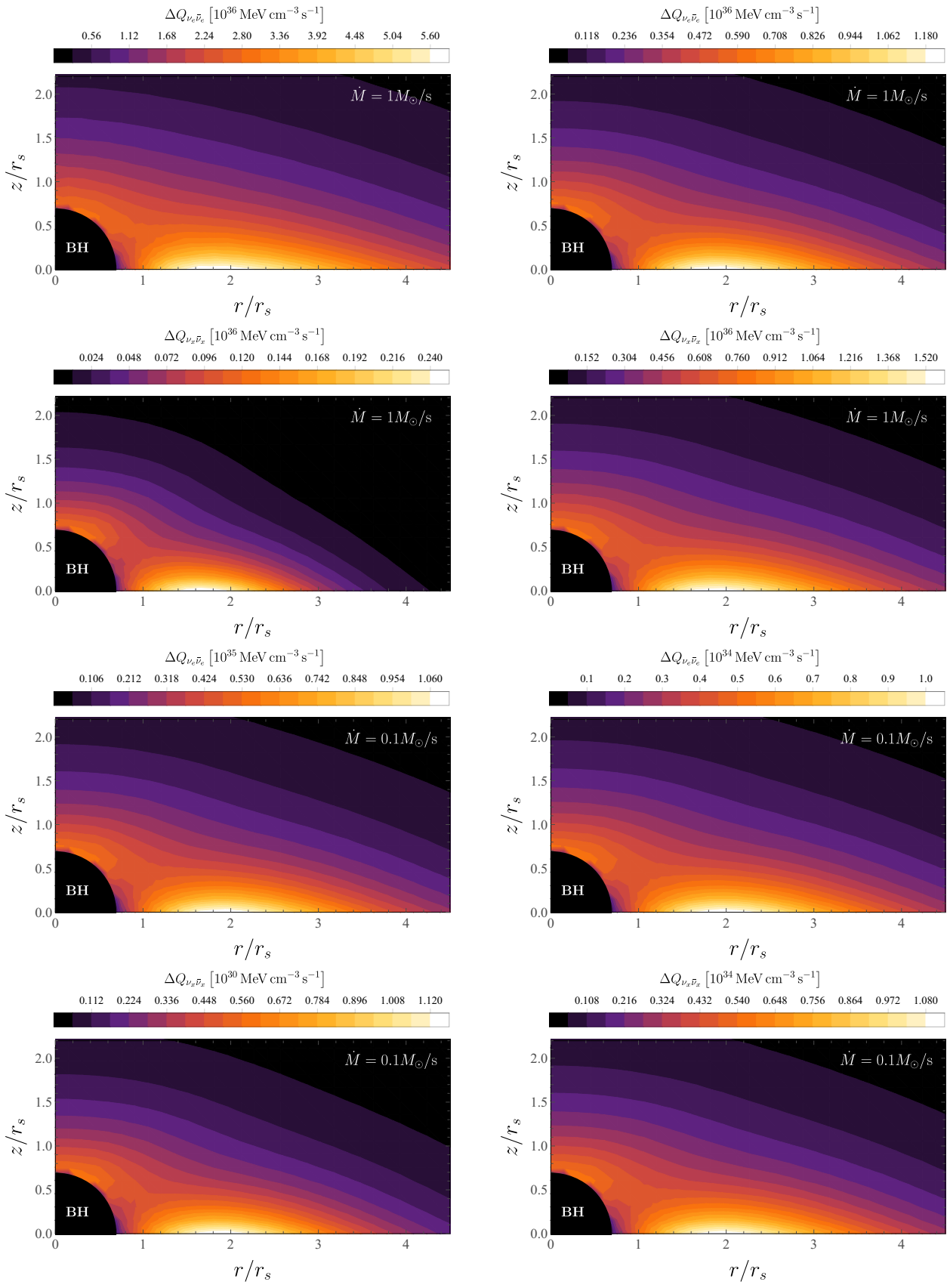

Figure 9. Comparison of the neutrino annihilation luminosity per unit volume $\Delta Q_{\nu_i\bar{\nu}_i} = \sum_{k,k'} \Delta Q_{\nu_i\bar{\nu}_i kk'}$ between disk without (**left** column) and with (**right** column) flavor equipartitioning for accretion rates $\dot{M} = 1M_\odot\ \mathrm{s}^{-1}$ and $\dot{M} = 0.01M_\odot\ \mathrm{s}^{-1}$.

Table 3. Comparison of total neutrino luminosities L_ν and annihilation luminosities $L_{\nu\bar{\nu}}$ between disks with and without flavor equipartitions. All luminosities are reported in MeV s^{-1}.

	Without Oscillations						With Oscillations (Flavor Equipartition)					
	L_{ν_e}	$L_{\bar{\nu}_e}$	L_{ν_x}	$L_{\bar{\nu}_x}$	$L_{\nu_e\bar{\nu}_e}$	$L_{\nu_x\bar{\nu}_x}$	L_{ν_e}	$L_{\bar{\nu}_e}$	L_{ν_x}	$L_{\bar{\nu}_x}$	$L_{\nu_e\bar{\nu}_e}$	$L_{\nu_x\bar{\nu}_x}$
1 $M_\odot$ s^{-1}	6.46×10^{58}	7.33×10^{58}	1.17×10^{58}	1.17×10^{58}	1.25×10^{57}	1.05×10^{55}	1.87×10^{58}	4.37×10^{58}	7.55×10^{58}	5.44×10^{58}	1.85×10^{56}	2.31×10^{56}
0.1 $M_\odot$ s^{-1}	9.19×10^{57}	1.08×10^{58}	8.06×10^{55}	8.06×10^{55}	1.62×10^{55}	1.27×10^{50}	2.47×10^{57}	4.89×10^{57}	7.75×10^{57}	5.27×10^{57}	1.78×10^{54}	1.64×10^{54}
0.01 $M_\odot$ s^{-1}	1.05×10^{57}	1.12×10^{57}	2.43×10^{55}	2.43×10^{55}	1.78×10^{53}	8.68×10^{48}	4.29×10^{56}	5.48×10^{56}	6.71×10^{56}	5.70×10^{56}	3.53×10^{52}	1.23×10^{52}

6. Discussion

The generation of a seed, energetic e^-e^+ plasma, seems to be a general prerequisite of GRB theoretical models for the explanation of the prompt (MeV) gamma-ray emission. The e^-e^+ pair annihilation produces photons leading to an opaque pair-photon plasma that self-accelerates, expanding to ultrarelativistic Lorentz factors in the order of 10^2–10^3 (see, e.g., [159–161]). The reaching of transparency of MeV-photons at large Lorentz factor and corresponding large radii is requested to solve the so-called compactness problem posed by the observed non-thermal spectrum in the prompt emission [162–164]. There is a vast literature on this subject, and we refer the reader to [165–170] and references therein for further details.

Neutrino-cooled accretion disks onto rotating BHs have been proposed as a possible way of producing the above-mentioned e^-e^+ plasma. The reason is that such disks emit a large amount of neutrino and antineutrinos that can undergo pair annihilation near the BH [100–112]. The viability of this scenario clearly depends on the energy deposition rate of neutrino-antineutrinos into e^-e^+ and so on the local (anti)neutrino density and energy.

We have here shown that, inside these hyperaccreting disks, a rich neutrino oscillation phenomenology is present due to the high neutrino density. Consequently, the neutrino/antineutrino emission and the corresponding pair annihilation process around the BH leading to electron–positron pairs, are affected by neutrino flavor conversion. Using the thin disk and α-viscosity approximations, we have built a simple stationary model of general relativistic neutrino-cooled accretion disks around a Kerr BH that takes into account not only a wide range of neutrino emission processes and nucleosynthesis, but also the dynamics of flavor oscillations. The main assumption relies on considering the neutrino oscillation behavior within small neighboring regions of the disk as independent from each other. This, albeit being a first approximation to a more detailed picture, has allowed us to set the main framework to analyze the neutrino oscillations phenomenology in inside neutrino-cooled disks.

In the absence of oscillations, a variety of neutrino-cooled accretion disks onto Kerr BHs, without neutrino flavor oscillations, have been modeled in the literature (see, e.g., [99,100,107,112,124] for a recent review). The physical setting of our disk model follows closely the ones considered in [107], but with some extensions and differences in some aspects:

1. The equation of vertical hydrostatic equilibrium, Equation (15), can be derived in several ways [124,127,131]. We followed a particular approach consistent with the assumptions in [127], in which we took the vertical average of a hydrostatic Euler equation in polar coordinates. The result is an equation that leads to smaller values of the disk pressure when compared with other models. It is expected that the pressure at the center of the disk is smaller than the average density multiplied by the local tidal acceleration at the equatorial plane. Still, the choice between the assortment of pressure relations is tantamount to the fine-tuning of the model. Within the thin disk approximation, all these approaches are equivalent, since they all assume vertical equilibrium and neglect self-gravity.
2. Following the BdHN scenario for the explanation of GRBs associated with Type Ic SNe (see Section 2), we considered a gas composed of ^{16}O at the outermost radius of the disk and followed the evolution of the ion content using the Saha equation to fix the local NSE. In [107], only ^{4}He is present, and in [112], ions up to ^{56}Fe are introduced.

The affinity between these cases implies that this particular model of disk accretion is insensible to the initial mass fraction distribution. This is explained by the fact that the average binding energy for most ions is very similar; hence, any cooling or heating due to a redistribution of nucleons, given by the NSE, is negligible when compared to the energy consumed by direct photodisintegration of alpha particles. Additionally, once most ions are dissociated, the main cooling mechanism is neutrino emission, which is similar for all models; the modulo includes the supplementary neutrino emission processes included in addition to electron and positron capture. However, during our numerical calculations, we noticed that the inclusion of non-electron neutrino emission processes can reduce the electron fraction by up to ∼8%. This effect was observed again during the simulation of flavor equipartition alluding to the need for detailed calculations of neutrino emissivities when establishing NSE state. We obtained similar results to [107] (see Figure 3), but by varying the accretion rate and fixing the viscosity parameter. This suggests that a more natural differentiating set of variables in the hydrodynamic equations of an α-viscosity disk is the combination of the quotient $\dot{M}/\alpha$ and either $\dot{M}$ or α. This result is already evident in, for example, Figures 11 and 12 of [107], but was not mentioned there.

Concerning neutrino oscillations, we showed that for the conditions inside the ignition radius, the oscillation potentials follow the relation $\langle\omega\rangle \ll \mu \ll \lambda$, as is illustrated by Figure 5. We also showed that within this region the number densities of electron neutrinos and antineutrinos are very similar. As a consequence of this particular environment, very fast pair conversions $\nu_e\bar{\nu}_e \rightleftharpoons \nu_x\bar{\nu}_x$, induced by bipolar oscillations, are obtained for the inverted mass hierarchy case with oscillation frequencies between 10^9 s^{-1} and 10^5 s^{-1}. For the normal hierarchy case, no flavor changes were observed (see Figures 6 and 7). Bearing in mind the magnitudes of these frequencies and the low neutrino travel times through the disk, we conclude that an accretion disk under our main assumption cannot represent a steady-state. However, using numerical and algebraic results obtained in [33,35,36] and references therein, we were able to generalize our model to a more realistic picture of neutrino oscillations. The main consequence of the interactions between neighboring regions of the disk is the onset of kinematic decoherence in a timescale in the order of the oscillation times. Kinematic decoherence induces a fast flavor equipartition among electronic and non-electronic neutrinos throughout the disk. Therefore, the neutrino content emerging from the disk is very different from the one that is usually assumed (see, e.g., [113,117,171]). The comparison between disks with and without flavor equipartition is summarized in Figure 8 and Table 3. We found that the flavor equipartition, while leaving antineutrino cooling practically unchanged, it enhances neutrino cooling by allowing the energy contained (and partially trapped inside the disk due to high opacity) within the ν_e gas to escape in the form of ν_x, rendering the disk insensible to the electron neutrino opacity. We give in Equation (77) a relation to estimate the change in F_ν as a function of $\tau_{\nu_e}\tau_{\nu_x}$ that describes correctly the behavior of the disk under the flavor equipartition. The variation of the flavor content in the emission flux implies a loss in L_{ν_e} and an increase in L_{ν_x} and $L_{\bar{\nu}_e}$. As a consequence, the total energy deposition rate of the process $\nu + \bar{\nu} \to e^- + e^+$ is reduced. We showed that this reduction can be as high 80% and is maximal whenever the quotient $\tau_{\nu_e}/\tau_{\nu_x}$ is also maximal and the condition $\tau_{\nu_e} > 1$ is obtained.

At this point, we can identify several issues which must still to be investigated in view of the results we have presented:

First, throughout the accretion disk literature, several fits of the neutrino and neutrino annihilation luminosity can be found (see, e.g., [99] and references therein). However, all these fits were calculated without taking into account neutrino oscillations. Since we have shown that oscillations directly impact luminosity, these results need to be extended.

Second, the calculations of the neutrino and antineutrino annihilation luminosities we have performed ignore general relativistic effects, save for the correction given by the capture function, and the possible neutrino oscillations from the disk surface to the

annihilation point. In [172], it has been shown that general relativistic effects can enhance the neutrino annihilation luminosity in a neutron star binary merger by a factor of 10. In [100], however, it is argued that in BHs this effect has to be mild since the energy gained by falling into the gravitational potential is lost by the electron–positron pairs when they climb back up. Nonetheless, this argument ignores the bending of neutrino trajectories and neutrino capture by the BH which can be significant for $r \lesssim 10r_s$. In [173], the increment is calculated to be no more than a factor of 2 and can be less depending on the geometry of the emitting surface. However, as before, these calculations assume a purely $\nu_e\bar{\nu}_e$ emission and ignore oscillations after the emission. Simultaneously, the literature on neutrino oscillation above accretion disks (see, e.g., [113,117]) does not take int account oscillations inside the disk and assume only $\nu_e\bar{\nu}_e$ emission. A similar situation occurs in works studying the effect of neutrino emission on r-process nucleosynthesis in hot outflows (wind) ejected from the disk (see, e.g., [174]).

It is still unclear how the complete picture (oscillations inside the disk $\rightarrow$ oscillations above the disk + relativistic effects) affects the final energy deposition. We are currently working on the numerical calculation of the annihilation energy deposition rate using a ray tracing code and including neutrino oscillations from the point of their creation until they are annihilated—i.e., within the accretion disk and after its emission from the surface of the disk and during its trajectory until reaching the annihilation point. These results and their consequences for the energy deposition annihilation rate will be the subject of a future publication.

The knowledge of the final behavior of a neutrino-dominated accretion disk with neutrino oscillations requires time-dependent, multi-dimensional, neutrino-transport simulations coupled with the evolution of the disk. These simulations are computationally costly even for systems with a high degree of symmetry, therefore a first approximation is needed to identify key theoretical and numerical features involved in the study of neutrino oscillations in neutrino-cooled accretion disks. This work serves as a platform for such a first approximation. Considering that kinematic decoherence is a general feature of anisotropic neutrino gases, with the simplified model presented here, we were able to obtain an analytical result that agrees with the physics understanding of accretion disks.

In [171] it is pointed out that for a total energy in $\bar{\nu}_e$ of 10^{52} erg and an average neutrino energy $\langle E_{\nu,\bar{\nu}} \rangle \sim 20$ MeV, the Hyper-Kamiokande neutrino-horizon is in the order of 1 Mpc. If we take a total energy carried out by $\bar{\nu}_e$ in the order of the gravitational gain by accretion ($E_g \sim 10^{52}$–10^{53} erg) in the more energetic case of binary-driven hypernovae and the neutrino energies in Figure 3, we should expect the neutrino-horizon distance to be also in the order of 1 Mpc. However, if we adopt the local binary-driven hypernovae rate $\sim$1 Gpc^{-3} yr^{-1} [175], it is clear that the direct detection of this neutrino signal is quite unlikely. However, we have shown that neutrino oscillation can have an effect on e^-e^+ plasma production above BHs in GRB models. Additionally, the unique conditions inside the disk and its geometry lend themselves to a variety of neutrino oscillations that can have impacts on other astrophysical phenomena, not only in plasma production, but also in r-process nucleosynthesis in disk winds. This, in particular, is the subject of a future publication. As such, this topic deserves appropriate attention, since it paves the way for new, additional astrophysical scenarios for testing neutrino physics.

Author Contributions: Conceptualization, J.D.U., E.A.B.-V. and J.A.R.; methodology, J.D.U., E.A.B.-V. and J.A.R.; software, J.D.U., E.A.B.-V. and J.A.R.; validation, J.D.U., E.A.B.-V. and J.A.R.; formal analysis, J.D.U., E.A.B.-V. and J.A.R.; investigation, J.D.U., E.A.B.-V. and J.A.R.; resources, J.D.U., E.A.B.-V. and J.A.R.; data curation, J.D.U., E.A.B.-V. and J.A.R.; writing—original draft preparation, J.D.U., E.A.B.-V. and J.A.R.; writing—review and editing, J.D.U., E.A.B.-V. and J.A.R.; visualization, J.D.U., E.A.B.-V. and J.A.R.; supervision, J.D.U., E.A.B.-V. and J.A.R.; project administration, J.D.U., E.A.B.-V. and J.A.R.; funding acquisition, J.D.U., E.A.B.-V. and J.A.R. All authors have read and agreed to the published version of the manuscript.

Funding: J.D.U. was supported by COLCIENCIAS under the program Becas Doctorados en el Exterior Convocatoria No. 728. E.A.B-V. was supported from COLCIENCIAS under the program

Becas Doctorados Nacionales Convocatoria, number 727, the International Center for Relativistic Astrophysics Network (ICRANet), Universidad Industrial de Santander (UIS) and the International Relativistic Astrophysics Ph.D Program (IRAP-PhD).

Acknowledgments: The authors thank C. L. Fryer for insightful discussions on astrophysical consequences of neutrino flavor oscillations in accretion disks.

Conflicts of Interest: The authors declare no conflict of interest.

Abbreviations

The following abbreviations are used in this manuscript:

BdHN	Binary-Driven Hypernova
BH	Black Hole
CF	Coordinate Frame
CO_{core}	Carbon–Oxygen Star
CRF	Co-rotating Frame
GRB	Gamma-ray Burst
IGC	Induced Gravitational Collapse
ISCO	Innermost Stable Circular Orbit
LNRF	Locally Non-Rotating Frame
MSW	Mikheyev–Smirnov–Wolfenstein
NDAF	Neutrino-Dominated Accretion Flows
NS	Neutron Star
NSE	Nuclear Statistical Equilibrium
SN	Supernova

Appendix A. Transformations and Christoffel Symbols

For the sake of completeness, here we give the explicitly the transformation used in Equation (5) and the Christoffel symbols used during calculations. The coordinate transformation matrices between the CF and the LNRF on the tangent vector space is [123]

$$e_{\hat{\nu}}{}^{\mu} = \begin{pmatrix} \frac{1}{\sqrt{\omega^2 g_{\phi\phi} - g_{tt}}} & 0 & 0 & 0 \\ 0 & \frac{1}{\sqrt{g_{rr}}} & 0 & 0 \\ 0 & 0 & \frac{1}{\sqrt{g_{\theta\theta}}} & 0 \\ \frac{\omega}{\sqrt{\omega^2 g_{\phi\phi} - g_{tt}}} & 0 & 0 & \frac{1}{\sqrt{g_{\phi\phi}}} \end{pmatrix}, \quad e^{\hat{\nu}}{}_{\mu} = \begin{pmatrix} \sqrt{\omega^2 g_{\phi\phi} - g_{tt}} & 0 & 0 & 0 \\ 0 & \sqrt{g_{rr}} & 0 & 0 \\ 0 & 0 & \sqrt{g_{\theta\theta}} & 0 \\ -\omega\sqrt{g_{\phi\phi}} & 0 & 0 & \sqrt{g_{\phi\phi}} \end{pmatrix}, \tag{A1}$$

so that the basis vectors transform as $\partial_{\hat{\nu}} = e^{\mu}{}_{\tilde{\nu}} \partial_{\mu}$, that is, with $\boldsymbol{e}^T$. For clarity, coordinates on the LNRF have a caret $(x^{\hat{\mu}})$, coordinates on the CRF have a tilde $(x^{\tilde{\mu}})$ and coordinates on the LRF have two $(x^{\tilde{\tilde{\mu}}})$. An observer on the LNRF sees the fluid elements move with an azimuthal velocity $\beta^{\hat{\phi}}$. This observer then can perform a Lorentz boost $L_{\beta^{\hat{\phi}}}$ to a new frame. On this new frame an observer sees the fluid elements falling radially with velocity $\beta^{\tilde{r}}$, so it can perform another Lorentz boost $L_{\beta^{\tilde{r}}}$ to the LRF. Finally, the transformation between the the LRF and the CF coordinates $x^{\mu} = e_{\hat{\rho}}{}^{\mu} (L_{\beta^{\hat{\phi}}})_{\tilde{\alpha}}{}^{\hat{\rho}} (L_{\beta^{\tilde{r}}})_{\tilde{\tilde{\nu}}}{}^{\tilde{\alpha}} x^{\tilde{\tilde{\nu}}} = A_{\tilde{\tilde{\nu}}}{}^{\mu} x^{\tilde{\tilde{\nu}}}$, where the components of $\boldsymbol{A}$ are

$$A^{\tilde{\tilde{\nu}}}{}_{\mu} = \begin{pmatrix} \gamma_{\tilde{r}}\gamma_{\hat{\phi}} \left(\sqrt{\omega^2 g_{\phi\phi} - g_{tt}} + \beta^{\hat{\phi}} \omega \sqrt{g_{\phi\phi}} \right) & -\gamma_{\tilde{r}} \beta^{\tilde{r}} \sqrt{g_{rr}} & 0 & -\gamma_{\tilde{r}}\gamma_{\hat{\phi}} \beta^{\hat{\phi}} \sqrt{g_{\phi\phi}} \\ -\gamma_{\hat{\phi}}\gamma_{\tilde{r}}\beta^{\tilde{r}} \left(\sqrt{\omega^2 g_{\phi\phi} - g_{tt}} + \beta^{\hat{\phi}} \omega \sqrt{g_{\phi\phi}} \right) & \gamma_{\tilde{r}} \sqrt{g_{rr}} & 0 & \gamma_{\tilde{r}}\gamma_{\hat{\phi}} \beta^{\tilde{r}} \beta^{\hat{\phi}} \sqrt{g_{\phi\phi}} \\ 0 & 0 & \sqrt{g_{\theta\theta}} & 0 \\ -\gamma_{\hat{\phi}} \left(\beta^{\hat{\phi}} \sqrt{\omega^2 g_{\phi\phi} - g_{tt}} + \omega \sqrt{g_{\phi\phi}} \right) & 0 & 0 & \gamma_{\hat{\phi}} \sqrt{g_{\phi\phi}} \end{pmatrix}. \tag{A2}$$

Since Lorentz transformations do not commute, the transformation $\boldsymbol{A}$ raises the question: what happens if we invert the order? In this case, we would not consider a co-rotating frame but a cofalling frame on which observers see fluid elements, not falling, but rotating. The new transformation velocities $\beta^{r'}$, $\beta^{\phi'}$ are subject to the conditions $\beta^{\phi'} = \gamma_{r'} \beta^{\hat{\phi}}$,

$\beta^{r'} = \beta^{\tilde{r}}/\gamma_{\hat{\phi}}$ and $\gamma_{r'}\gamma_{\phi'} = \gamma_{\tilde{r}}\gamma_{\hat{\phi}}$. Although both approaches are valid, considering that the radial velocity is an unknown, the first approach is clearly cleaner. To obtain the coordinate transformation between the CF and the CRF $A_{\tilde{\nu}}{}^{\mu}$ and $A^{\tilde{\nu}}{}_{\mu}$ we can simply set $\beta^{\tilde{r}} = 0$ in Equation (A2). With this, we can calculate

$$\frac{d\hat{\phi}}{d\hat{t}} = \beta^{\hat{\phi}} = \frac{u^{\mu}e^{\hat{\phi}}{}_{\mu}}{u^{\nu}e^{\hat{t}}{}_{\nu}} = \sqrt{\frac{g_{\phi\phi}}{\omega^2 g_{\phi\phi} - g_{tt}}}(\Omega - \omega), \tag{A3}$$

and

$$d\tilde{r} = \sqrt{g_{rr}}dr, \;\; d\tilde{t} = \frac{\gamma_{\hat{\phi}}}{\sqrt{\omega^2 g_{\phi\phi} - g_{tt}}}dt = \frac{1}{\sqrt{-g_{tt} - 2\Omega g_{t\phi} - \Omega^2 g_{\phi\phi}}}dt, \;\; d\tilde{\theta} = \sqrt{g_{\theta\theta}}d\theta. \tag{A4}$$

The non-vanishing Christoffel symbols are

$$\begin{aligned}
&\Gamma^{t}_{tr} = \frac{M\left(r^2 - M^2a^2\cos^2\theta\right)\left(r^2 + M^2a^2\right)}{\Sigma^2\Delta}, \;\; \Gamma^{t}_{t\theta} = -\frac{M^3a^2 r\sin 2\theta}{\Sigma^2}, \\
&\Gamma^{t}_{r\phi} = -\frac{M^2a\left(3r^4 + M^2a^2r^2 + M^2a^2\cos^2\theta\left(r^2 - M^2a^2\right)\right)\sin^2\theta}{\Sigma^2\Delta}, \\
&\Gamma^{t}_{\theta\phi} = \frac{2M^4a^3 r\cos\theta\sin^3\theta}{\Sigma^2}, \;\; \Gamma^{r}_{tt} = \frac{M\Delta\left(r^2 - M^2a^2\cos^2\theta\right)}{\Sigma^3}, \\
&\Gamma^{r}_{t\phi} = -\frac{M^2a\Delta\left(r^2 - M^2a^2\cos^2\theta\right)\sin^2\theta}{\Sigma^3}, \\
&\Gamma^{r}_{rr} = \frac{r}{\Sigma} + \frac{M - r}{\Delta}, \;\; \Gamma^{r}_{r\theta} = -\frac{M^2a^2\sin\theta}{M^2a^2\cos\theta + r^2\tan\theta}, \;\; \Gamma^{r}_{\theta\theta} = -\frac{r\Delta}{\Sigma}, \\
&\Gamma^{r}_{\phi\phi} = \left(Ma\Gamma^{r}_{t\phi} - \Gamma^{r}_{\theta\theta}\right)\sin^2\theta, \;\; \Gamma^{\theta}_{tt} = -\Gamma^{t}_{\theta\phi}\frac{\csc^2\theta}{Ma\Sigma}, \;\; \Gamma^{\theta}_{t\phi} = \frac{M^2ar\left(r^2 + M^2a^2\right)\sin 2\theta}{\Sigma^3}, \\
&\Gamma^{\theta}_{rr} = \frac{M^2a^2\sin\theta\cos\theta}{\Sigma\Delta}, \;\; \Gamma^{\theta}_{t\theta} = \frac{r}{\Sigma}, \;\; \Gamma^{\theta}_{\theta\theta} = \Gamma^{r}_{r\theta}, \\
&\Gamma^{\theta}_{\phi\phi} = \left(\frac{\Delta}{\Sigma} + \frac{2Mr\left(r^2 + M^2a^2\right)^2}{\Sigma^3}\right)\sin\theta\cos\theta, \;\; \Gamma^{\phi}_{tr} = -\frac{M^2a\left(r^2 - M^2a^2\cos^2\theta\right)}{\Sigma^2\Delta}, \\
&\Gamma^{\phi}_{t\theta} = -\frac{2M^2ar\cot\theta}{\Sigma^2}, \;\; \Gamma^{\phi}_{r\phi} = \frac{r(\Sigma - 2Mr)}{\Sigma\Delta} + \frac{Ma\Sigma}{\Delta^2}\Gamma^{r}_{t\phi}, \;\; \Gamma^{\phi}_{\theta\phi} = \cot\theta - \Gamma^{t}_{t\theta}.
\end{aligned} \tag{A5}$$

Using the connection coefficients and the metric, both evaluated at the equatorial plane we can collect several equations for averaged quantities. The expansion of the fluid world lines is

$$\boldsymbol{\theta} = \nabla_{\mu}u^{\mu} = \frac{2}{r}u^{r} + \partial_r u^{r}. \tag{A6}$$

There are several ways to obtain an approximate version of the shear tensor (e.g., [124,176,177]) but by far the simplest one is proposed by [127]. On the CRF the fluid four-velocity can be approximated by $u^{\tilde{\mu}} = (1,0,0,0)$ by Equation (6). Both the fluid four-acceleration $a_{\nu} = u^{\mu}\nabla_{\mu}u_{\nu}$ and expansion parameter, Equation (A6), vanish so that the shear tensor reduces to $2\sigma_{\tilde{\mu}\tilde{\nu}} = \nabla_{\tilde{\mu}}u_{\tilde{\nu}} + \nabla_{\tilde{\nu}}u_{\tilde{\mu}}$. In particular, the r-ϕ component is

$$\sigma_{\tilde{r}\tilde{\phi}} = -\frac{1}{2}\left(\Gamma^{\tilde{t}}_{\tilde{\phi}\tilde{r}} + \Gamma^{\tilde{t}}_{\tilde{r}\tilde{\phi}}\right) = -\frac{1}{4}\left(2c_{\tilde{t}\tilde{\phi}}{}^{\tilde{r}} + 2c_{\tilde{t}\tilde{r}}{}^{\tilde{\phi}}\right) = \frac{1}{2}c_{\tilde{r}\tilde{t}}{}^{\tilde{\phi}} = \frac{\gamma^2_{\tilde{\phi}}}{2}\frac{\sqrt{g_{\phi\phi}}}{\sqrt{\omega^2 g_{\phi\phi} - g_{tt}}\sqrt{g_{rr}}}\partial_r\Omega, \tag{A7}$$

where $c_{\tilde{\mu}\tilde{\nu}}{}^{\tilde{\alpha}}$ are the commutation coefficients for the CRF. Finally, of particular interest is the $\tilde{\theta}$ component of the Riemann curvature tensor

$$R^{\tilde{\theta}}{}_{\tilde{t}\tilde{\theta}\tilde{t}}\Big|_{\theta=\pi/2} = \frac{M}{r^3}\frac{r^2 - 4aM^{3/2}r^{1/2} + 3M^2a^2}{r^2 - 3Mr + 2aM^{3/2}r^{1/2}}, \tag{A8}$$

which gives a measurement of the relative acceleration in the $\tilde{\theta}$ direction of nearly equatorial geodesics.

Appendix B. Stress–Energy Tensor

Here we present some equations related to the stress–energy that we used in this paper. Equation (9) for a zero bulk viscosity fluid in components is

$$T^{\mu}_{\nu} = \Pi u^{\mu} u_{\nu} + P\delta^{\mu}_{\nu} - 2\eta\sigma^{\mu}_{\nu} + q^{\mu}u_{\nu} + q_{\nu}u^{\mu}, \tag{A9}$$

whose (vanishing) covariant derivative is

$$\begin{aligned}\nabla_{\mu}T^{\mu}_{\nu} &= u^{\mu}u_{\nu}\partial_{\mu}\Pi + \Pi\boldsymbol{\theta}u_{\nu} + \Pi a_{\nu} + \partial_{\nu}P - 2\eta\nabla_{\mu}\sigma^{\mu}_{\nu} + q^{\mu}\nabla_{\mu}u_{\nu} + u_{\nu}\nabla_{\mu}q^{\mu} + q_{\nu}\boldsymbol{\theta} + u^{\mu}\nabla_{\mu}q_{\nu} \\ &= u^{\mu}\left[u_{\nu}\left(\partial_{\mu}\Pi - \frac{\Pi}{\rho}\partial_{\mu}\rho\right) - \frac{q_{\nu}}{\rho}\partial_{\mu}\rho\right] + \Pi a_{\nu} + \partial_{\nu}P - 2\eta\nabla_{\mu}\sigma^{\mu}_{\nu} + q^{\mu}\nabla_{\mu}u_{\nu} + u_{\nu}\nabla_{\mu}q^{\mu} + u^{\mu}\nabla_{\mu}q_{\nu},\end{aligned} \tag{A10}$$

where baryon conservation is used $\rho\boldsymbol{\theta} = -u^{\mu}\partial_{\mu}\rho$. To get an equation of motion for the fluid, we project along the direction perpendicular to u_{ν}

$$\begin{aligned}&P^{\nu}_{\beta}\nabla_{\mu}T^{\mu}_{\nu} = u^{\mu}\left[u_{\beta}\left(\partial_{\mu}\Pi - \frac{\Pi}{\rho}\partial_{\mu}\rho\right) - \frac{q_{\beta}}{\rho}\partial_{\mu}\rho\right] + \Pi a_{\beta} + \partial_{\beta}P - 2\eta\nabla_{\mu}\sigma^{\mu}_{\beta} + q^{\mu}\nabla_{\mu}u_{\beta} + u_{\beta}\nabla_{\mu}q^{\mu} \\ &+ u^{\mu}\nabla_{\mu}q_{\beta} - u^{\mu}u_{\beta}\left[\partial_{\mu}\Pi - \frac{\Pi}{\rho}\partial_{\mu}\rho\right] + u^{\nu}u_{\beta}\partial_{\nu}P - 2\eta u^{\nu}u_{\beta}\nabla_{\mu}\sigma^{\mu}_{\nu} - u_{\beta}\nabla_{\mu}q^{\mu} + u^{\nu}u_{\beta}u^{\mu}\nabla_{\mu}q_{\nu} \\ &= -\frac{q_{\beta}}{\rho}u^{\mu}\partial_{\mu}\rho + \Pi a_{\beta} + \partial_{\beta}P - 2\eta\nabla_{\mu}\sigma^{\mu}_{\beta} + q^{\mu}\nabla_{\mu}u_{\beta} + u^{\mu}\nabla_{\mu}q_{\beta} + u_{\beta}u^{\nu}\partial_{\nu}P - 2\eta u^{\nu}u_{\beta}\nabla_{\mu}\sigma^{\mu}_{\nu} + u^{\nu}u_{\beta}u^{\mu}\nabla_{\mu}q_{\nu} \\ &= -\frac{q_{\beta}}{\rho}u^{\mu}\partial_{\mu}\rho + \Pi a_{\beta} + \partial_{\beta}P - 2\eta\nabla_{\mu}\sigma^{\mu}_{\beta} + q^{\mu}\nabla_{\mu}u_{\beta} + u^{\mu}\nabla_{\mu}q_{\beta} + u_{\beta}\left(u^{\nu}\partial_{\nu}P + 2\eta\sigma^{\mu\nu}\sigma_{\mu\nu} - q_{\nu}a^{\nu}\right),\end{aligned} \tag{A11}$$

where the identities $q_{\mu}u^{\mu} = u^{\mu}a_{\mu} = \sigma^{\mu\nu}u_{\nu} = 0$, $u_{\mu}u^{\nu} = -1$, $\sigma^{\mu\nu}\sigma_{\mu\nu} = \sigma^{\mu\nu}\nabla_{\mu}u_{\nu}$ are used. Combining the Equations (A10) and (A11) we get

$$u^{\mu}\left[\partial_{\mu}U - \frac{U+P}{\rho}\partial_{\mu}\rho\right] = 2\eta\sigma^{\mu\nu}\sigma_{\mu\nu} - q_{\mu}a^{\mu} - \nabla_{\mu}q^{\mu}. \tag{A12}$$

With Equation (A6) we can obtain an equation for mass conservation

$$\begin{aligned}0 =& \nabla_{\mu}(\rho u^{\mu}) = u^{\mu}\partial_{\mu}\rho + \rho\boldsymbol{\theta} = u^{\mu}\partial_{\mu}\rho + \rho\left(\frac{2}{r}u^{r} + \partial_{r}u^{r}\right), \\ &\Rightarrow \partial_{r}\left(r^{2}\rho u^{r}\right) + r^{2}u^{j}\partial_{j}\rho = 0, \quad \text{for } j \in \{t,\theta,\phi\}.\end{aligned} \tag{A13}$$

Finally, we reproduce the zero torque at the innermost stable circular orbit condition that appears in [128]. Using the killing vector fields $\boldsymbol{\partial}_{\phi}$, $\boldsymbol{\partial}_{t}$ and the approximation $\Pi \approx \rho$, we can calculate

$$\begin{aligned}&0 = \boldsymbol{\nabla}\cdot(\boldsymbol{T}\cdot\boldsymbol{\partial}_{\phi}) = \nabla_{\mu}T^{\mu}_{\phi} = \frac{1}{\sqrt{-g}}\partial_{\mu}\left(\sqrt{-g}T^{\mu}_{\phi}\right) \approx \frac{1}{r^{2}}\partial_{r}\left(\rho u^{r}u_{\phi}r^{2} - 2\eta\sigma^{r}_{\phi}r^{2}\right) + u_{\phi}\partial_{\theta}q^{\theta}, \\ &\Rightarrow \partial_{r}\left(\rho u^{r}u_{\phi}r^{2} - 2\eta\sigma^{r}_{\phi}r^{2}\right) = -r^{2}u_{\phi}\partial_{\theta}q^{\theta}, \\ &\Rightarrow \partial_{r}\left(\frac{\dot{M}}{2\pi}u_{\phi} + 4rH\eta\sigma^{r}_{\phi}\right) = 2Hu_{\phi}\epsilon,\end{aligned} \tag{A14}$$

where we integrated vertically and used Equation (16). Analogously, using Equation (11) we obtain

$$\partial_{r}\left(\frac{\dot{M}}{2\pi}u_{t} - 4rH\Omega\eta\sigma^{r}_{\phi}\right) = 2Hu_{t}\epsilon. \tag{A15}$$

The vertical integration of the divergence of the heat flux is as follows: Since, on average, $\boldsymbol{q} = q^\theta \boldsymbol{\partial}_\theta$, we have $\nabla_\mu q^\mu = \partial_\theta q^\theta$ and by Equation (A2), $q^\theta = rq^{\hat{\hat{\theta}}}$. Vertically integrating yields

$$\int_{\theta_{\min}}^{\theta_{\max}} \partial_\theta q^\theta r d\theta = rq^\theta \Big|_{\theta_{\min}}^{\theta_{\max}} = 2q^{\tilde{\tilde{\theta}}} = 2H\epsilon, \tag{A16}$$

where $q^{\tilde{\tilde{\theta}}}$ is the averaged energy flux radiating out of a face of the disk, as measured by an observer on the LRF, which we approximate as the half-thickness of the disk H times the average energy density per unit proper time ϵ lost by the disk. With the variable change $z = 8\pi r H \eta \sigma_\phi^r / \dot{M}$ and $y = 4\pi H \epsilon / \dot{M}$ the equations reduce to

$$\partial_r (u_\phi + z) = y u_\phi, \tag{A17a}$$

$$\partial_r (u_t - \Omega z) = y u_t. \tag{A17b}$$

Using the relation $\partial_r u_t = -\Omega \partial_r u_\phi$ (see Equation (10.7.29) in [178]) and $\partial_r \left(u_t + \Omega u_\phi\right) = u_\phi \partial_r \Omega$ we can combine the previous equations to obtain

$$z = -\frac{y\left(u_t + \Omega u_\phi\right)}{\partial_r \Omega}, \tag{A18a}$$

$$\partial_r \left(AB^2\right) = B \partial_r u_\phi, \tag{A18b}$$

with $A = y/\partial_r \Omega$ and $B = u_t + \Omega u_\phi$. To integrate these equations we use the zero torque condition $z(r = r^*) = 0$ where r^* is the radius of the innermost stable circular orbit, which gives the relation

$$y = \frac{\partial_r \Omega}{\left(u_t + \Omega u_\phi\right)^2} \int_{r^*}^{r} (u_t + \Omega u_\phi) \partial_r u_\phi dr = \frac{\partial_r \Omega}{\left(u_t + \Omega u_\phi\right)^2} \left(u_t u_\phi |_{r^*}^r - 2 \int_{r^*}^{r} u_\phi \partial_r u_t dr \right), \tag{A19}$$

or, equivalently,

$$8\pi H r \rho \nu_{\text{turb}} \sigma_\phi^r \approx 8\pi H r \Pi \nu_{\text{turb}} \sigma_\phi^r = -\frac{\dot{M}}{\left(u_t + \Omega u_\phi\right)} \left(u_t u_\phi |_{r^*}^r - 2 \int_{r^*}^{r} u_\phi \partial_r u_t dr \right). \tag{A20}$$

Using Equation (5), the approximation $\gamma_{\tilde{r}} \approx 1$ and the variable change $r = xM^2$ the integral can be easily evaluated by partial fractions

$$8\pi H r \rho \nu_{\text{turb}} \sigma_\phi^r = \dot{M} M f(x, x^*), \tag{A21a}$$

$$f(x, x^*) = \frac{x^3 + a}{x^{3/2}\sqrt{x^3 - 3x + 2a}} \left[x - x^* - \frac{3}{2} a \ln\left(\frac{x}{x^*}\right) + \frac{1}{2} \sum_{i=1}^{3} \frac{a x_i^2 - 2x_i + a}{x_i^2 - 1} \ln\left(\frac{x - x_i}{x^* - x_i}\right) \right], \tag{A21b}$$

where x_1, x_2, x_3 are the roots of the polynomial $x^3 - 3x + 2a$.

Appendix C. Nuclear Statistical Equilibrium

The results in this section appear in [179]. We include them here since they are necessary to solve Equation (19). Neutrino dominated accretion disks reach densities above $\sim 10^7$ g cm^{-3} and temperatures above $\sim 5 \times 10^9$ K. For these temperatures, forward and reverse nuclear reactions are balanced and the abundances in the plasma are determined by the condition $\mu_i = Z_i \mu_p + N_i \mu_n$, that is, the Nuclear Statistical Equilibrium. However, for densities above 10^6 g cm^{-3}, the electron screening of charged particle reactions can affect the nuclear reaction rates. For this reason, to obtain an accurate NSE state it is necessary to include Coulomb corrections to the ion chemical potential. The Coulomb correction to the i-th chemical potential is given by

$$\frac{\mu_i^C}{T} = K_1\left[\Gamma_i\sqrt{\Gamma_i + K_2} - K_2\ln\left(\sqrt{\frac{\Gamma_i}{K_2}} + \sqrt{1+\frac{\Gamma_i}{K_2}}\right)\right] + 2K_3\left[\sqrt{\Gamma_i} - \arctan\sqrt{\Gamma_i}\right] + Z_1\left[\Gamma_i - Z_2\ln\left(1+\frac{\Gamma_i}{Z_1}\right)\right] + \frac{Z_3}{2}\ln\left(1+\frac{\Gamma_i^2}{Z_4}\right), \quad \text{(A22)}$$

and the ion coupling parameter in terms of the electron coupling parameter is $\Gamma_i = \Gamma_e Z_i^{5/3}$ with

$$\Gamma_e = \frac{e^2}{T}\left(\frac{4\pi Y_e n_B}{3}\right)^{1/3}. \quad \text{(A23)}$$

where e is the electron charge. The parameters K_i, C_i are given in Table A1.

Table A1. Constants appearing in Equation (A22). See [179].

K_1	K_2	K_3	Z_1	Z_2	Z_3	Z_4
−0.907347	0.62849	0.278497	4.50×10^{-3}	170.0	-8.4×10^{-5}	3.70×10^{-3}

Appendix D. Neutrino Interactions and Cross-Sections

In this appendix we include the neutrino emission rates and neutrino cross-sections used in the accretion disk model. These expressions have been covered in [180–186]. We also include the expression energy emission rate for $\nu\bar{\nu}$ annihilation into electron–positron pairs. Whenever possible we write the rates in terms of generalized Fermi functions since some numerical calculations were done following [187]. We list in Table A2 some useful expressions and constants in Planck units. The numerical values can be found in [141].

Table A2. Constants used throughout this appendix to calculate emissivities and cross-sections. All quantities are reported in Planck units.

Symbol	Value	Name
M_w	6.584×10^{-18}	W boson mass
g_w	0.653	Weak coupling constant
g_a	1.26	Axial-vector coupling constant
α^*	$\frac{1}{137}$	Fine structure constant
$\sin^2\theta_W$	0.231	Weinberg angle
$\cos^2\theta_c$	0.947	Cabibbo angle
G_F	1.738×10^{33}	Fermi coupling constant
$C_{v,e}$	$2\sin^2\theta_W + 1/2$	Weak interaction vector constant for ν_e
$C_{a,e}$	$1/2$	Weak interaction axial-vector constant for ν_e
$C_{v,e}$	$C_{v,e} - 1$	Weak interaction vector constant for ν_x
$C_{a,e}$	$C_{a,e} - 1$	Weak interaction axial-vector constant for ν_x
σ_0	6.546×10^{21}	Weak interaction cross-section

Appendix D.1. Neutrino Emissivities

- Pair annihilation: $e^- + e^+ \to \nu + \bar{\nu}$

This process generates neutrinos of all flavors but around 70% are electron neutrinos [71]. This is due to the fact that the only charged leptons in the accretion systems we study are electrons and positrons, so creation of electron neutrinos occurs via either charged or neutral electroweak currents while creation of non-electronic neutrinos can only

occur through neutral currents. Using the electron or positron four-momentum $p = (E, \boldsymbol{p})$, the Dicus cross-section for a particular flavor i is [180]

$$\sigma_{D,i} = \frac{G_F^2}{12\pi E_{e^-} E_{e^+}} \left[C_{+,i} \left(m_e^4 + 3m_e^2 p_{e^-} \cdot p_{e^+} + 2(p_{e^-} \cdot p_{e^+})^2 \right) + 3C_{-,i} \left(m_e^4 + m_e^2 p_{e^-} \cdot p_{e^+} \right) \right]. \quad \text{(A24)}$$

The factors $C_{\pm,i}$, are written in terms of the weak interaction vector and axial-vector constants: $C_{\pm,i} = C_{v,i}^2 \pm C_{a,i}^2$ [141]. Representing the Fermi–Dirac distribution for electrons (positrons) as f_{e^-} (f_{e^+}) with $\eta_{e^\mp}$ the electron (positron) degeneracy parameter including its rest mass. The number and energy emission rates can be calculated by replacing $\Lambda = 2$ and $\Lambda = E_{e^-} + E_{e^+}$ in the integral [184]:

$$\frac{4}{(2\pi)^6} \int \Lambda \sigma_D f_{e^-} f_{e^+} d^3\boldsymbol{p}_{e^-} d^3\boldsymbol{p}_{e^+}, \quad \text{(A25)}$$

giving the expressions

$$\begin{aligned} R_{\nu_i+\bar{\nu}_i} = {} & \frac{G_F^2 m_e^8}{18\pi} [C_{+,i}(8\mathbb{U}_1\mathbb{V}_1 + 5\mathbb{U}_{-1}\mathbb{V}_{-1} + 9\mathbb{U}_0\mathbb{V}_0 - 2\mathbb{U}_{-1}\mathbb{V}_1 - 2\mathbb{U}_1\mathbb{V}_{-1}) \\ & + 9C_{-,i}(\mathbb{U}_{-1}\mathbb{V}_{-1} + \mathbb{U}_0\mathbb{V}_0)], \quad \text{(A26a)} \\ Q_{\nu_i+\bar{\nu}_i} = {} & \frac{G_F^2 m_e^9}{36\pi} [C_{+,i}(8(\mathbb{U}_2\mathbb{V}_1 + \mathbb{U}_1\mathbb{V}_2) + 7(\mathbb{U}_1\mathbb{V}_0 + \mathbb{U}_0\mathbb{V}_1) + 5(\mathbb{U}_{-1}\mathbb{V}_0 + \mathbb{U}_0\mathbb{V}_{-1}) \\ & - 2(\mathbb{U}_2\mathbb{V}_{-1} + \mathbb{U}_{-1}\mathbb{V}_2)) + 9C_{-,i}(\mathbb{U}_0(\mathbb{V}_1 + \mathbb{V}_{-1}) + \mathbb{V}_0(\mathbb{U}_1 + \mathbb{U}_{-1}))]. \quad \text{(A26b)} \end{aligned}$$

The functions $\mathbb{U}, \mathbb{V}$ can be written in terms of generalized Fermi functions

$$\mathbb{U}_j = \sqrt{2}\xi^{3/2} \sum_{k=0}^{j+1} \binom{j+1}{k} \xi^k \mathcal{F}_{k+1/2,0}(\xi, \eta_{e^-}), \quad \text{(A27a)}$$

$$\mathbb{V}_j = \sqrt{2}\xi^{3/2} \sum_{k=0}^{j+1} \binom{j+1}{k} \xi^k \mathcal{F}_{k+1/2,0}(\xi, \eta_{e^+}). \quad \text{(A27b)}$$

It is often useful to define the functions

$$\varepsilon_i^m = \frac{2G_F^2 (m_e)^4}{3(2\pi)^7} \int f_{e^-} f_{e^+} \left(E_{e^-}^m + E_{e^+}^m \right) \sigma_{D,i} \, d^3\mathbf{p}_{e^-} d^3\mathbf{p}_{e^+}. \quad \text{(A28)}$$

For $m = 0$ and $m = 1$ Equation (A28) gives the neutrino and antineutrino number emissivity (neutrino production rate), and the neutrino and antineutrino energy emissivity (energy per unit volume per unit time) for a certain flavor i, respectively (that is, Equation (A26)). Hence, not only we are able to calculate the total number and energy emissivity, but we can also calculate the neutrino or antineutrino energy moments with

$$\langle E_{\nu_i(\bar{\nu}_i)}^m \rangle = \frac{\varepsilon_i^m}{\varepsilon_i^0}, \text{ for } m \geq 1. \quad \text{(A29)}$$

- Electron capture and positron capture: $p + e^- \to n + \nu_e$, $n + e^+ \to p + \bar{\nu}_e$ and $A + e^- \to A' + \nu_e$

Due to lepton number conservation this process generated only electron (anti)neutrinos. The number and energy emission rates for electron and positron capture by nucleons are

$$R_{\nu_e} = \frac{m_e^5 G_F^2 \cos^2\theta_c}{\sqrt{2}\pi^3}\left(1+3g_A^2\right)\Delta_{np}\xi^{3/2}\Big[\xi^3\mathcal{F}_{7/2,\chi}(\xi,\eta_{e^-}) + (3-2\mathbb{Q})\xi^2\mathcal{F}_{5/2,\chi}(\xi,\eta_{e^-}) + (1-\mathbb{Q})(3-\mathbb{Q})\xi\mathcal{F}_{3/2,\chi}(\xi,\eta_{e^-}) + (1-\mathbb{Q})^2\mathcal{F}_{1/2,\chi}(\xi,\eta_{e^-})\Big], \quad \text{(A30a)}$$

$$Q_{\nu_e} = \frac{m_e^6 G_F^2 \cos^2\theta_c}{\sqrt{2}\pi^3}\left(1+3g_A^2\right)\Delta_{np}\xi^{3/2}\Big[\xi^4\mathcal{F}_{9/2,\chi}(\xi,\eta_{e^-}) + \xi^3(4-3\mathbb{Q})\mathcal{F}_{7/2,\chi}(\xi,\eta_{e^-}) + 3(\mathbb{Q}-1)(\mathbb{Q}-2)\xi^2\mathcal{F}_{5/2,\chi}(\xi,\eta_{e^-}) + (1-\mathbb{Q})^2(4-\mathbb{Q})\xi\mathcal{F}_{3/2,\chi}(\xi,\eta_{e^-}) + (1-\mathbb{Q})^3\mathcal{F}_{1/2,\chi}(\xi,\eta_{e^-})\Big], \quad \text{(A30b)}$$

$$R_{\bar{\nu}_e} = \frac{m_e^5 G_F^2 \cos^2\theta_c}{\sqrt{2}\pi^3}\left(1+3g_A^2\right)\Delta_{pn}\xi^{3/2}\Big[\xi^3\mathcal{F}_{7/2,0}(\xi,\eta_{e^+}) + (3+2\mathbb{Q})\xi^2\mathcal{F}_{5/2,0}(\xi,\eta_{e^+}) + (1+\mathbb{Q})(3+\mathbb{Q})\xi\mathcal{F}_{3/2,0}(\xi,\eta_{e^+}) + (1+\mathbb{Q})^2\mathcal{F}_{1/2,0}(\xi,\eta_{e^+})\Big], \quad \text{(A30c)}$$

$$Q_{\bar{\nu}_e} = \frac{m_e^6 G_F^2 \cos^2\theta_c}{\sqrt{2}\pi^3}\left(1+3g_A^2\right)\Delta_{np}\xi^{3/2}\Big[\xi^4\mathcal{F}_{9/2,0}(\xi,\eta_{e^+}) + \xi^3(4+3\mathbb{Q})\mathcal{F}_{7/2,0}(\xi,\eta_{e^+}) + 3(\mathbb{Q}+1)(\mathbb{Q}+2)\xi^2\mathcal{F}_{5/2,0}(\xi,\eta_{e^+}) + (1+\mathbb{Q})^2(4+\mathbb{Q})\xi\mathcal{F}_{3/2,0}(\xi,\eta_{e^+}) + (1+\mathbb{Q})^3\mathcal{F}_{1/2,0}(\xi,\eta_{e^+})\Big], \quad \text{(A30d)}$$

where $\Delta_{ij} = \left(n_i - n_j\right)/\left(\exp\left(\eta_i - \eta_j\right) - 1\right),\ i,j \in \{p,n\}$ are the Fermi blocking factors in the nucleon phase spaces and $\mathbb{Q} = (m_n - m_p)m_e \approx 2.531$ is the nucleon mass difference. The number and energy emission rates for electron capture by an ion i are

$$R_{\nu_e,i} = \frac{\sqrt{2}m_e^5 G_F^2 \cos^2\theta_c}{7\pi^3} g_A^2 n_i \kappa_{Z_i}\kappa_{N_i}\xi^{3/2}\Big[\xi^3\mathcal{F}_{7/2,\bar{\chi}}(\xi,\eta_{e^-}) + (3-2\mathbb{Q})\xi^2\mathcal{F}_{5/2,\bar{\chi}}(\xi,\eta_{e^-}) + (1-\mathbb{Q})(3-\mathbb{Q})\xi\mathcal{F}_{3/2,\bar{\chi}}(\xi,\eta_{e^-})(1-\mathbb{Q})^2\mathcal{F}_{1/2,\bar{\chi}}(\xi,\eta_{e^-})\Big], \quad \text{(A31a)}$$

$$Q_{\nu_e,i} = \frac{\sqrt{2}m_e^6 G_F^2 \cos^2\theta_c}{7\pi^3} g_A^2 n_i \kappa_{Z_i}\kappa_{N_i}\xi^{3/2}\Big[\xi^4\mathcal{F}_{9/2,\bar{\chi}}(\xi,\eta_{e^-}) + \xi^3(4-3\mathbb{Q})\mathcal{F}_{7/2,\bar{\chi}}(\xi,\eta_{e^-}) + 3(\mathbb{Q}-1)(\mathbb{Q}-2)\xi^2\mathcal{F}_{5/2,\bar{\chi}}(\xi,\eta_{e^-}) + (1-\mathbb{Q})^2(4-\mathbb{Q})\xi\mathcal{F}_{3/2,\bar{\chi}}(\xi,\eta_{e^-}) + (1-\mathbb{Q})^3\mathcal{F}_{1/2,\bar{\chi}}(\xi,\eta_{e^-})\Big]. \quad \text{(A31b)}$$

The lower integration limits in these expressions are given by $\chi = (\mathbb{Q}-1)/\xi$ and $\bar{\chi} = (\mu_n - \mu_p + \Delta)/T - 1/\xi$ where $\Delta \approx 2.457 \times 10^{-22}$ is the energy of the neutron $1f_{5/2}$ state above the ground state. The functions $\kappa_{Z_i}, \kappa_{N_i}$ are

$$\kappa_{Z_i} = \begin{cases} 0 & \text{if } Z_i \leq 20. \\ Z_i - 20 & \text{if } 20 < Z_i \leq 28., \\ 8 & \text{if } Z_i > 28. \end{cases} \quad \kappa_{N_i} = \begin{cases} 6 & \text{if } N_i \leq 34. \\ 40 - N_i & \text{if } 34 < N_i \leq 40. \\ 0 & \text{if } N_i > 40. \end{cases} \quad \text{(A32)}$$

- Plasmon decay: $\tilde{\gamma} \to \nu + \bar{\nu}$.

$$R_{\nu_e+\bar{\nu}_e} = \frac{C_{v,e}\sigma_0 T^8}{96\pi^3 m_e^2 \alpha^*}\tilde{\gamma}^6(\tilde{\gamma}+1)\exp(-\tilde{\gamma}), \quad \text{(A33a)}$$

$$Q_{\nu_e+\bar{\nu}_e} = \frac{C_{v,e}\sigma_0 T^9}{192\pi^3 m_e^2 \alpha^*}\tilde{\gamma}^6\left(\tilde{\gamma}^2+2\tilde{\gamma}+2\right)\exp(-\tilde{\gamma}), \quad \text{(A33b)}$$

$$R_{\nu_x+\bar{\nu}_x} = \frac{C_{v,x}\sigma_0 T^8}{48\pi^3 m_e^2 \alpha^*}\tilde{\gamma}^6(\tilde{\gamma}+1)\exp(-\tilde{\gamma}), \quad \text{(A33c)}$$

$$Q_{\nu_x+\bar{\nu}_x} = \frac{C_{v,x}\sigma_0 T^9}{96\pi^3 m_e^2 \alpha^*}\tilde{\gamma}^6\left(\tilde{\gamma}^2+2\tilde{\gamma}+2\right)\exp(-\tilde{\gamma}), \quad \text{(A33d)}$$

where $\tilde{\gamma} = \tilde{\gamma}_0\sqrt{\left(\pi^2 + 3(\eta_{e^-} + 1/\xi)^2\right)/3}$ and $\tilde{\gamma}_0 = 2\sqrt{\frac{\alpha^*}{3\pi}} \approx 5.565 \times 10^{-2}$.

- Nucleon-nucleon bremsstrahlung $n_1 + n_2 \to n_3 + n_4 + \nu + \bar{\nu}$.

The nucleon-nucleon bremsstrahlung produces the same amount of neutrinos of all three flavors. The number and energy emission rates can be approximated by (see, e.g., [186])

$$R_{\nu_i+\bar{\nu}_i} = \left(2.59\times10^{13}\right)\left(X_p^2+X_n^2+\frac{28}{3}X_pX_n\right)n_B^2\xi^{9/2}, \tag{A34a}$$

$$Q_{\nu_i+\bar{\nu}_i} = \left(4.71\times10^{-9}\right)\left(X_p^2+X_n^2+\frac{28}{3}X_pX_n\right)n_B^2\xi^{10/2}. \tag{A34b}$$

Appendix D.2. Cross-Sections

We consider four interactions to describe the (anti)neutrino total cross-section.

- Neutrino annihilation: $(\nu+\bar{\nu}\rightarrow e^-+e^+)$.

$$\sigma_{\nu_e\bar{\nu}_e} = \frac{4}{3}K_{\nu_e\bar{\nu}_e}\sigma_0\frac{\langle E_{\nu_e}\rangle\langle E_{\bar{\nu}_e}\rangle}{m_e^2} \text{ with } K_{\nu_e\bar{\nu}_e} = \frac{1+4\sin^2\theta_W+8\sin^4\theta_W}{12}, \tag{A35a}$$

$$\sigma_{\nu_x\bar{\nu}_x} = \frac{4}{3}K_{\nu_x\bar{\nu}_x}\sigma_0\frac{\langle E_{\nu_x}\rangle\langle E_{\bar{\nu}_x}\rangle}{m_e^2} \text{ with } K_{\nu_x\bar{\nu}_x} = \frac{1-4\sin^2\theta_W+8\sin^4\theta_W}{12}, \tag{A35b}$$

- Electron (anti)neutrino absorption by nucleons: $(\nu_e+n\rightarrow e^-+p$ and $\bar{\nu}_e+p\rightarrow e^++n)$.

$$\sigma_{\nu_e n} = \sigma_0\left(\frac{1+3g_a^2}{4}\right)\left(\frac{\langle E_{\nu_e}\rangle}{m_e}+\mathbb{Q}\right)^2\sqrt{1-\frac{1}{\left(\frac{\langle E_{\nu_e}\rangle}{m_e}+\mathbb{Q}\right)^2}}, \tag{A36a}$$

$$\sigma_{\bar{\nu}_e p} = 3.83\times10^{22}\left(\frac{\wp\langle E_{\bar{\nu}_e}\rangle}{m_e}-\mathbb{Q}\right)^2\sqrt{1-\frac{1}{\left(\frac{\wp\langle E_{\bar{\nu}_e}\rangle}{m_e}-\mathbb{Q}\right)^2}}\left(\frac{\wp\langle E_{\bar{\nu}_e}\rangle}{m_e}\right)^{g(E_{\bar{\nu}_e})}, \tag{A36b}$$

$$g(E_{\bar{\nu}_e}) = -0.07056+0.02018\ln\left(\frac{\wp\langle E_{\bar{\nu}_e}\rangle}{m_e}\right)-0.001953\ln^3\left(\frac{\wp\langle E_{\bar{\nu}_e}\rangle}{m_e}\right). \tag{A36c}$$

where $\wp = 0.511$.

- (anti)neutrino scattering by baryons: $(\nu+A_i\rightarrow\nu+A_i$ and $\bar{\nu}+A_i\rightarrow\bar{\nu}+A_i)$.

$$\sigma_p = \frac{\sigma_0\langle E\rangle^2}{4m_e^2}\left(4\sin^4\theta_W-2\sin^2\theta_W+\frac{1+3g_a^2}{4}\right), \tag{A37a}$$

$$\sigma_n = \frac{\sigma_0\langle E\rangle^2}{4m_e^2}\frac{1+3g_a^2}{4}, \tag{A37b}$$

$$\sigma_{A_i} = \frac{\sigma_0A_i^2\langle E\rangle^2}{16m_e^2}\left[\left(4\sin^2\theta_W-1\right)\frac{Z_i}{A_i}+1-\frac{Z_i}{A_i}\right]. \tag{A37c}$$

- (anti)neutrino scattering by electrons or positrons: $(\nu+e^\pm\rightarrow\nu+e^\pm$ and $\bar{\nu}+e^\pm\rightarrow\bar{\nu}+e^\pm)$.

$$\sigma_e = \frac{3}{8}\sigma_0\xi\frac{\langle E\rangle}{m_e}\left(1+\frac{\eta_e+1/\xi}{4}\right)\left[(C_{v,i}+n_\ell C_{a,i})^2+\frac{1}{3}(C_{v,i}-n_\ell C_{a,i})^2\right]. \tag{A38}$$

Here, n_ℓ is the (anti)neutrino lepton number (that is, 1 for neutrinos and -1 for antineutrinos, depending on the cross-section to be calculated), and in the last four expressions, $\langle E\rangle$ is replaced by the average (anti)neutrino energy of the corresponding flavor. With these expressions, the total opacity for neutrinos or antineutrinos is

$$\kappa_{\nu_i(\bar{\nu}_i)} = \frac{\sum_i\sigma_in_i}{\rho}, \tag{A39}$$

where n_i is the number density of the target particle associated with the process corresponding to the cross-section σ_i. The (anti)neutrino optical depth appearing in Equation (32) can then be approximated as

$$\tau_{\nu_i(\bar{\nu}_i)} = \int \kappa_{\nu_i(\bar{\nu}_i)} \rho d\theta \approx \kappa_{\nu_i(\bar{\nu}_i)} \rho H. \tag{A40}$$

Appendix D.3. Neutrino-Antineutrino Pair Annihilation

Since the main interaction between $\nu\bar{\nu}$ is the annihilation into $e^- e^+$, this process above neutrino-cooled disks has been proposed as the origin of the energetic plasma involved in the production of GRBs. Once the (anti)neutrino energy emissivity and average energies are calculated it is possible to calculate the energy deposition rate of the process $\nu_i + \bar{\nu}_i \to e^- + e^+$ for each flavor i. Ignoring Pauli blocking effects in the phase spaces of electron and positrons, the local energy deposition rate at a position $\mathbf{r}$ by $\nu\bar{\nu}$ annihilation can be written in terms of the neutrino and antineutrino distributions $f_{\nu_i} = f_{\nu_i}(\mathbf{r}, E_\nu), f_{\bar{\nu}_i} = f_{\bar{\nu}_i}(\mathbf{r}, E_{\bar{\nu}})$ as [155]

$$\begin{aligned} Q_{\nu_i\bar{\nu}_i} = A_{1,i} \int_0^\infty dE_{\nu_i} \int_0^\infty dE_{\bar{\nu}_i} E_{\nu_i}^3 E_{\bar{\nu}_i}^3 (E_{\nu_i} + E_{\bar{\nu}_i}) \int_{S_2} d\Omega_{\nu_i} \int_{S_2} d\Omega_{\bar{\nu}_i} f_{\nu_i} f_{\bar{\nu}_i} (1 - \cos\theta)^2, \\ + A_{2,i} \int_0^\infty dE_{\nu_i} \int_0^\infty dE_{\bar{\nu}_i} E_{\nu_i}^2 E_{\bar{\nu}_i}^2 (E_{\nu_i} + E_{\bar{\nu}_i}) \int_{S_2} d\Omega_{\nu_i} \int_{S_2} d\Omega_{\bar{\nu}_i} f_{\nu_i} f_{\bar{\nu}_i} (1 - \cos\theta), \end{aligned} \tag{A41}$$

where we have introduced the constants appearing in Equation (80)

$$\begin{aligned} A_{1,i} &= \frac{\sigma_0 \left[(C_{v,i} - C_{a,i})^2 + (C_{v,i} + C_{a,i})^2 \right]}{12\pi^2 m_e^2}, \\ A_{2,i} &= \frac{\sigma_0 \left[2C_{v,i}^2 - C_{a,i}^2 \right]}{6\pi^2 m_e^2}. \end{aligned} \tag{A42}$$

In Equation (A41), θ is the angle between the neutrino and antineutrino momentum and $d\Omega$ is the differential solid angle of the incident (anti)neutrino at $\mathbf{r}$. The integral can be re-written in terms of the total intensity (energy integrated intensity) $I_\nu = \int E_\nu^3 f_\nu dE_\nu$ as [156]

$$\begin{aligned} Q_{\nu_i\bar{\nu}_i} = A_{1,i} \int_{S_2} d\Omega_{\nu_i} I_{\nu_i} \int_{S_2} d\Omega_{\bar{\nu}_i} I_{\bar{\nu}_i} (\langle E_{\nu_i} \rangle + \langle E_{\bar{\nu}_i} \rangle)(1 - \cos\theta)^2 \\ + A_{2,i} \int_{S_2} d\Omega_{\nu_i} I_{\nu_i} \int_{S_2} d\Omega_{\bar{\nu}_i} I_{\bar{\nu}_i} \frac{\langle E_{\nu_i} \rangle + \langle E_{\bar{\nu}_i} \rangle}{\langle E_{\nu_i} \rangle \langle E_{\bar{\nu}_i} \rangle} (1 - \cos\theta). \end{aligned} \tag{A43}$$

The incident radiation intensity passing through the solid differential angle $d\Omega$ at $\mathbf{r}$ is the intensity $I_{\mathbf{r}_d,\nu}$ emitted from the point on the disk $\mathbf{r}_d$ diluted by the inverse square distance $r_k = |\mathbf{r} - \mathbf{r}_d|$ between both points. Finally, assuming that each point $\mathbf{r}_d$ on the disk's surface acts as a half-isotropic radiator of (anti)neutrinos, the total flux emitted at $\mathbf{r}_d$ is $F_{\mathbf{r}_d,\nu} = \int_0^{\pi/2} \int_0^{2\pi} I_{\mathbf{r}_d,\nu} \cos\theta' \sin\theta' d\theta' d\phi' = \pi I_{\mathbf{r}_d,\nu}$, with θ', ϕ' the direction angles at $\mathbf{r}_d$. Collecting all obtains

$$\begin{aligned} Q_{\nu_i\bar{\nu}_i} = A_{1,i} \int\limits_{\mathbf{r}_{d,\nu_i} \in \text{disk}} d\mathbf{r}_{d,\nu_i} \int\limits_{\mathbf{r}_{d,\bar{\nu}_i} \in \text{disk}} d\mathbf{r}_{d,\bar{\nu}_i} \frac{F_{\mathbf{r}_d,\nu_i}}{r_{k,\nu_i}^2} \frac{F_{\mathbf{r}_d,\bar{\nu}_i}}{r_{k,\bar{\nu}_i}^2} (\langle E_{\nu_i} \rangle + \langle E_{\bar{\nu}_i} \rangle)(1 - \cos\theta)^2 \\ + A_{2,i} \int\limits_{\mathbf{r}_{d,\nu_i} \in \text{disk}} d\mathbf{r}_{d,\nu_i} \int\limits_{\mathbf{r}_{d,\bar{\nu}_i} \in \text{disk}} d\mathbf{r}_{d,\bar{\nu}_i} \frac{F_{\mathbf{r}_d,\nu_i}}{r_{k,\nu_i}^2} \frac{F_{\mathbf{r}_d,\bar{\nu}_i}}{r_{k,\bar{\nu}_i}^2} \frac{\langle E_{\nu_i} \rangle + \langle E_{\bar{\nu}_i} \rangle}{\langle E_{\nu_i} \rangle \langle E_{\bar{\nu}_i} \rangle} (1 - \cos\theta). \end{aligned} \tag{A44}$$

References

1. De Salas, P.F.; Forero, D.V.; Ternes, C.A.; Tortola, M.; Valle, J.W.F. Status of neutrino oscillations 2018: 3σ hint for normal mass ordering and improved CP sensitivity. *Phys. Lett. B* **2018**, *782*, 633–640. [CrossRef]
2. Wolfenstein, L. Neutrino Oscillations in Matter. *Phys. Rev. D* **1978**, *17*, 2369–2374. [CrossRef]
3. Mikheyev, S.P.; Smirnov, A.Y. Resonant amplification of ν oscillations in matter and solar-neutrino spectroscopy. *Il Nuovo Cimento C* **1986**, *9*, 17–26. [CrossRef]
4. Barbieri, R.; Dolgov, A. Neutrino oscillations in the early universe. *Nucl. Phys. B* **1991**, *349*, 743–753. [CrossRef]
5. Enqvist, K.; Kainulainen, K.; Maalampi, J. Refraction and Oscillations of Neutrinos in the Early Universe. *Nucl. Phys. B* **1991**, *349*, 754–790. [CrossRef]
6. Savage, M.J.; Malaney, R.A.; Fuller, G.M. Neutrino Oscillations and the Leptonic Charge of the Universe. *Astrophys. J.* **1991**, *368*, 1–11. [CrossRef]
7. Kostelecky, V.A.; Samuel, S. Neutrino oscillations in the early universe with an inverted neutrino mass hierarchy. *Phys. Lett. B* **1993**, *318*, 127–133. [CrossRef]
8. Kostelecky, V.A.; Samuel, S. Nonlinear neutrino oscillations in the expanding universe. *Phys. Rev. D* **1994**, *49*, 1740–1757. [CrossRef]
9. Kostelecký, V.; Pantaleone, J.; Samuel, S. Neutrino oscillations in the early universe. *Phys. Lett. B* **1993**, *315*, 46–50. [CrossRef]
10. McKellar, B.H.J.; Thomson, M.J. Oscillating doublet neutrinos in the early universe. *Phys. Rev. D* **1994**, *49*, 2710–2728. [CrossRef]
11. Lunardini, C.; Smirnov, A.Y. High-energy neutrino conversion and the lepton asymmetry in the universe. *Phys. Rev. D* **2001**, *64*, 73006. [CrossRef]
12. Dolgov, A.D.; Hansen, S.H.; Pastor, S.; Petcov, S.T.; Raffelt, G.G.; Semikoz, D.V. Cosmological bounds on neutrino degeneracy improved by flavor oscillations. *Nucl. Phys. B* **2002**, *632*, 363–382. [CrossRef]
13. Wong, Y.Y. Analytical treatment of neutrino asymmetry equilibration from flavor oscillations in the early universe. *Phys. Rev. D* **2002**, *66*, 25015. [CrossRef]
14. Abazajian, K.N.; Beacom, J.F.; Bell, N.F. Stringent constraints on cosmological neutrino-antineutrino asymmetries from synchronized flavor transformation. *Phys. Rev. D* **2002**, *66*, 13008. [CrossRef]
15. Kirilova, D.P. Neutrino oscillations and the early universe. *Cent. Eur. J. Phys.* **2004**, *2*, 467–491. [CrossRef]
16. Bahcall, J.N.; Concepcion Gonzalez-Garcia, M.; na-Garay, C.P. Solar Neutrinos Before and After KamLAND. *J. High Energy Phys.* **2003**, *2003*, 09. [CrossRef]
17. Balantekin, A.B.; Yuksel, H. Global Analysis of Solar Neutrino and KamLAND Data. *J. Phys. G Nucl. Part. Phys.* **2003**, *29*, 665. [CrossRef]
18. Fogli, G.L.; Lisi, E.; Marrone, A.; Montanino, D.; Palazzo, A.; Rotunno, A.M. Neutrino Oscillations: A Global Analysis. *arXiv* **2003**, arXiv:0310012.
19. de Holanda, P.C.; Smirnov, A.Y. Solar neutrinos: The SNO salt phase results and physics of conversion. *Astropart. Phys.* **2004**, *21*, 287–301. [CrossRef]
20. Giunti, C. Status of neutrino masses and mixing. *Eur. Phys. J. C* **2004**, *33*, 852–856. [CrossRef]
21. Maltoni, M.; Schwetz, T.; Tórtola, M.A.; Valle, J.W. Status of three-neutrino oscillations after the SNO-salt data. *Phys. Rev. D* **2003**, *68*, 113010. [CrossRef]
22. Dighe, A. Supernova neutrino oscillations: What do we understand? *J. Phys. Conf. Ser.* **2010**, *203*, 012015. [CrossRef]
23. Haxton, W.C.; Hamish Robertson, R.G.; Serenelli, A.M. Solar Neutrinos: Status and Prospects. *Annu. Rev. Astron. Astrophys.* **2013**, *51*, 21–61. [CrossRef]
24. Vissani, F. Solar neutrino physics on the beginning of 2017. *Nucl. Phys. At. Energy* **2017**, *18*, 5–12. [CrossRef]
25. Notzold, D.; Raffelt, G. Neutrino Dispersion at Finite Temperature and Density. *Nucl. Phys. B* **1988**, *307*, 924–936. [CrossRef]
26. Pantaleone, J. Neutrino oscillations at high densities. *Phys. Lett. B* **1992**, *287*, 128–132. [CrossRef]
27. Qian, Y.Z.; Fuller, G.M. Neutrino-neutrino scattering and matter enhanced neutrino flavor transformation in Supernovae. *Phys. Rev. D* **1995**, *51*, 1479–1494. [CrossRef] [PubMed]
28. Pastor, S.; Raffelt, G. Flavor oscillations in the supernova hot bubble region: Nonlinear effects of neutrino background. *Phys. Rev. Lett.* **2002**, *89*, 191101. [CrossRef]
29. Duan, H.; Fuller, G.M.; Qian, Y.Z. Collective neutrino flavor transformation in supernovae. *Phys. Rev. D* **2006**, *74*, 123004. [CrossRef]
30. Sawyer, R.F. Speed-up of neutrino transformations in a supernova environment. *Phys. Rev. D* **2005**, *72*, 45003. [CrossRef]
31. Fuller, G.M.; Qian, Y.Z. Simultaneous flavor transformation of neutrinos and antineutrinos with dominant potentials from neutrino-neutrino forward scattering. *Phys. Rev. D* **2006**, *73*, 23004. [CrossRef]
32. Duan, H.; Fuller, G.M.; Carlson, J.; Qian, Y.Z. Coherent Development of Neutrino Flavor in the Supernova Environment. *Phys. Rev. Lett.* **2006**, *97*, 241101. [CrossRef] [PubMed]
33. Fogli, G.L.; Lisi, E.; Marrone, A.; Mirizzi, A. Collective neutrino flavor transitions in supernovae and the role of trajectory averaging. *JCAP* **2007**, *0712*, 10. [CrossRef]
34. Duan, H.; Fuller, G.M.; Qian, Y.Z. A Simple Picture for Neutrino Flavor Transformation in Supernovae. *Phys. Rev. D* **2007**, *76*, 85013. [CrossRef]
35. Raffelt, G.G.; Sigl, G. Self-induced decoherence in dense neutrino gases. *Phys. Rev. D* **2007**, *75*, 83002. [CrossRef]
36. Esteban-Pretel, A.; Pastor, S.; Tomas, R.; Raffelt, G.G.; Sigl, G. Decoherence in supernova neutrino transformations suppressed by deleptonization. *Phys. Rev. D* **2007**, *76*, 125018. [CrossRef]

37. Esteban-Pretel, A.; Pastor, S.; Tomas, R.; Raffelt, G.G.; Sigl, G. Mu-tau neutrino refraction and collective three-flavor transformations in supernovae. *Phys. Rev. D* **2008**, *77*, 65024. [CrossRef]
38. Chakraborty, S.; Choubey, S.; Dasgupta, B.; Kar, K. Effect of Collective Flavor Oscillations on the Diffuse Supernova Neutrino Background. *JCAP* **2008**, *0809*, 13. [CrossRef]
39. Duan, H.; Fuller, G.M.; Carlson, J.; Qian, Y.Z. Flavor Evolution of the Neutronization Neutrino Burst from an O-Ne-Mg Core-Collapse Supernova. *Phys. Rev. Lett.* **2008**, *100*, 21101. [CrossRef]
40. Duan, H.; Fuller, G.M.; Carlson, J. Simulating nonlinear neutrino flavor evolution. *Comput. Sci. Dis.* **2008**, *1*, 015007. [CrossRef]
41. Dasgupta, B.; Dighe, A.; Mirizzi, A. Identifying neutrino mass hierarchy at extremely small theta(13) through Earth matter effects in a supernova signal. *Phys. Rev. Lett.* **2008**, *101*, 171801. [CrossRef] [PubMed]
42. Dasgupta, B.; Dighe, A. Collective three-flavor oscillations of supernova neutrinos. *Phys. Rev. D* **2008**, *77*, 113002. [CrossRef]
43. Sawyer, R.F. The multi-angle instability in dense neutrino systems. *Phys. Rev. D* **2009**, *79*, 105003. [CrossRef]
44. Duan, H.; Fuller, G.M.; Qian, Y.Z. Collective Neutrino Oscillations. *Ann. Rev. Nucl. Part. Sci.* **2010**, *60*, 569–594. [CrossRef]
45. Wu, M.R.; Qian, Y.Z. Resonances Driven by a Neutrino Gyroscope and Collective Neutrino Oscillations in Supernovae. *Phys. Rev. D* **2011**, *84*, 45009. [CrossRef]
46. Bilenky, S.M. Neutrino oscillations: Brief history and present status. *arXiv* **2014**, arXiv:1408.2864.
47. Kneller, J.P. The Physics Of Supernova Neutrino Oscillations. In Proceedings of the 12th Conference on the Intersections of Particle and Nuclear Physics (CIPANP 2015), Vail, CO, USA, 19–24 May 2015.
48. Volpe, C. Theoretical developments in supernova neutrino physics: Mass corrections and pairing correlators. *J. Phys. Conf. Ser.* **2016**, *718*, 62068. [CrossRef]
49. Mirizzi, A.; Tamborra, I.; Janka, H.T.; Saviano, N.; Scholberg, K.; Bollig, R.; Hüdepohl, L.; Chakraborty, S. Supernova neutrinos: production, oscillations and detection. *Nuovo Cimento Riv. Ser.* **2016**, *39*, 1–112. [CrossRef]
50. Horiuchi, S.; Kneller, J.P. What can be learned from a future supernova neutrino detection? *J. Phys. G Nucl. Phys.* **2018**, *45*, 43002. [CrossRef]
51. Zaizen, M.; Yoshida, T.; Sumiyoshi, K.; Umeda, H. Collective neutrino oscillations and detectabilities in failed supernovae. *Phys. Rev. D* **2018**, *98*, 103020. [CrossRef]
52. Zhang, B. *The Physics of Gamma-ray Bursts*; Cambridge University Press: Cambridge, UK, 2018. [CrossRef]
53. Ruffini, R.; Bernardini, M.G.; Bianco, C.L.; Vitagliano, L.; Xue, S.S.; Chardonnet, P.; Fraschetti, F.; Gurzadyan, V. Black Hole Physics and Astrophysics: The GRB-Supernova Connection and URCA-1 - URCA-2. In *The Tenth Marcel Grossmann Meeting, Proceedings of the MG10 Meeting Held at Brazilian Center for Research in Physics (CBPF), Rio de Janeiro, Brazil, 20–26 July 2003*; Novello, M., Bergliaffa, S.P., Ruffini, R., Eds.; World Scientific Publishing: Singapore, 2006; Volumes 3, p. 369. [CrossRef]
54. Ruffini, R.; Bernardini, M.G.; Bianco, C.L.; Caito, L.; Chardonnet, P.; Cherubini, C.; Dainotti, M.G.; Fraschetti, F.; Geralico, A.; Guida, R.; et al. On Gamma-ray Bursts. In *The Eleventh Marcel Grossmann Meeting On Recent Developments in Theoretical and Experimental General Relativity, Gravitation and Relativistic Field Theories*; Kleinert, H., Jantzen, R.T., Ruffini, R., Eds.; World Scientific: Singapore, 2008; pp. 368–505. [CrossRef]
55. Izzo, L.; Rueda, J.A.; Ruffini, R. GRB 090618: A candidate for a neutron star gravitational collapse onto a black hole induced by a type Ib/c supernova. *Astron. Astrophys.* **2012**, *548*, L5. [CrossRef]
56. Rueda, J.A.; Ruffini, R. On the Induced Gravitational Collapse of a Neutron Star to a Black Hole by a Type Ib/c Supernova. *Astrophys. J.* **2012**, *758*, L7. [CrossRef]
57. Fryer, C.L.; Rueda, J.A.; Ruffini, R. Hypercritical Accretion, Induced Gravitational Collapse, and Binary-Driven Hypernovae. *Astrophys. J.* **2014**, *793*, L36. [CrossRef]
58. Ruffini, R.; Wang, Y.; Enderli, M.; Muccino, M.; Kovacevic, M.; Bianco, C.L.; Penacchioni, A.V.; Pisani, G.B.; Rueda, J.A. GRB 130427A and SN 2013cq: A Multi-wavelength Analysis of An Induced Gravitational Collapse Event. *Astrophys. J.* **2015**, *798*, 10. [CrossRef]
59. Fryer, C.L.; Oliveira, F.G.; Rueda, J.A.; Ruffini, R. Neutron-Star-Black-Hole Binaries Produced by Binary-Driven Hypernovae. *Phys. Rev. Lett.* **2015**, *115*, 231102. [CrossRef]
60. Wang, Y.; Rueda, J.A.; Ruffini, R.; Becerra, L.; Bianco, C.; Becerra, L.; Li, L.; Karlica, M. Two Predictions of Supernova: GRB 130427A/SN 2013cq and GRB 180728A/SN 2018fip. *Astrophys. J.* **2019**, *874*, 39. [CrossRef]
61. Rueda, J.A.; Ruffini, R.; Karlica, M.; Moradi, R.; Wang, Y. Magnetic Fields and Afterglows of BdHNe: Inferences from GRB 130427A, GRB 160509A, GRB 160625B, GRB 180728A, and GRB 190114C. *Astrophys. J.* **2020**, *893*, 148. [CrossRef]
62. Rueda, J.A.; Ruffini, R.; Wang, Y. Induced Gravitational Collapse, Binary-Driven Hypernovae, Long Gramma-ray Bursts and Their Connection with Short Gamma-ray Bursts. *Universe* **2019**, *5*, 110. [CrossRef]
63. Becerra, L.; Bianco, C.L.; Fryer, C.L.; Rueda, J.A.; Ruffini, R. On the Induced Gravitational Collapse Scenario of Gamma-ray Bursts Associated with Supernovae. *Astrophys. J.* **2016**, *833*, 107. [CrossRef]
64. Bianco, C.L.; Ruffini, R.; Xue, S. The elementary spike produced by a pure e^+e^- pair-electromagnetic pulse from a Black Hole: The PEM Pulse. *Astron. Astrophys.* **2001**, *368*, 377–390. [CrossRef]
65. Ruffini, R.; Moradi, R.; Rueda, J.A.; Becerra, L.; Bianco, C.L.; Cherubini, C.; Filippi, S.; Chen, Y.C.; Karlica, M.; Sahakyan, N.; et al. On the GeV Emission of the Type I BdHN GRB 130427A. *Astrophys. J.* **2019**, *886*, 82. [CrossRef]
66. Ruffini, R.; Melon Fuksman, J.D.; Vereshchagin, G.V. On the Role of a Cavity in the Hypernova Ejecta of GRB 190114C. *Astrophys. J.* **2019**, *883*, 191. [CrossRef]

67. Ruffini, R.; Wang, Y.; Aimuratov, Y.; Barres de Almeida, U.; Becerra, L.; Bianco, C.L.; Chen, Y.C.; Karlica, M.; Kovacevic, M.; Li, L.; et al. Early X-ray Flares in GRBs. *Astrophys. J.* **2018**, *852*, 53. [CrossRef]
68. Ruffini, R.; Karlica, M.; Sahakyan, N.; Rueda, J.A.; Wang, Y.; Mathews, G.J.; Bianco, C.L.; Muccino, M. A GRB Afterglow Model Consistent with Hypernova Observations. *Astrophys. J.* **2018**, *869*, 101. [CrossRef]
69. Becerra, L.; Cipolletta, F.; Fryer, C.L.; Rueda, J.A.; Ruffini, R. Angular Momentum Role in the Hypercritical Accretion of Binary-driven Hypernovae. *Astrophys. J.* **2015**, *812*, 100. [CrossRef]
70. Becerra, L.; Ellinger, C.L.; Fryer, C.L.; Rueda, J.A.; Ruffini, R. SPH Simulations of the Induced Gravitational Collapse Scenario of Long Gamma-ray Bursts Associated with Supernovae. *Astrophys. J.* **2019**, *871*, 14. [CrossRef]
71. Becerra, L.; Guzzo, M.M.; Rossi-Torres, F.; Rueda, J.A.; Ruffini, R.; Uribe, J.D. Neutrino Oscillations within the Induced Gravitational Collapse Paradigm of Long Gamma-ray Bursts. *Astrophys. J.* **2018**, *852*, 120. [CrossRef]
72. Goodman, J. Are gamma-ray bursts optically thick? *Astrophys. J.* **1986**, *308*, L47–L50. [CrossRef]
73. Paczynski, B. Gamma-ray bursters at cosmological distances. *Astrophys. J.* **1986**, *308*, L43–L46. [CrossRef]
74. Eichler, D.; Livio, M.; Piran, T.; Schramm, D.N. Nucleosynthesis, neutrino bursts and gamma-rays from coalescing neutron stars. *Nature* **1989**, *340*, 126–128. [CrossRef]
75. Narayan, R.; Piran, T.; Shemi, A. Neutron star and black hole binaries in the Galaxy. *Astrophys. J.* **1991**, *379*, L17–L20. [CrossRef]
76. Balbus, S.A.; Hawley, J.F. A powerful local shear instability in weakly magnetized disks. I—Linear analysis. II—Nonlinear evolution. *Astrophys. J.* **1991**, *376*, 214–233. [CrossRef]
77. Hawley, J.F.; Balbus, S.A. A Powerful Local Shear Instability in Weakly Magnetized Disks. II. Nonlinear Evolution. *Astrophys. J.* **1991**, *376*, 223. [CrossRef]
78. Balbus, S.A.; Hawley, J.F. Instability, turbulence, and enhanced transport in accretion disks. *Rev. Mod. Phys.* **1998**, *70*, 1–53. [CrossRef]
79. Balbus, S.A. Enhanced Angular Momentum Transport in Accretion Disks. *Annu. Rev. Astron. Astrophys.* **2003**, *41*, 555–597. [CrossRef]
80. Shakura, N.I.; Sunyaev, R.A. Black holes in binary systems. Observational appearance. *Astron. Astrophys.* **1973**, *24*, 337–355.
81. King, A.R.; Pringle, J.E.; Livio, M. Accretion disc viscosity: How big is alpha? *Mon. Not. R. Astron. Soc.* **2007**, *376*, 1740–1746. [CrossRef]
82. Pessah, M.E.; Chan, C.K.; Psaltis, D. The fundamental difference between shear alpha viscosity and turbulent magnetorotational stresses. *Mon. Not. R. Astron. Soc.* **2008**, *383*, 683–690. [CrossRef]
83. King, A. Accretion disc theory since Shakura and Sunyaev. *Mem. Soc. Astron. Ital.* **2012**, *83*, 466.
84. Kotko, I.; Lasota, J.P. The viscosity parameter α and the properties of accretion disc outbursts in close binaries. *Astron. Astrophys.* **2012**, *545*, A115. [CrossRef]
85. Pringle, J.E. Accretion discs in astrophysics. *Annu. Rev. Astron. Astrophys.* **1981**, *19*, 137–162. [CrossRef]
86. Krolik, J.H. *Active Galactic Nuclei: From the Central Black Hole to the Galactic Environment*; Princeton University Press: Princeton, NJ, USA, 1999.
87. Abramowicz, M.A.; Björnsson, G.; Pringle, J.E. *Theory of Black Hole Accretion Discs*; Cambridge University Press: Cambridge, UK, 1999; p. 309.
88. Manmoto, T. Advection-dominated Accretion Flow around a Kerr Black Hole. *Astrophys. J.* **2000**, *534*, 734–746. [CrossRef]
89. Frank, J.; King, A.; Raine, D.J. *Accretion Power in Astrophysics*, 3rd ed.; Cambridge University Press: Cambridge, UK, 2002; p. 398.
90. Blaes, O.M. Course 3: Physics Fundamentals of Luminous Accretion Disks around Black Holes. In *Accretion Discs, Jets and High Energy Phenomena in Astrophysics*; Beskin, V., Henri, G., Menard, F., Pelletier, G., Dalibard, J., Eds.; Springer: Berlin/Heidelberg, Germany, 2004; pp. 137–185.
91. Narayan, R.; McClintock, J.E. Advection-dominated accretion and the black hole event horizon. *New Astron. Rev.* **2008**, *51*, 733–751. [CrossRef]
92. Kato, S.; Fukue, J.; Mineshige, S. *Black-Hole Accretion Disks—Towards a New Paradigm—*; Kyoto University Press: Kyoto, Japan, 2008.
93. Qian, L.; Abramowicz, M.A.; Fragile, P.C.; Horák, J.; Machida, M.; Straub, O. The Polish doughnuts revisited. I. The angular momentum distribution and equipressure surfaces. *Astron. Astrophys.* **2009**, *498*, 471–477. [CrossRef]
94. Montesinos, M. Review: Accretion Disk Theory. *arXiv* **2012**, arXiv:1203.6851.
95. Abramowicz, M.A.; Fragile, P.C. Foundations of Black Hole Accretion Disk Theory. *Living Rev. Relativ.* **2013**, *16*, 1. [CrossRef] [PubMed]
96. Yuan, F.; Narayan, R. Hot Accretion Flows Around Black Holes. *Annu. Rev. Astron. Astrophys.* **2014**, *52*, 529–588. [CrossRef]
97. Blaes, O. General Overview of Black Hole Accretion Theory. *Space Sci. Rev.* **2014**, *183*, 21–41. [CrossRef]
98. Lasota, J.P. Black Hole Accretion Discs. *Astrophysics of Black Holes: From Fundamental Aspects to Latest Developments*; Bambi, C., Ed.; Astrophysics and Space Science Library; Springer: Berlin/Heidelberg, Germany, 2016; Volume 440, p. 1. [CrossRef]
99. Liu, T.; Gu, W.M.; Zhang, B. Neutrino-dominated accretion flows as the central engine of gamma-ray bursts. *New Astron. Rev.* **2017**, *79*, 1–25. [CrossRef]
100. Popham, R.; Woosley, S.E.; Fryer, C. Hyperaccreting Black Holes and Gamma-ray Bursts. *Astrophys. J.* **1999**, *518*, 356–374. [CrossRef]
101. Narayan, R.; Piran, T.; Kumar, P. Accretion Models of Gamma-ray Bursts. *Astrophys. J.* **2001**, *557*, 949–957. [CrossRef]

102. Kohri, K.; Mineshige, S. Can Neutrino-cooled Accretion Disks Be an Origin of Gamma-ray Bursts? *Astrophys. J.* **2002**, *577*, 311–321. [CrossRef]
103. Di Matteo, T.; Perna, R.; Narayan, R. Neutrino Trapping and Accretion Models for Gamma-ray Bursts. *Astrophys. J.* **2002**, *579*, 706–715. [CrossRef]
104. Kohri, K.; Narayan, R.; Piran, T. Neutrino-dominated Accretion and Supernovae. *Astrophys. J.* **2005**, *629*, 341–361. [CrossRef]
105. Lee, W.H.; Ramirez-Ruiz, E.; Page, D. Dynamical Evolution of Neutrino-cooled Accretion Disks: Detailed Microphysics, Lepton-driven Convection, and Global Energetics. *Astrophys. J.* **2005**, *632*, 421–437. [CrossRef]
106. Gu, W.M.; Liu, T.; Lu, J.F. Neutrino-dominated Accretion Models for Gamma-ray Bursts: Effects of General Relativity and Neutrino Opacity. *Astrophys. J.* **2006**, *643*, L87–L90. [CrossRef]
107. Chen, W.X.; Beloborodov, A.M. Neutrino-cooled Accretion Disks around Spinning Black Holes. *Astrophys. J.* **2007**, *657*, 383–399. [CrossRef]
108. Kawanaka, N.; Mineshige, S. Neutrino-cooled Accretion Disk and Its Stability. *Astrophys. J.* **2007**, *662*, 1156–1166. [CrossRef]
109. Janiuk, A.; Yuan, Y.F. The role of black hole spin and magnetic field threading the unstable neutrino disk in gamma ray bursts. *Astron. Astrophys.* **2010**, *509*, A55. [CrossRef]
110. Kawanaka, N.; Piran, T.; Krolik, J.H. Jet Luminosity from Neutrino-dominated Accretion Flows in Gamma-ray Bursts. *Astrophys. J.* **2013**, *766*, 31. [CrossRef]
111. Luo, S.; Yuan, F. Global neutrino heating in hyperaccretion flows. *Mon. Not. R. Astron. Soc.* **2013**, *431*, 2362–2370. [CrossRef]
112. Xue, L.; Liu, T.; Gu, W.M.; Lu, J.F. Relativistic Global Solutions of Neutrino-dominated Accretion Flows. *Astrophys. J. Suppl. Ser.* **2013**, *207*, 23. [CrossRef]
113. Malkus, A.; Kneller, J.P.; McLaughlin, G.C.; Surman, R. Neutrino oscillations above black hole accretion disks: Disks with electron-flavor emission. *Phys. Rev. D* **2012**, *86*, 85015. [CrossRef]
114. Frensel, M.; Wu, M.R.; Volpe, C.; Perego, A. Neutrino flavor evolution in binary neutron star merger remnants. *Phys. Rev. D* **2017**, *95*, 23011. [CrossRef]
115. Tian, J.Y.; Patwardhan, A.V.; Fuller, G.M. Neutrino flavor evolution in neutron star mergers. *Phys. Rev. D* **2017**, *96*, 43001. [CrossRef]
116. Wu, M.R.; Tamborra, I. Fast neutrino conversions: Ubiquitous in compact binary merger remnants. *Phys. Rev. D* **2017**, *95*, 103007. [CrossRef]
117. Padilla-Gay, I.; Shalgar, S.; Tamborra, I. Multi-Dimensional Solution of Fast Neutrino Conversions in Binary Neutron Star Merger Remnants. *arXiv* **2020**, arXiv:2009.01843.
118. Janiuk, A.; Mioduszewski, P.; Moscibrodzka, M. Accretion and outflow from a magnetized, neutrino cooled torus around the gamma-ray burst central engine. *Astrophys. J.* **2013**, *776*, 105. [CrossRef]
119. Janiuk, A. Microphysics in the Gamma-ray Burst Central Engine. *Astrophys. J.* **2017**, *837*, 39. [CrossRef]
120. Janiuk, A.; Sapountzis, K.; Mortier, J.; Janiuk, I. Numerical Simulations of Black Hole Accretion Flows. *arXiv* **2018**, arXiv:1805.11305.
121. Janiuk, A. The r-process Nucleosynthesis in the Outflows from Short GRB Accretion Disks. *Astrophys. J.* **2019**, *882*, 163. [CrossRef]
122. Bardeen, J.M. A Variational Principle for Rotating Stars in General Relativity. *Astrophys. J.* **1970**, *162*, 71. [CrossRef]
123. Bardeen, J.M.; Press, W.H.; Teukolsky, S.A. Rotating Black Holes: Locally Nonrotating Frames, Energy Extraction, and Scalar Synchrotron Radiation. *Astrophys. J.* **1972**, *178*, 347–370. [CrossRef]
124. Gammie, C.F.; Popham, R. Advection-dominated Accretion Flows in the Kerr Metric. I. Basic Equations. *Astrophys. J.* **1998**, *498*, 313–326. [CrossRef]
125. Bardeen, J.M. Kerr Metric Black Holes. *Nature* **1970**, *226*, 64–65. [CrossRef]
126. Thorne, K.S. Disk-Accretion onto a Black Hole. II. Evolution of the Hole. *Astrophys. J.* **1974**, *191*, 507–520. [CrossRef]
127. Novikov, I.D.; Thorne, K.S. Astrophysics of black holes. In *Black Holes (Les Astres Occlus)*; Dewitt, C., Dewitt, B.S., Eds.; Gordon and Breach Science Publishers Inc.: New York, NY, USA, 1973; pp. 343–450.
128. Page, D.N.; Thorne, K.S. Disk-Accretion onto a Black Hole. Time-Averaged Structure of Accretion Disk. *Astrophys. J.* **1974**, *191*, 499–506. [CrossRef]
129. Landau, L.D.; Lifshitz, E.M. *Fluid Mechanics*; Pergamon Press: Oxford, UK, 1959.
130. Abramowicz, M.A.; Chen, X.M.; Granath, M.; Lasota, J.P. Advection-Dominated Accretion Flows Around Kerr Black Holes. *Astrophys. J.* **1996**, *471*, 762–773. [CrossRef]
131. Abramowicz, M.A.; Lanza, A.; Percival, M.J. Accretion Disks around Kerr Black Holes: Vertical Equilibrium Revisited. *Astrophys. J.* **1997**, *479*, 179–183. [CrossRef]
132. Misner, C.W.; Thorne, K.S.; Wheeler, J.A. *Gravitation*; Princeton University Press: Princeton, NJ, USA, 1973.
133. Mihalas, D.; Mihalas, B.W. *Foundations of Radiation Hydrodynamics*; Oxford University Press: Oxford, UK, 1984.
134. Clifford, F.E.; Tayler, R.J. The equilibrium distribution of nuclides in matter at high temperatures. *Mon. Not. R. Astron. Soc.* **1965**, *69*, 21. [CrossRef]
135. Calder, A.C.; Townsley, D.M.; Seitenzahl, I.R.; Peng, F.; Messer, O.E.B.; Vladimirova, N.; Brown, E.F.; Truran, J.W.; Lamb, D.Q. Capturing the Fire: Flame Energetics and Neutronization for Type Ia Supernova Simulations. *Astrophys. J.* **2007**, *656*, 313–332. [CrossRef]

136. Mavrodiev, S.C.; Deliyergiyev, M.A. Modification of the nuclear landscape in the inverse problem framework using the generalized Bethe-Weizsäcker mass formula. *Int. J. Mod. Phys. E* **2018**, *27*, 1850015. [CrossRef]
137. Rauscher, T.; Thielemann, F.K. Astrophysical Reaction Rates From Statistical Model Calculations. *At. Data Nucl. Data Tables* **2000**, *75*, 1–351.
138. Rauscher, T. Nuclear Partition Functions at Temperatures Exceeding 10^{10} K. *Astrophys. J. Suppl. Ser.* **2003**, *147*, 403–408. [CrossRef]
139. Vincenti, W.G.; Kruger, C.H. *Introduction to Physical Gas Dynamics*; Krieger Pub Co (June 1, 1975); John Wlley & Sons: Hoboken, NJ, USA, 1965.
140. Buresti, G. A note on Stokes' hypothesis. *Acta Mech.* **2015**, *226*, 3555–3559. [CrossRef]
141. Particle Data Group. Review of Particle Physics. *Phys. Rev. D* **2018**, *98*, 30001. [CrossRef]
142. Dolgov, A.D. Neutrinos in the Early Universe. *Sov. J. Nucl. Phys.* **1981**, *33*, 700–706.
143. Sigl, G.; Raffelt, G. General kinetic description of relativistic mixed neutrinos. *Nucl. Phys. B* **1993**, *406*, 423–451. [CrossRef]
144. Hannestad, S.; Raffelt, G.G.; Sigl, G.; Wong, Y.Y.Y. Self-induced conversion in dense neutrino gases: Pendulum in flavour space. *Phys. Rev. D* **2006**, *74*, 105010. Erratum in **2007**, *76*, 029901, doi:10.1103/PhysRevD.76.029901. [CrossRef]
145. Cardall, C.Y. Liouville equations for neutrino distribution matrices. *Phys. Rev. D* **2008**, *78*, 85017. [CrossRef]
146. Strack, P.; Burrows, A. Generalized Boltzmann formalism for oscillating neutrinos. *Phys. Rev. D* **2005**, *71*, 93004. [CrossRef]
147. Dasgupta, B.; Dighe, A.; Mirizzi, A.; Raffelt, G.G. Collective neutrino oscillations in non-spherical geometry. *Phys. Rev. D* **2008**, *78*, 33014. [CrossRef]
148. Tolman, R.C. *Relativity, Thermodynamics, and Cosmology*; Clarendon Press: Oxford, UK, 1934.
149. Klein, O. On the statistical derivation of the laws of chemical equilibrium. *Il Nuovo Cimento (1943–1954)* **1949**, *6*, 171–180. [CrossRef]
150. Klein, O. On the Thermodynamical Equilibrium of Fluids in Gravitational Fields. *Rev. Mod. Phys.* **1949**, *21*, 531–533. [CrossRef]
151. Paczynski, B. A model of selfgravitating accretion disk. *Acta Astron.* **1978**, *28*, 91–109.
152. Raffelt, G.G. *Stars as Laboratories for Fundamental Physics*; University of Chicago Press: Chicago, IL, USA, 1996.
153. Harris, R.A.; Stodolsky, L. Two state systems in media and "Turing's paradox". *Phys. Lett. B* **1982**, *116*, 464–468. [CrossRef]
154. Stodolsky, L. Treatment of neutrino oscillations in a thermal environment. *Phys. Rev. D* **1987**, *36*, 2273–2277. [CrossRef] [PubMed]
155. Janka, H.T. Implications of detailed neutrino transport for the heating by neutrino-antineutrino annihilation in supernova explosions. *Astron. Astrophys.* **1991**, *244*, 378–382.
156. Ruffert, M.; Janka, H.T.; Takahashi, K.; Schaefer, G. Coalescing neutron stars - a step towards physical models. II. Neutrino emission, neutron tori, and gamma-ray bursts. *Astron. Astrophys.* **1997**, *319*, 122–153.
157. Rosswog, S.; Ramirez-Ruiz, E.; Davies, M.B. High-resolution calculations of merging neutron stars—III. Gamma-ray bursts. *Mon. Not. R. Astron. Soc.* **2003**, *345*, 1077–1090. [CrossRef]
158. Kawanaka, N.; Kohri, K. A possible origin of the rapid variability of gamma-ray bursts due to convective energy transfer in hyperaccretion discs. *Mon. Not. R. Astron. Soc.* **2012**, *419*, 713–717. [CrossRef]
159. Preparata, G.; Ruffini, R.; Xue, S.S. The dyadosphere of black holes and gamma-ray bursts. *Astron. Astrophys.* **1998**, *338*, L87–L90.
160. Ruffini, R.; Salmonson, J.D.; Wilson, J.R.; Xue, S.S. On evolution of the pair-electromagnetic pulse of a charged black hole. *A&As* **1999**, *138*, 511–512. [CrossRef]
161. Ruffini, R.; Salmonson, J.D.; Wilson, J.R.; Xue, S.S. On the pair-electromagnetic pulse from an electromagnetic black hole surrounded by a baryonic remnant. *Astron. Astrophys.* **2000**, *359*, 855–864.
162. Shemi, A.; Piran, T. The appearance of cosmic fireballs. *Astrophys. J.* **1990**, *365*, L55–L58. [CrossRef]
163. Piran, T.; Shemi, A.; Narayan, R. Hydrodynamics of Relativistic Fireballs. *Mon. Not. R. Astron. Soc.* **1993**, *263*, 861. [CrossRef]
164. Meszaros, P.; Laguna, P.; Rees, M.J. Gasdynamics of relativistically expanding gamma-ray burst sources - Kinematics, energetics, magnetic fields, and efficiency. *Astrophys. J.* **1993**, *415*, 181–190. [CrossRef]
165. Piran, T. Gamma-ray bursts and the fireball model. *Phys. Rep.* **1999**, *314*, 575–667. [CrossRef]
166. Piran, T. The physics of gamma-ray bursts. *Rev. Mod. Phys.* **2004**, *76*, 1143–1210. [CrossRef]
167. Mészáros, P. Theories of Gamma-ray Bursts. *Annu. Rev. Astron. Astrophys.* **2002**, *40*, 137. [CrossRef]
168. Mészáros, P. Gamma-ray bursts. *Rep. Prog. Phys.* **2006**, *69*, 2259–2321. [CrossRef]
169. Berger, E. Short-Duration Gamma-ray Bursts. *Annu. Rev. Astron. Astrophys.* **2014**, *52*, 43–105. [CrossRef]
170. Kumar, P.; Zhang, B. The physics of gamma-ray bursts and relativistic jets. *Phys. Rep.* **2015**, *561*, 1–109. [CrossRef]
171. Liu, T.; Zhang, B.; Li, Y.; Ma, R.Y.; Xue, L. Detectable MeV neutrinos from black hole neutrino-dominated accretion flows. *Phys. Rev. D* **2016**, *93*, 123004. [CrossRef]
172. Salmonson, J.D.; Wilson, J.R. General Relativistic Augmentation of Neutrino Pair Annihilation Energy Deposition near Neutron Stars. *Astrophys. J.* **1999**, *517*, 859–865. [CrossRef]
173. Birkl, R.; Aloy, M.A.; Janka, H.T.; Müller, E. Neutrino pair annihilation near accreting, stellar-mass black holes. *Astron. Astrophys.* **2007**, *463*, 51–67. [CrossRef]
174. Caballero, O.L.; McLaughlin, G.C.; Surman, R. Neutrino Spectra from Accretion Disks: Neutrino General Relativistic Effects and the Consequences for Nucleosynthesis. *Astrophys. J.* **2012**, *745*, 170. [CrossRef]
175. Ruffini, R.; Rueda, J.A.; Muccino, M.; Aimuratov, Y.; Becerra, L.M.; Bianco, C.L.; Kovacevic, M.; Moradi, R.; Oliveira, F.G.; Pisani, G.B.; Wang, Y. On the Classification of GRBs and Their Occurrence Rates. *Astrophys. J.* **2016**, *832*, 136. [CrossRef]

176. Moghaddas, M.; Ghanbari, J.; Ghodsi, A. Shear Tensor and Dynamics of Relativistic Accretion Disks around Rotating Black Holes. *Publ. Astron. Soc. Jpn.* **2012**, *64*. [CrossRef]
177. Moeen, M. Calculation of the relativistic bulk tensor and shear tensor of relativistic accretion flows in the Kerr metric. *Iran. J. Astron. Astrophys.* **2017**, *4*, 205–221. [CrossRef]
178. Zeldovich, Y.B.; Novikov, I.D. *Relativistic Astrophysics. Volume 1: Stars and Relativity*; University of Chicago Press: Chicago, IL, USA, 1971.
179. Potekhin, A.Y.; Chabrier, G. Equation of state of fully ionized electron-ion plasmas. II. Extension to relativistic densities and to the solid phase. *Phys. Rev. E* **2000**, *62*, 8554–8563. [CrossRef] [PubMed]
180. Dicus, D.A. Stellar energy-loss rates in a convergent theory of weak and electromagnetic interactions. *Phys. Rev. D* **1972**, *6*, 941–949. [CrossRef]
181. Tubbs, D.L.; Schramm, D.N. Neutrino Opacities at High Temperatures and Densities. *Astrophys. J.* **1975**, *201*, 467–488. [CrossRef]
182. Bruenn, S.W. Stellar core collapse—Numerical model and infall epoch. *Astrophys. J. Suppl. Ser.* **1985**, *58*, 771–841. [CrossRef]
183. Ruffert, M.; Janka, H.T.; Schaefer, G. Coalescing neutron stars—A step towards physical models. I. Hydrodynamic evolution and gravitational-wave emission. *Astron. Astrophys.* **1996**, *311*, 532–566.
184. Yakovlev, D.G.; Kaminker, A.D.; Gnedin, O.Y.; Haensel, P. Neutrino emission from neutron stars. *Phys. Rep.* **2001**, *354*, 1–155. [CrossRef]
185. Burrows, A.; Thompson, T.A. *Neutrino-Matter Interaction Rates in Supernovae*; Fryer, C.L., Ed.; Astrophysics and Space Science Library; Springer: Dordrecht, The Netherlands, 2004; Volume 302, pp. 133–174. [CrossRef]
186. Burrows, A.; Reddy, S.; Thompson, T.A. Neutrino opacities in nuclear matter. *Nucl. Phys. A* **2006**, *777*, 356–394. [CrossRef]
187. Aparicio, J.M. A Simple and Accurate Method for the Calculation of Generalized Fermi Functions. *Astrophys. J. Suppl. Ser.* **1998**, *117*, 627–632. [CrossRef]